

CIRCULATION OF THE NORTHEAST PACIFIC OCEAN INFERRED  
FROM TEMPERATURE AND SALINITY DATA.

By

Richard James Matear

B. Eng. (Geophysics) University of Saskatchewan

A THESIS SUBMITTED IN PARTIAL FULFILLMENT OF  
THE REQUIREMENTS FOR THE DEGREE OF  
MASTERS OF SCIENCE

in

THE FACULTY OF GRADUATE STUDIES  
GEOPHYSICS

We accept this thesis as conforming  
to the required standard

THE UNIVERSITY OF BRITISH COLUMBIA

August 1989

© Richard James Matear, 1989

In presenting this thesis in partial fulfilment of the requirements for an advanced degree at the University of British Columbia, I agree that the Library shall make it freely available for reference and study. I further agree that permission for extensive copying of this thesis for scholarly purposes may be granted by the head of my department or by his or her representatives. It is understood that copying or publication of this thesis for financial gain shall not be allowed without my written permission.

Department of Geophysics

The University of British Columbia  
Vancouver, Canada

Date Aug 27 / 89

## Abstract

The temperature, salinity, and pressure (STP) data were collected during two cruises, one in early October and the other in early December of 1987, as part of the Ocean Storms experiment. These hydrographic data were analyzed to determine circulation of the northeast Pacific Ocean and to calculate the factors influencing the heat and salt content of the upper ocean. From the depth profiles of the temperature and salinity data, the water mass in the Ocean Storms area was classified as being the Eastern Sub-Arctic Pacific Water Mass. Maps of dynamic height for this area revealed that the current pattern was generally smooth but that mesoscale eddies did exist in the flow. Isentropic analysis of the temperature and salinity fields produced a flow pattern that was generally consistent with the dynamic height maps. However, this analysis revealed additional details in the flow that were not evident in the dynamic height maps.

To extract additional information from the temperature and salinity data an inverse model was developed. This model assumed that the flow was geostrophic and that the vertical velocity satisfied a linear  $\beta$ -plane vorticity equation. This inverse model calculated the vertical and horizontal velocities at a reference level of 1000 dbars, and the horizontal and vertical mixing terms by conserving mass, salt, and heat. These conservation constraints were applied to large boxes defined by four hydrographic stations and two pressure surfaces.

The circulation determined using the model showed well-defined flow features. Comparison of the absolute geostrophic flow with the seven-day averaged current meter observations showed much similarity, despite complications from an incident storm. Correlation between the geostrophic flow at the surface and the total flow field inferred from

drifter data was also high.

An estimate of the ageostrophic flow suggested that acceleration and nonlinear terms played an important role in affecting the flow field during the first cruise.

The observed change in salt content of the upper 150 m of the ocean was .004 ppt for the sixty days between the two cruises. The net transport of salt into the study area by the calculated flow field was -.016 ppt. Therefore, to balance the salt budget would require  $E - P = 9$  cm. The upper ocean lost  $92 \text{ W/m}^2$  of heat during the sixty days between the two cruises. As the vertical and horizontal transport of heat accounted for  $40 \text{ W/m}^2$  loss of heat, the remainder of heat lost,  $52 \text{ W/m}^2$ , was attributed to air-sea boundary processes.

## Table of Contents

<b>Abstract</b>	<b>ii</b>
<b>List of Tables</b>	<b>vii</b>
<b>List of Figures</b>	<b>x</b>
<b>Acknowledgement</b>	<b>xv</b>
<b>1 Introduction</b>	<b>1</b>
<b>2 Hydrographic Data</b>	<b>5</b>
2.1 Data Collection . . . . .	5
2.2 Data Calibration . . . . .	11
2.3 Data Processing . . . . .	11
2.4 Removal of Internal Waves . . . . .	12
<b>3 Hydrography of the Ocean Storms Area</b>	<b>15</b>
3.1 Temperature and Salinity Structure . . . . .	15
3.1.1 Vertical Structure . . . . .	15
3.1.2 Temperature-Salinity Diagram . . . . .	19
3.2 The Horizontal Flow Field . . . . .	21
3.3 Dynamic Height . . . . .	22
3.3.1 Horizontal Distribution of Temperature and Salinity . . . . .	29
3.4 Summary . . . . .	31

<b>4</b>	<b>Developing and Solving the Inverse Problem</b>	<b>44</b>
4.1	Determining the Ocean Circulation: The Physical Problem . . . . .	44
4.2	The Inverse Problem . . . . .	47
4.2.1	Formulation . . . . .	47
4.2.2	Ocean Storms Grid . . . . .	50
4.3	Including A Priori Information . . . . .	52
4.4	Solving the Inverse Problem . . . . .	54
<b>5</b>	<b>Evaluating the Model and Solution</b>	<b>62</b>
5.1	The Importance of Temperature, Salt and Mass Conditions on the Solution	63
5.2	The Effect of the Layering of the Ocean on the Solution . . . . .	69
5.3	The Sensitivity of the Solution to the Choice of Reference Level . . . . .	71
5.4	The Importance of the Different Unknown Parameters on the Solution . .	73
5.5	Sensitivity of the Solution to Errors in the Data . . . . .	74
5.6	Reference Solution . . . . .	78
<b>6</b>	<b>Results of the Model</b>	<b>80</b>
6.1	Vertical Velocity . . . . .	80
6.2	Vertical Mixing Coefficients . . . . .	81
6.3	Horizontal Velocities . . . . .	81
6.4	Direct Current Measurements . . . . .	89
6.5	Mixed Layer Drifters . . . . .	99
<b>7</b>	<b>Factors Influencing Heat and Salt Content in the Ocean Storms Area</b>	<b>104</b>
7.1	The Observed Change in Salt and Heat Content . . . . .	104
7.2	Transport of Salt and Heat . . . . .	107
7.2.1	Salt Transport . . . . .	108

7.2.2	Heat Transport . . . . .	109
7.3	Exchange Across the Air-Sea Boundary . . . . .	110
7.3.1	Salt Budget . . . . .	111
7.3.2	Heat Budget . . . . .	112
<b>8</b>	<b>Discussion and Conclusion</b>	<b>114</b>
	<b>Bibliography</b>	<b>119</b>

## List of Tables

4.1	The levels used to vertically define the boxes used in the model. . . . .	51
5.2	Correlation and regression coefficients between up-weighted solutions and the reference solution which weighted the three conditions equally ( $T=1$ , $S=1$ , $M=1$ ). . . . .	64
5.3	The normalized residual errors in the three conditions for the null solution, the reference solution, and the solution obtained by alternating the up-weighting of the three conditions. The solution for temperature, salt or mass is the solution obtained when this condition is up-weighted by a factor of 5. . . . .	65
5.4	Correlation and regression coefficients between solutions with various weights for the conservation of mass condition. The weighting of the temperature and salt conditions are held fixed at one. . . . .	67
5.5	The normalized residual errors in the conservation of temperature, salt, and mass conditions for various weights for the conservation of mass condition. The Null column refers to errors in these three conditions if the solution is identically zero. . . . .	68
5.6	The correlation and regression coefficients between the reference solution, a 12-layer model with solutions obtained from models using different numbers of layers. . . . .	70

5.7	The correlation and regression coefficients between the reference solution and solutions obtained by doubling the thickness of the layers considered in the model. For the 6-layer model the ocean is divided according to the following pressure surfaces, 150, 250, 400, 600, 800, 1000, 1500 dbar. The 5-layer model divides the ocean according to the following surfaces, 150, 250, 500, 800, 1000, 1500 dbar. Only the reference vertical and horizontal velocities are used in determining the regression and correlation coefficients.	71
5.8	The correlation and regression coefficient between solutions using different reference levels and the reference solution that used 1000 dbar. The correlation and regression coefficients were calculated using the velocities from 1000 dbar and all of the mixing coefficients. . . . .	72
5.9	The correlation and regression coefficient for horizontal reference velocities between solutions obtained with a reduce set of unknown parameters. . . . .	75
5.10	The correlation and regression coefficients between the reference solution and solutions obtained using data with random errors added. The random errors with standard deviation $\sigma$ are add to the original data as follows: a) salinity, $\pm\sigma$ ppt and b) temperature, $\pm\sigma$ °C. . . . .	75
5.11	The correlation and regression coefficients between the reference solution and solutions obtained using data with coherent temperature and salinity errors added to the data. . . . .	76
6.12	A comparison of the geostrophic velocities calculated from the model to the current meter observations. . . . .	91

7.13	Change in salt content between cruise one and cruise two. The value given for the change in salt content is the change in salinity observed in that layer. The mean and standard deviation are obtained using the stations occupied during both cruises. . . . .	106
7.14	Change in heat content between cruise one and cruise two. The value given for the change in heat content is the change in heat observed in that layer. The mean and standard deviation are obtained using the stations occupied during both cruises. . . . .	107
7.15	The calculated transport of salt using circulation parameters determined by the inverse model. The vertical mixing term is only important at depths of 250 m to 800 m. The errors in these transports are determined from the uncertainty in the circulation parameters and the uncertainty in the measurement of salinity. A positive transport means that the Ocean Storms area experiences a gain in salinity. . . . .	108
7.16	The calculated fluxes of heat from using the velocities obtained from the inverse model. The vertical mixing term is only important at depths of 500 m to 1200 m. The errors in these transports are determined from the uncertainty in the circulation parameters and the uncertainty in the measurement of temperature. . . . .	110

## List of Figures

2.1	Location of the Ocean Storms area in the northeast Pacific Ocean. . . . .	6
2.2	The planned hydrographic grid for the Ocean Storms area. . . . .	7
2.3	The STP stations occupied during the first cruise (8702) in the Ocean Storms grid and surrounding area. The arrows indicate the path travelled by the ship during this cruise. . . . .	9
2.4	The STP stations occupied during the second cruise (8704) in the Ocean Storms grid and surrounding area. The arrows indicate the path travelled by the ship during the cruise. . . . .	10
2.5	Potential density versus pressure plots. The upper panel shows the presence of the internal wave in the data. The lower panel shows the filtered version with this internal wave removed. . . . .	13
3.6	Major surface currents of the North Pacific Ocean. The Ocean Storms area is centred at $47.5^{\circ}$ N and $139.0^{\circ}$ W, just southeast of Ocean Station P. . . . .	16
3.7	Salinity and temperature profiles from the Ocean Storms area (OS10, $48^{\circ}$ N and $139.3^{\circ}$ W). In these plots the solid line refers to data from cruise one and the dash line represents data from cruise two. . . . .	17
3.8	Temperature-Salinity (T-S) diagrams for the first cruise (8702) and for the second cruise (8704) for data obtained from the Ocean Storms area. In these plots the solid line represents the average T-S curve for that cruise. . . . .	20

3.9	Spatial structure of the T-S diagram for cruise one (8702). The solid line represents the T-S curve from OS25. These plots show the presence of two different water masses (A) and (B) in the halocline. . . . .	21
3.10	Cruise One: Dynamic Height in dynamic meters relative to 1000 dbar at: a) the surface, b) 150 dbar, c) 500 dbar. In these maps the arrows indicate the direction of the geostrophic flow and the dots denote the location of the STP stations obtained during this cruise. . . . .	23
3.11	Cruise Two: Dynamic Height in dynamic meters relative to 1000 dbar at: a) the surface, b) 150 dbar, c) 500 dbar. In these maps the arrows indicate the direction of the geostrophic flow and the dots denote the location of the STP stations obtained during this cruise. . . . .	26
3.12	Temperature and Salinity distribution for cruise one on the $\sigma_t = 25.0$ surface for: a) the temperature distribution in deg C, and b) the salinity distribution in ppt. The arrows in these maps indicate the interpretative current pattern. . . . .	32
3.13	Temperature and Salinity distribution for cruise one on the $\sigma_t = 26.2$ surface for: a) the temperature distribution in deg C, and b) the salinity distribution in ppt. The arrows in these maps indicate the interpretative current pattern. . . . .	34
3.14	Temperature and Salinity distribution for cruise one on the $\sigma_t = 27.0$ surface for: a) the temperature distribution in deg C, and b) the salinity distribution in ppt. The arrows in these maps indicate the interpretative current pattern. . . . .	36

3.15	Temperature and Salinity distribution for cruise two on the $\sigma_t = 25.5$ surface for: a) the temperature distribution in deg C, and b) the salinity distribution in ppt. The arrows in these maps indicate the interpretative current pattern. . . . .	38
3.16	Temperature and Salinity distribution for cruise two on the $\sigma_t = 26.2$ surface for: a) the temperature distribution in deg C, and b) the salinity distribution in ppt. The arrows in these maps indicate the interpretative current pattern. . . . .	40
3.17	Temperature and Salinity distribution for cruise two on the $\sigma_t = 27.0$ surface for: a) the temperature distribution in deg C, and b) the salinity distribution in ppt. The arrows in these maps indicate the interpretative current pattern. . . . .	42
4.18	The boxes used for the inverse model of the Ocean Storms area. For cruise one, all the boxes are defined. . . . .	48
4.19	A plot of the normalized magnitude of the singular values versus index number p. . . . .	58
4.20	The reduction in error versus the number of singular values of matrix <b>B</b> that are used in determining the solution. The number of singular values used (n), indicates that the first n singular values of matrix <b>B</b> are used. . . . .	59
4.21	The trade-off curve for the inverse model. This curve relates the resolution of the model to the size of the variance of the unknowns. The numbers over the points on this curve indicate the cutoff for the singular values. . . . .	61
5.22	The high frequency fluctuations of the temperature measurements obtained from a mooring located in the centre of the grid. . . . .	77

6.23	The vertical velocity determined from the inverse model. The velocities are in $\mu m/s$ and a positive value means the flow is upward. The top map shows the vertical velocity at the base of the mixed layer (50 m). The lower map is the vertical velocity at the base of the halocline (150 m).	82
6.24	The vertical mixing coefficients, $k_z$ , determined from the inverse model.	83
6.25	The horizontal flow field for selected depth surfaces of the upper zone (0-200 m). The velocity is shown at: a) the surface, b) 15 m, c) 100 m, and d) 200 m.	85
6.26	The horizontal flow field in the intermediate zone (200- 900 m) at selected depths. The velocity is shown at depths: a) 500 m, b) 600 m, c) 700 m, and d) 900 m.	87
6.27	The horizontal flow field in the deep zone (900-1500 m) at selected depths. The velocity at depths of a) 1000 m and b) 1500 m.	90
6.28	The velocities from the current meter observations for a seven day average plotted every three days. In this figure the stick points in the direction of flow, with north being up. The numbers on the left side of the plot are the corresponding depths in meters of the current meter. On the right side of the plot, the velocities calculated from the inverse model at the location of the mooring are displayed.	92
6.29	The velocities from the current meter observations for a fourteen day average plotted every seven days. In this figure the stick points in the direction of flow, with north being up. The numbers on the left side of the plot are the corresponding depths in meters of the current meter. On the right side of the plot, the velocities calculated from the inverse model at the location of the mooring are displayed.	93

6.30	The velocities from the current meter observations for a 21 day average plotted every 10 days. In this figure the stick points in the direction of flow, with north being up. The numbers on the left side of the plot are the corresponding depths in meters of the current meter. On the right side of the plot, the velocities calculated from the inverse model at the location of the mooring are displayed. . . . .	94
6.31	The v-component of the velocity measured at 3000 m on the OSU mooring(upper panel) and the v-component computed from the geostrophic relation and data from the bottom pressure sensor array. . . . .	95
6.32	The horizontal velocity profiles for a) the geostrophic flow, b) the ageostrophic flow, and c) the total flow. . . . .	98
6.33	The tracks of the drifter data: The location of the Ocean Storms grid is defined by the dashed line on this map. The oscillation of the drifter tracks is due to inertial oscillations. . . . .	100
6.34	The total flow field determined from the drifter data. The location of the Ocean Storms grid is shown by the enclosed region on this map. This velocity map is obtained from the drifter data from day 275 to 295. . . .	101
6.35	The ageostrophic flow field determined from subtracting the geostrophic velocity determined from the inverse model at 15 m from the total flow estimated from the drifter data. . . . .	103

## Acknowledgement

I would like to thank my supervisors Dr. W. Hsieh and Dr. G. McBean for their inspiration and guidance during the work on this thesis. I would also like to thank Dr. W. Large for the enthusiastic suggestions he provided during my research.

Dr. S. Tabata generously supplied the STP data as well as invaluable information on the analysis of these data. The current meter observations were provided by Dr. C. Paulson and Dr. M. Levine of Oregon State University. The drifter data were supplied by Dr. W. Large of University of British Columbia.

I would also like to acknowledge the moral support provided by my wife, Rhonda who had the unenviable task of proof-reading the many drafts of my thesis.

## Chapter 1

### Introduction

One of the major goals of physical oceanography is to obtain a description of the large time-scale movement of water in the ocean. Determination of this general circulation is an important step toward understanding global climate and the distribution of chemical properties in the ocean [1]. The main body of knowledge about the general circulation of the ocean has been drawn from observations of the temperature and salinity distributions in the ocean. The justification behind using temperature and salinity to infer ocean circulation are: 1) these quantities are relatively easy to measure and 2) in contrast to direct velocity measurements, the signals in the temperature and salinity fields are far less contaminated by energetic smaller-scale motions induced by eddies and waves [2].

The inference of flow characteristics from temperature and salinity data has evolved along two distinct paths: 1) the water mass analysis techniques (eg. isentropic analysis [3]), and 2) dynamic methods (eg. Beta Spiral method[4]). In the water mass analysis techniques, water masses with a characteristic range of temperature, salinity, and other properties are identified. By identifying the location of the source of these water masses, a qualitative description of the flow can be inferred by assuming the path of the flow must be from the source to the point of observation [3]. This technique allows one to infer the flow field directly from the observed temperature and salinity distribution, but no quantitative description of the flow can be made.

In dynamic methods, the constraint governing the large-scale flow in the ocean is

geostrophy, the balance between the pressure gradient and the Coriolis forces

$$\vec{k} \times f\vec{u} = -\frac{1}{\rho}(\vec{\nabla}p) \quad (1.1)$$

The  $\vec{k}$  is the unit directional vector in the  $z$  direction (up). The pressure gradient can be related to the density stratification via the hydrostatic approximation. From the temperature and salinity information one can calculate the density stratification and determine the flow relative to a prescribed reference level,  $z_r$ , using the thermal wind equations

$$u = -\frac{g}{\rho_0 f} \int_{z_r}^z \rho_y dz \quad (1.2)$$

$$v = -\frac{g}{\rho_0 f} \int_{z_r}^z \rho_x dz \quad (1.3)$$

The classical approach to solving this problem is to subjectively determine a depth of no motion and set the reference level  $z_r$  equal to this depth. Dietrich [5] reviewed five different proposals for ascertaining this depth of no motion and concluded that none of the methods considered were very reliable.

In recent years a more mathematical approach has been taken to determine the general circulation of the ocean by dynamic methods. Two methods that have been developed which pose the problem mathematically as an inverse problem are the Beta Spiral method [4] and the box model method [1].

The Beta Spiral method was originally developed by Schott and Stommel [4] to determine the velocity at the reference level. In this method, an additional dynamic constraint, a linear  $\beta$ -plane vorticity equation, was used to constrain the velocity at the reference level. This method allowed the determination of the 3-dimensional velocity field. Olbers et al [6] applied this method to a set of grid points in the North Atlantic Ocean. In their formulation, the conservation of mass, potential density, and potential vorticity (a linear functional of temperature and salinity defined to be orthogonal to the potential

density in the T-S diagram [6]) were included to further constrain the solution. These constraints were applied at each grid point for several depths through a finite difference equation. Olbers et al solved the problem locally at each grid point independently of other grid points. Each grid point therefore required its own inverse solution. By considering enough vertical depths at each grid point, one derives an overdetermined system of equations and finds the least squares solution to the problem.

In the box model method originally presented by Wunsch [1], an inverse problem was formulated for determining the general circulation of the North Atlantic by considering the conservation of mass in several large boxes. These boxes were defined horizontally by large regions of the North Atlantic Ocean bounded by hydrographic stations, and vertically by several isothermal layers. A solution to the problem was obtained by determining velocities at the prescribed reference level that best conserved the mass flowing into each of the boxes considered. In applying this method to large boxes containing many hydrographic stations, the inverse problem that was generated was highly underdetermined (ie. an infinite number of solutions existed). In order to obtain only one solution to the problem, Wunsch required the solution to conserve the mass and minimize the energy of the unknown reference velocities (smallest model solution). In later papers by Wunsch [7,8], additional constraints on the solution were imposed by conserving salt and heat. With the addition of more constraints, additional unknowns were also included for determining the vertical velocity and horizontal and vertical mixing coefficients. By using only three conservation constraints the problem still remained underdetermined [7]. In view of this situation, Wunsch [8] chose to investigate the range of possible solutions consistent with the set of constraints rather than to try to determine one unique solution.

From the methods presented above, I have developed a box model method that makes use of the linear  $\beta$ -plane vorticity equation. This method is used in this thesis to investigate the circulation in the northeast Pacific Ocean from data obtained as part of the

*Ocean Storms Experiment.*

The organization of this thesis is as follows. In Chapter 2, I present a brief account of the collection, calibration, and data processing of the hydrographic data collected in the Ocean Storms Experiment. In Chapter 3, I describe the general oceanic features of the Ocean Storms area through the use of the observed temperature and salinity information and maps of dynamic height. In Chapter 4, I develop the physics behind the model employed and then proceed to show how the inverse problem was formulated and solved. In Chapter 5, the model is investigated to evaluate the uncertainty of the calculated unknowns. Chapter 6 presents the circulation parameters calculated from the model. The calculated flow field is compared to current meter observations and Lagrangian Drifters. From these measurements, the time-scale of geostrophic flow is estimated and the ageostrophic flow is calculated and discussed. In Chapter 7, the salt and heat transport due to horizontal and vertical velocities and mixing terms is calculated for the upper ocean. These values are compared to the observed changes in salt and heat content. From the differences between these two measurements, the salt and heat budgets are balanced to estimate the effect of the air-sea boundary processes. Chapter 8 concludes this thesis with a discussion and summary of the limitations of the model, and interpretation of the ocean circulation in the Ocean Storms area.

## Chapter 2

### Hydrographic Data

The hydrographic data made available for this thesis were acquired as part of the Ocean Storms Experiment. This experiment was a joint Canadian-American effort designed to study the interaction of the atmosphere and ocean during severe storms. The main goals of this experiment were to:

- 1) measure the surface fluxes of heat and momentum during severe storms.
- 2) compute a 3-dimensional heat budget of the oceanic mixed layer and seasonal thermocline.
- 3) test the oceanic response to severe storms against appropriate physical models.

This project was carried out in the open ocean 1000 km off the coast of Vancouver Island, centred at  $47.5^{\circ}$  N and  $139.0^{\circ}$  W (Fig. 2.1). In the Ocean Storms area, it was planned that the hydrographic data would be collected on a  $6 \times 5$  grid with grid spacings of 60 km (Fig. 2.2). With this grid spacing it was expected that mesoscale features of the ocean would be resolved [9].

#### 2.1 Data Collection

The hydrographic data for this thesis was acquired during two cruises in the fall of 1987. This is a summary of information presented in the data report for these two cruises [10]. During both cruises, the same equipment was used to obtain the hydrographic data. The salinity/temperature profiles (STP) were collected with a Guildline 8705 Digital STP probe /87102 Deck Control unit. The transmission of the data to the surface

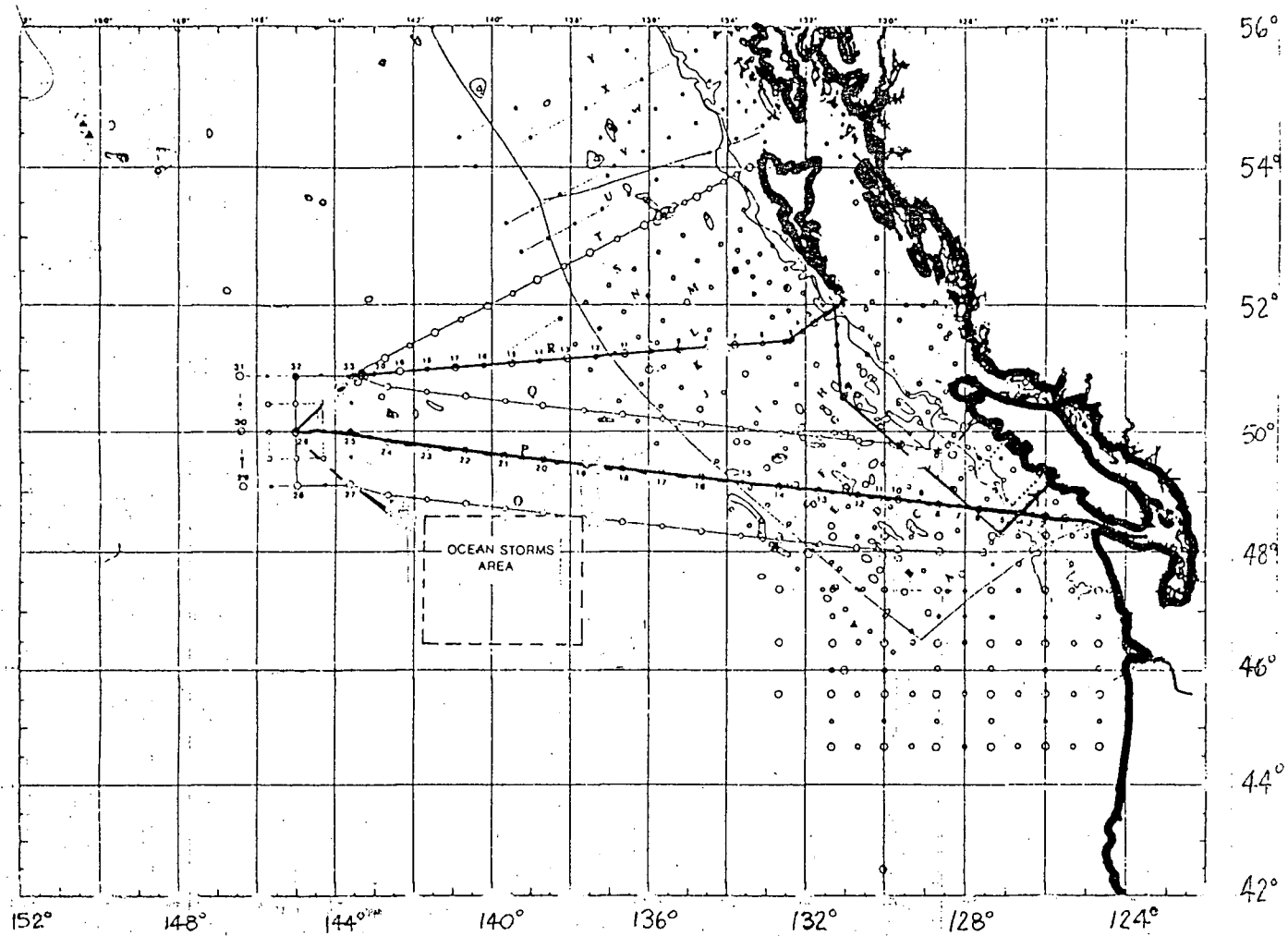


Figure 2.1: Location of the Ocean Storms area in the northeast Pacific Ocean.

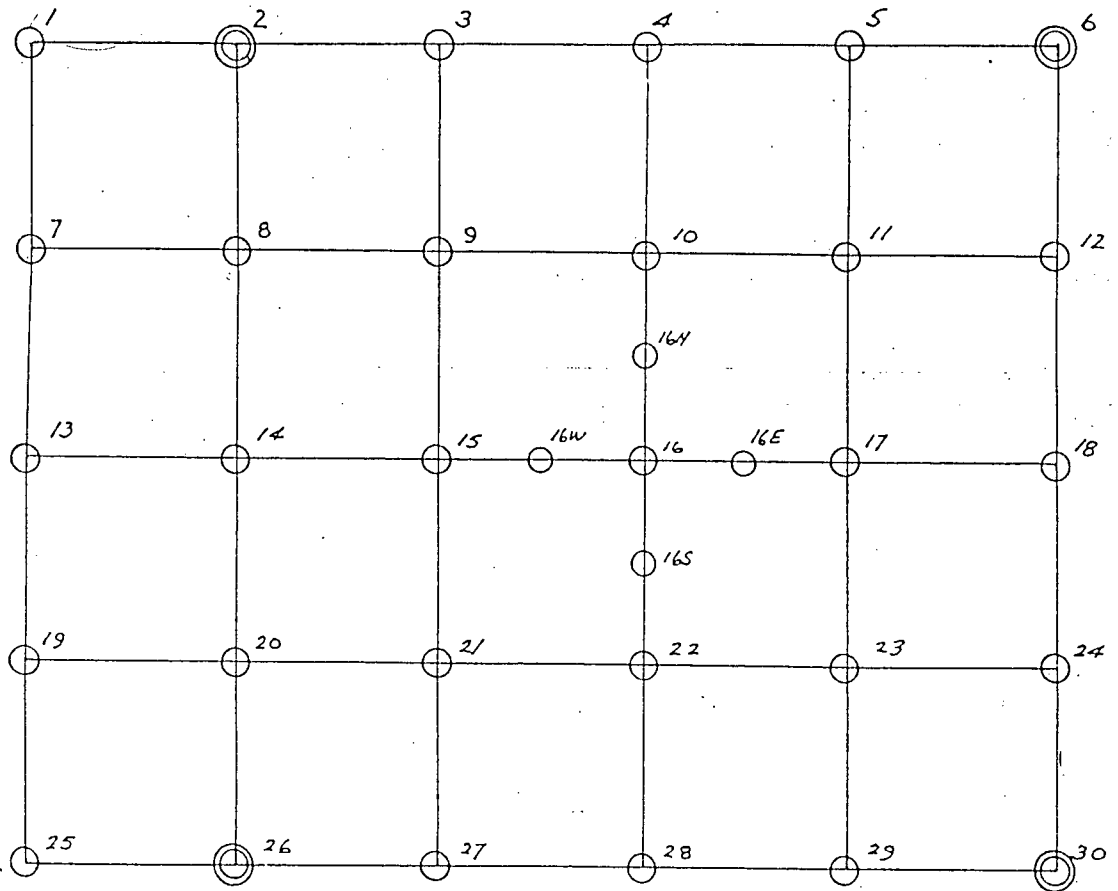


Figure 2.2: The planned hydrographic grid for the Ocean Storms area.

was performed by a Sea Tech Transmissometer attached to the STP probe. In addition, hydrographic casts were made with Niskin sampling bottles, each fitted with two reversing thermometers. For samples  $\geq 200$  m, a single reversing thermometer was used. The salinities from these bottle samples were determined in duplicate with a Guildline 8400 Autosal salinometer at the Institute of Ocean Sciences (IOS). The ship was also equipped with a sea water loop system which provided temperature and salinity readings from a depth of 3 m every 2 minutes. The salinities observed from this unit were considered to accurately represent the salinity of the upper mixed layer [11].

For the first cruise (8702), carried out from Sept. 22 to Oct. 16, good weather allowed the completion of all of the planned survey. During this cruise, 117 STP stations were occupied and 8 hydrographic casts were acquired. All 34 STP stations in the Ocean Storms area were occupied (Fig. 2.3). One hydrographic cast was obtained in the Ocean Storms area at station OS14. In the closely spaced grid of the Ocean Storms area, all the STP stations were acquired to a depth of 1500 dbar, except for stations OS31 to OS34 which went to a depth of 500 dbar. The second cruise (8704), carried out from Nov.25 to Dec. 5, was plagued by persistent gales and storms with winds reaching speeds of 75 knots. Due to the rough conditions at sea, only a fraction of the planned STP stations were occupied. During this cruise, 32 STP stations were occupied and 3 hydrographic casts made. Only 17 STP stations were acquired in the Ocean Storms grid (Fig. 2.4). The failure of the second cruise to cover all the desired locations in the Ocean Storms grid limited the usefulness of using this data in the inverse model. The data from this cruise will be used only to calculate the change in heat and salt content of the ocean.

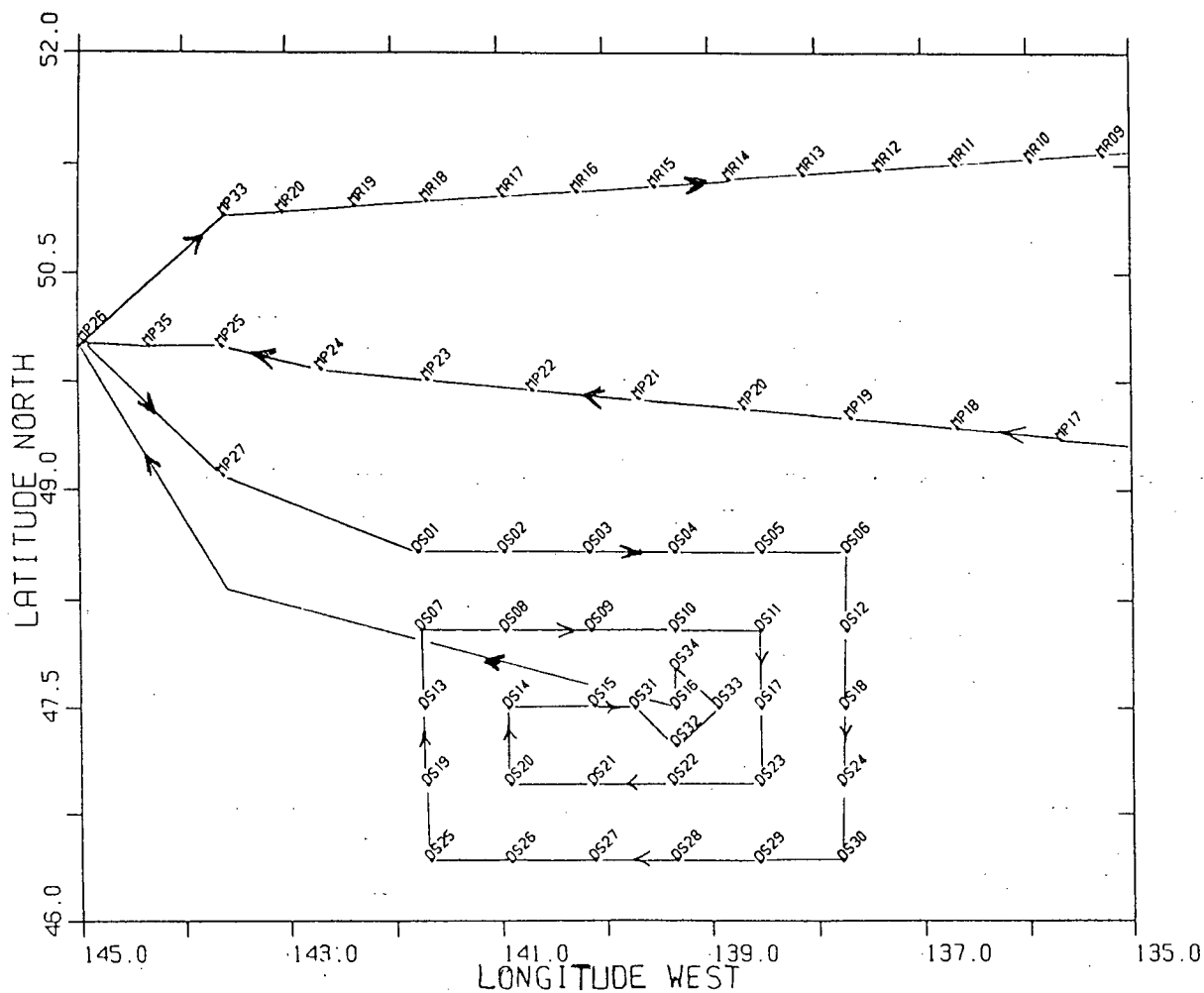


Figure 2.3: The STP stations occupied during the first cruise (8702) in the Ocean Storms grid and surrounding area. The arrows indicate the path travelled by the ship during this cruise.

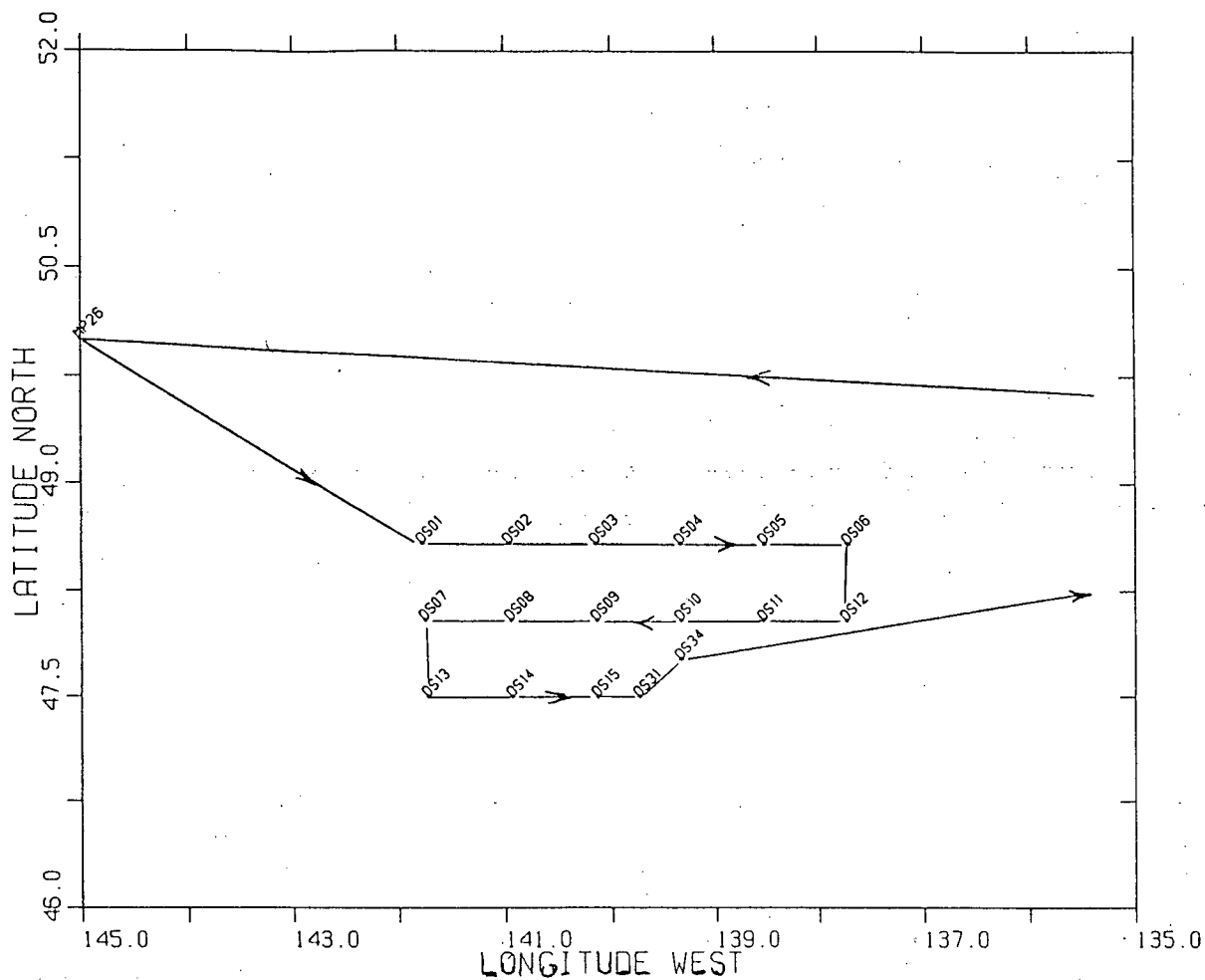


Figure 2.4: The STP stations occupied during the second cruise (8704) in the Ocean Storms grid and surrounding area. The arrows indicate the path travelled by the ship during the cruise.

## 2.2 Data Calibration

The STP data were calibrated by comparing these values to the measurements obtained from the hydrographic casts, special calibration samples (sampling bottles placed a few metres above the STP sensor usually at 1500 dbar), and the sea water loop system. The data report [10] provides more details on the calibration than the summary given below.

For the first cruise, the STP temperature readings were almost identical to the readings obtained from the hydrographic cast and the calibration samples.

STP temp - T hydro/calib. =  $+0.003^{\circ}\text{C}$  (standard deviation of  $0.05^{\circ}\text{C}$ )

Therefore, no correction was applied to the STP temperatures. Comparing the STP salinities for the first cruise to calibration readings indicated that a slight instrumental drift occurred during this cruise. The correction for the STP salinities was accomplished as follows:

- 1) P01 - P14 subtract 0.016 ppt from STP salinity
- 2) P15 - R06 subtract 0.047 ppt from STP salinity (Ocean Storms grid)
- 3) R07 - END subtract 0.081 ppt from STP salinity

For the second cruise it appeared that the observed STP temperature and salinity values exhibited a temperature dependence. A regression curve using STP temperature was used to reduce the observed STP temperature and salinity values to the "correct" temperature and salinity values [10].

## 2.3 Data Processing

To convert the STP conductivity measurements to salinity, the practical salinity units were used [12]. The temperature and salinity values were interpolated to a constant pressure interval of 1 dbar. To smooth any random errors present in the temperature and salinity values, a running average filter was applied to the data. The following filter

lengths were applied to the data:

- 1) 10 dbar filter length for the interval 0 - 500 dbar
- 2) 20 dbar filter length for depths greater than 500 dbar

From the filtered values of temperature and salinity, potential density and dynamic height relative to 1000 dbar were determined [12].

## 2.4 Removal of Internal Waves

It is evident in the plot of potential density as a function of pressure for several stations in the Ocean Storms area (Fig. 2.5), that oscillations occurred in the pycnocline. These oscillations in part are caused by internal waves [13]. From a study of the temporal variability at Ocean Station P (Station MP26 in Fig. 2.1), it was determined that most of the variability in the internal wave is in the semidiurnal frequency band [13]. Marginally resolvable spectral peaks also occurred within the diurnal and near inertial band (16 to 24 hrs).

In order to properly calculate the change in heat and salt content at any one station it is necessary to remove the temporal fluctuations of temperature caused by internal waves. The reduction of the effects of these internal waves was accomplished by calculating an average potential density function of pressure by averaging several adjacent stations collected over a time period of 12 to 18 hours. The original density function was then shifted in depth in order to match the average density curve (Fig. 2.5). The corresponding values of temperature and salinity were not altered but their position in depth moved up or down in accordance with the match to the average density function. The temperature and salinity values were then interpolated back to the original pressure sampling. A tapered cut-off was used so that no changes were made to the data for depths having a density  $\geq 26.8$ . Below this point, the effect of the internal waves on the salt or heat

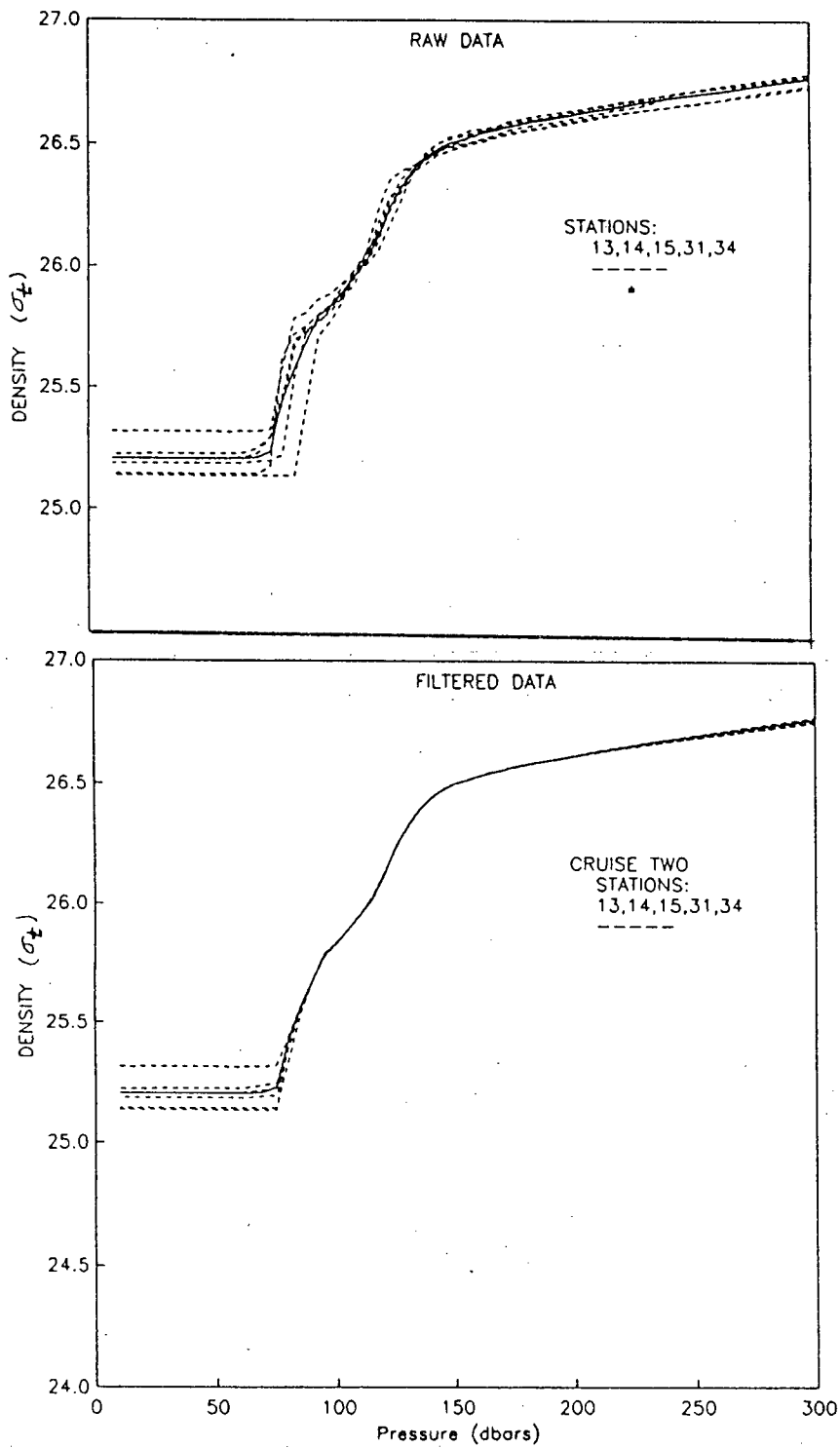


Figure 2.5: Potential density versus pressure plots. The upper panel shows the presence of the internal wave in the data. The lower panel shows the filtered version with this internal wave removed.

content of the ocean was not significant because the change in temperature and salinity with depth was small. This technique of removing the internal tides from the data lacks a sound theoretical basis, but faced with the data available it was deemed to be the best approach. This filtering method will also reduce baroclinic eddies present in the data.

## Chapter 3

### Hydrography of the Ocean Storms Area

The major surface currents of the North Pacific Ocean are shown in Figure 3.6 [14]. Due to influences of the wind system over the North Pacific Ocean, the surface water tends to flow eastward across the ocean. The Ocean Storms area lies in the broad boundary between the West Wind Drift and the Sub-Arctic current [14]. The expected surface geostrophic current through the Ocean Storms region should be of the order of 5 km/day ( 5.8 cm/sec) in an easterly or northeasterly direction [14]. This flow may be complicated by eddies with spatial scales of 50 - 100 km [15].

#### 3.1 Temperature and Salinity Structure

##### 3.1.1 Vertical Structure

The water mass in the vicinity of the Ocean Storms area is the Eastern Sub-Arctic Pacific Water Mass [9]. The structure of this water mass is characterized by three zones: the upper "seasonal" zone (0-100 m), a principal halocline (100-200 m), and a lower zone ( $\geq 200$  m) [9]. An example of the vertical temperature and salinity structure in the Ocean Storms area is displayed in Figure 3.7. These plots clearly show the three characteristic zones.

The upper seasonal zone is defined by a layer of relatively constant salinity. For the first cruise this zone can be divided into two layers, a well mixed upper layer of constant temperature and salinity, and a lower layer possessing a prominent seasonal thermocline



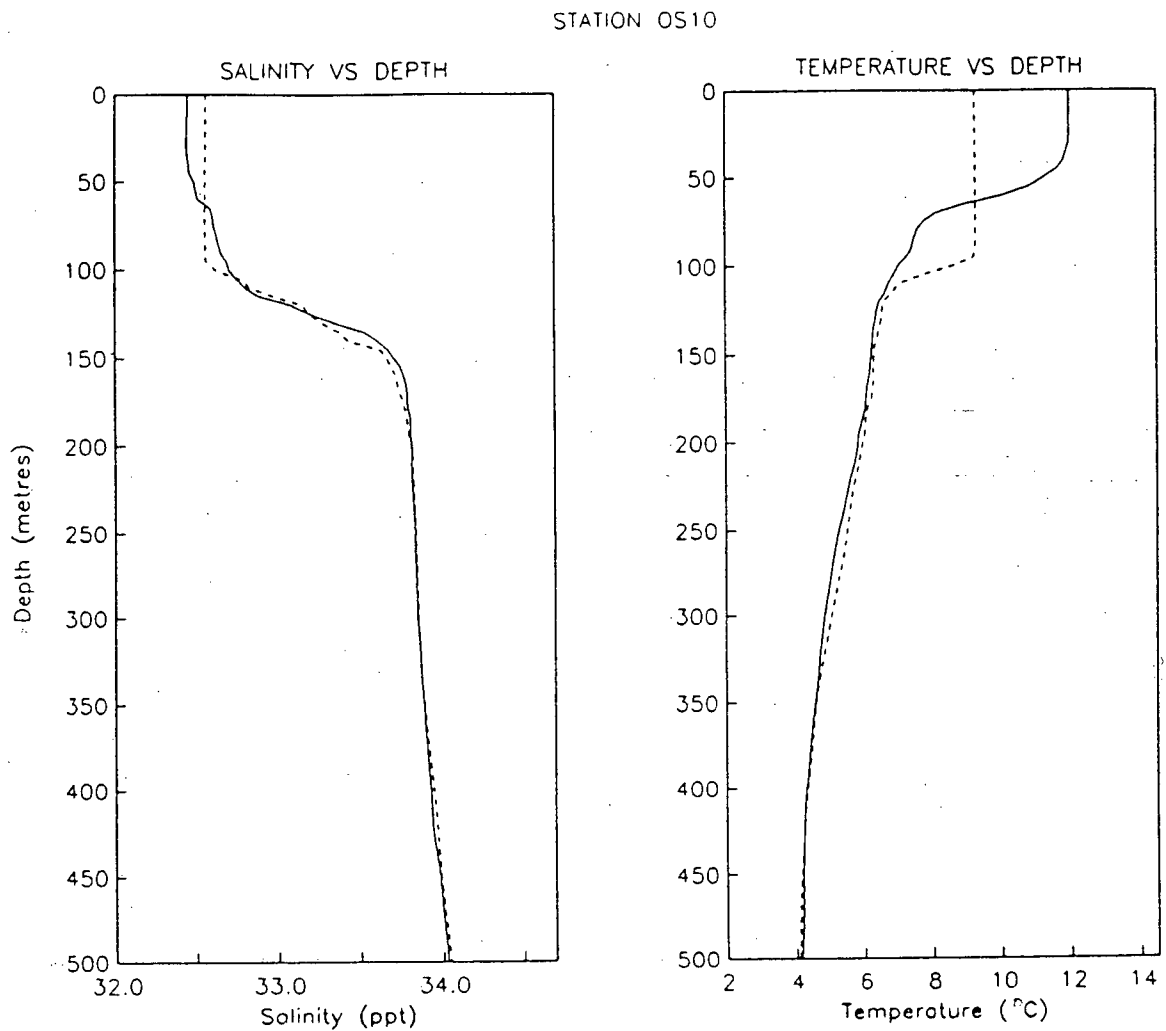


Figure 3.7: Salinity and temperature profiles from the Ocean Storms area (OS10, 48° N and 139.3° W). In these plots the solid line refers to data from cruise one and the dash line represents data from cruise two.

and a small seasonal halocline. By the second cruise, this upper zone has undergone a couple of dramatic changes. One, the mixed layer has deepened by 50 m to encompass the first 100 m. Two, the mixed layer has experienced an increase in salinity of 0.2 ppt and a decrease in temperature of  $2.7^{\circ}\text{C}$ . These changes to the mixed layer are offset by changes of the opposite sign to the seasonal thermocline and seasonal halocline. The changes that occurred to the upper ocean between the two cruises are caused principally by two effects, by a loss of heat to the atmosphere, and by the vertical mixing of the cooler and saltier water of the halocline and seasonal thermocline with the warmer and fresher surface waters [16]. The role of horizontal transport in altering the salinity and temperature of the upper zone is less well known but is necessary to balance the salt and heat budgets [14].

The second zone, the principal halocline, occurs where the salinity increases rapidly with depth. This zone is clearly present in both cruises and it represents a transition zone between the upper and lower zones. The temperature in this zone generally decreases with depth but at some of the Ocean Storms stations, a temperature inversion occurs. This situation is still stable because of the dominating effect that salinity has in determining the density of the water column. The presence of this marked halocline prevents winter convective overturn from being able to mix water deeper than the halocline [9]. Only with the occurrence of intense evaporation at the surface can the halocline be eroded to allow mixing below the halocline [9]. This erosion of the halocline is not evident in the data from the two cruises.

In the lower zone the temperature decreases gradually with depth, reaching  $2.8^{\circ}\text{C}$  at a depth of a 1000 m and  $1.5^{\circ}\text{C}$  in the abyssal layers (4000 m)[17]. The salinity also increases gradually with depth, reaching 34.4 ppt at 1000 m and 34.7 ppt in the abyssal layers [17]. The differences in salinity and temperature between the two cruises are small for this zone. This implies that the steady state assumption should be valid in this zone

for the time interval between the two cruises.

### 3.1.2 Temperature-Salinity Diagram

The presence of three distinct zones in the depth structure of the water is illustrated in the temperature-salinity (T-S) diagram by the three main segments of the T-S diagram (Fig. 3.8). These three zones can be divided according to potential density ( $\sigma_t$ ):

- 1) the upper zone  $\sigma_t \leq 25.8$
- 2) the principal halocline  $25.8 \leq \sigma_t \leq 26.6$
- 3) the lower zone  $\sigma_t \geq 26.6$

In addition to the depth structure of the T-S diagram, the first cruise exhibited a distinct spatial structure to the water mass present in the halocline (Fig. 3.9). On the south boundary of the Ocean Storms grid, the water in the halocline is warmer than the water on the west boundary of the grid. At station OS25, there is a transition between the two water masses. At this station, the cooler water mass (A) is found at the top of the halocline and the warmer water mass (B) is found at the bottom of the halocline. This transitional T-S diagram is also evident at stations OS20, OS15, OS11, and OS06. This spatial structure of temperature and salinity will become more evident in the next section.

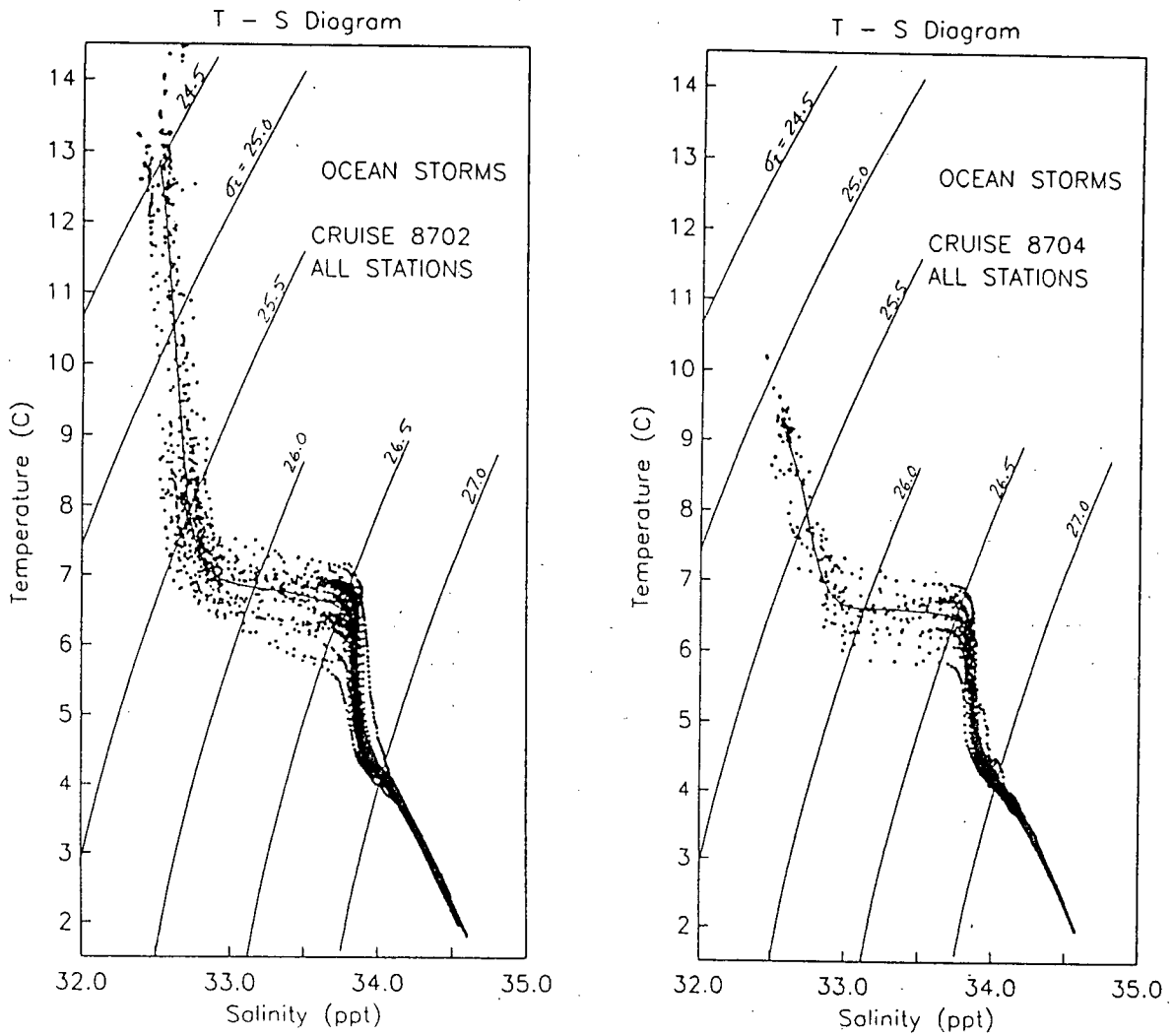


Figure 3.8: Temperature-Salinity (T-S) diagrams for the first cruise (8702) and for the second cruise (8704) for data obtained from the Ocean Storms area. In these plots the solid line represents the average T-S curve for that cruise.

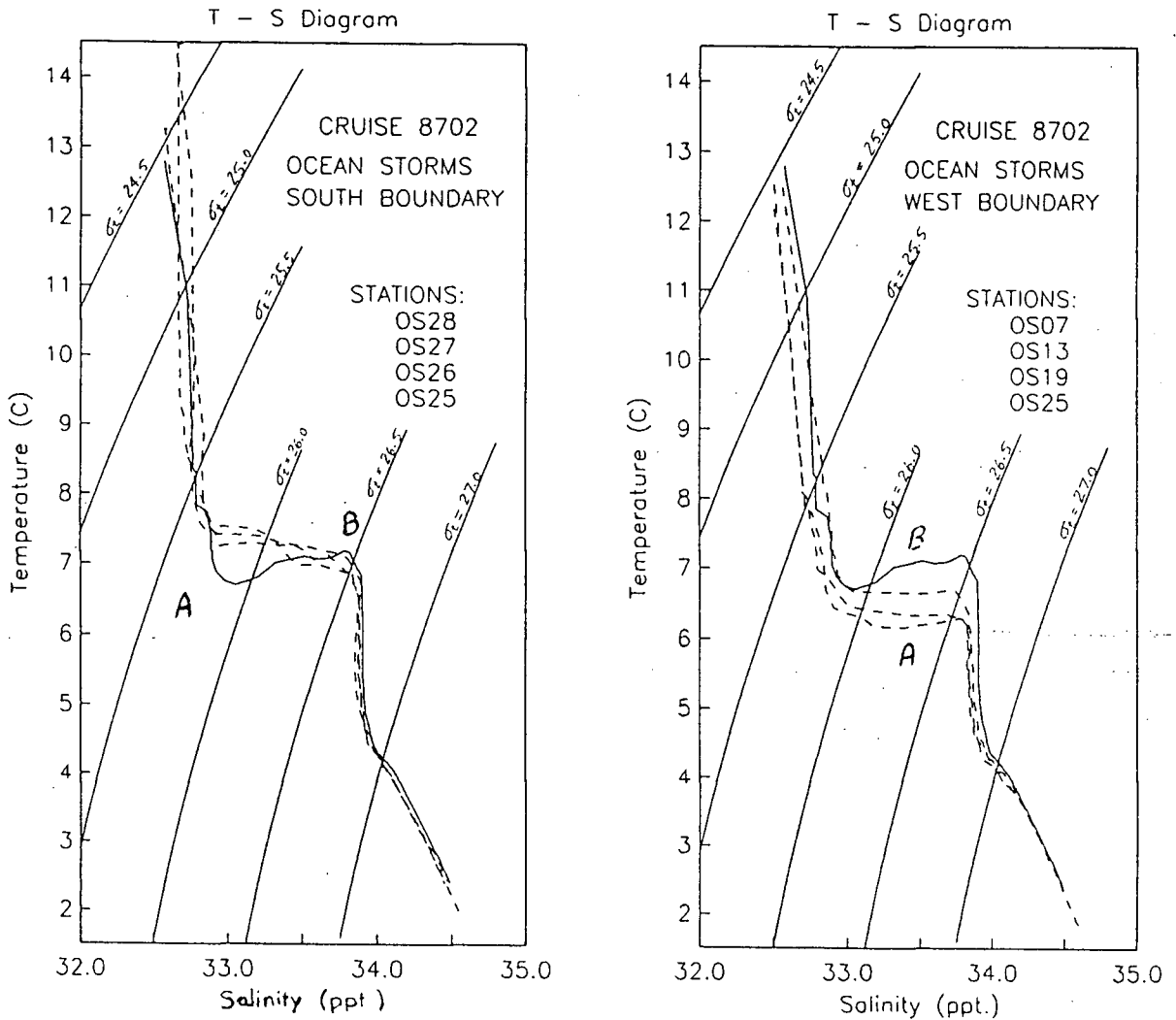


Figure 3.9: Spatial structure of the T-S diagram for cruise one (8702). The solid line represents the T-S curve from OS25. These plots show the presence of two different water masses (A) and (B) in the halocline.

### 3.2 The Horizontal Flow Field

To provide a qualitative picture of the flow field and define mesoscale features in the study area, maps of dynamic height are used. The flow field from these maps will then be related to the observed distribution of temperature and salinity on potential density surfaces,

and to the flow inferred from these distributions using isentropic analysis. To simplify the discussion of the flow field, the ocean will be divided into the three zones defined by the vertical structure of the temperature and salinity profiles, the upper "seasonal" zone, the principal halocline and the lower zone.

### 3.3 Dynamic Height

The maps of dynamic height presented in this section display the dynamic height in dynamic meters relative to a reference level of 1000 dbar. In these maps, the contour lines represent streamlines of the geostrophic flow.

For the first cruise, the dynamic height maps for the three zones are similar (Fig. 3.10). These maps reveal three distinctive features:

- 1) A prominent eddy near OS02 ( $48.6^{\circ}$  N and  $141.0^{\circ}$  W) is present in all zones. adjacent
- 2) A less well-defined eddy appears in the south, near station OS27 ( $46.4^{\circ}$  N and  $140.1^{\circ}$  W). Insufficient data exists to properly define this feature.
- 3) In the centre of the Ocean Storms grid, the geostrophic flow is smoother with the flow generally in a northeasterly direction.

As one goes to deeper levels this flow tends to rotate to the south; at a depth of 1500 dbar the flow is southerly. At this depth the flow in the centre of the Ocean Storms grid becomes more complicated with smaller eddy features in the centre of the grid.

The flow structure evident by the dynamic height maps for the second cruise (Fig. 3.11) revealed several changes from that of the first cruise. First, the eddy that was present near station OS02 ( $48.6^{\circ}$  N and  $141.0^{\circ}$  W) still exists but appears to have moved north, out of the Ocean Storms area. By the second cruise, the disturbance in the flow at station OS04 ( $48.6^{\circ}$  N and  $139.3^{\circ}$  W) has developed into a weak cyclonic eddy. Due

to the lack of data in the lower portion of the Ocean Storms grid for cruise two, it is difficult to infer the general flow pattern in the Ocean Storms area. It does appear that a northeasterly flow could be consistent with the observed data.

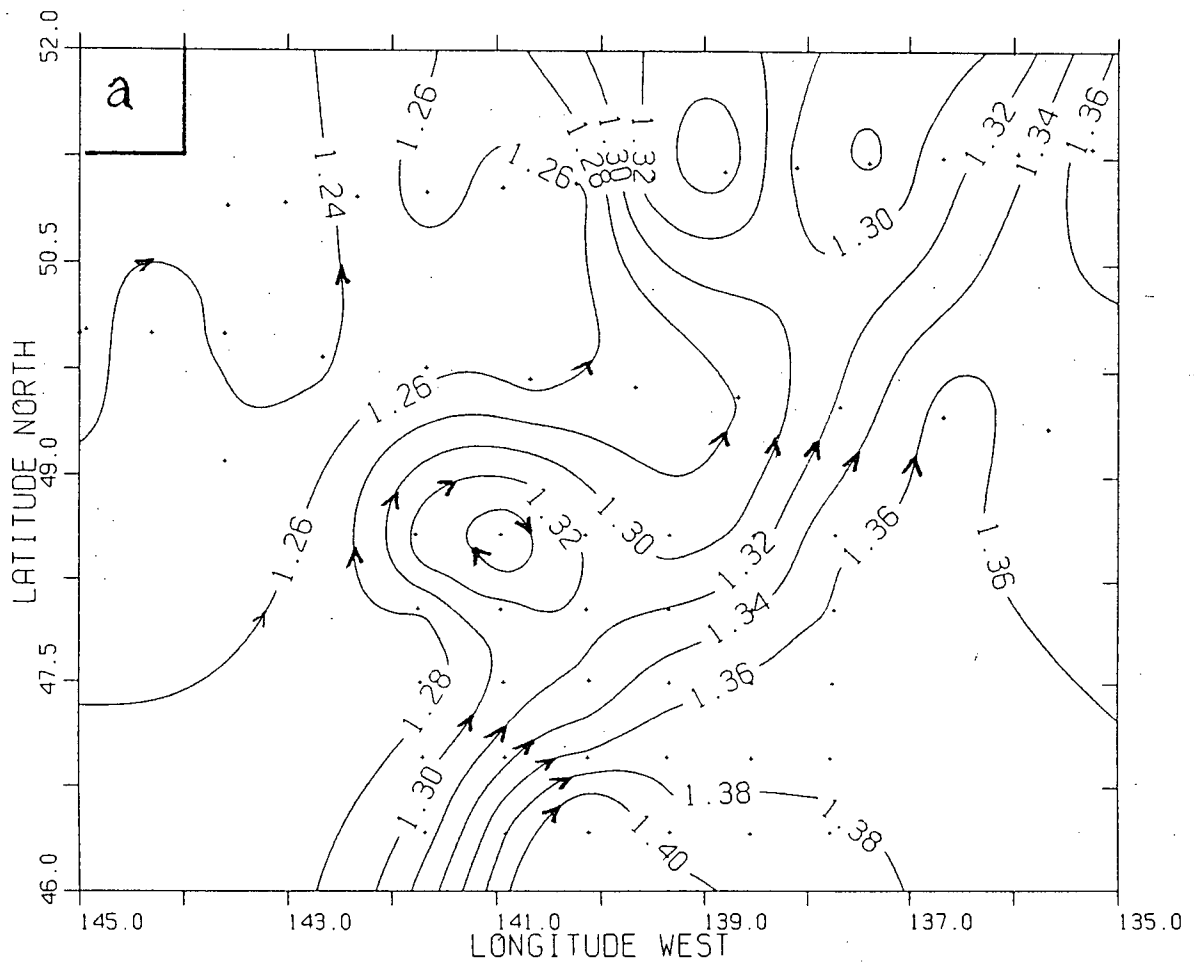
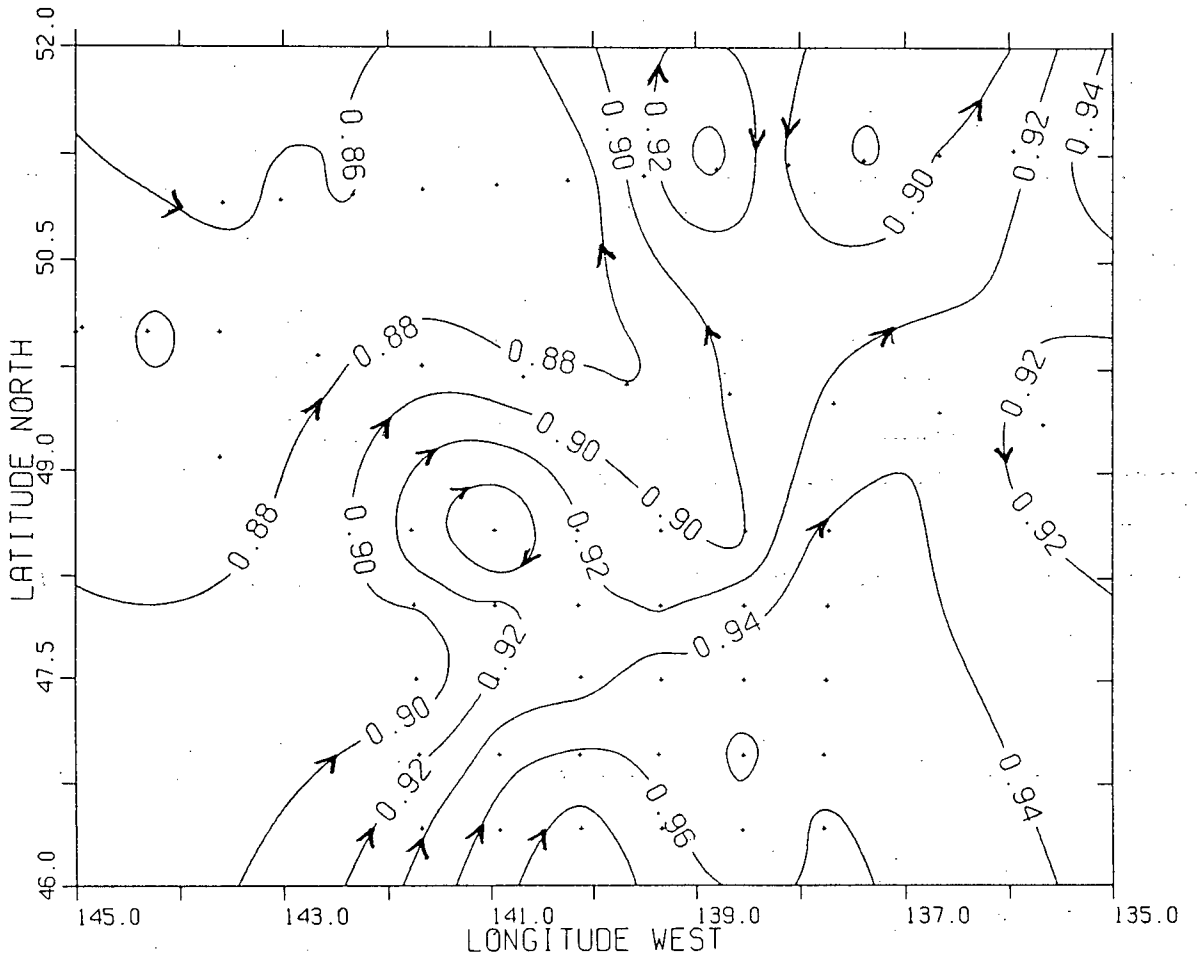
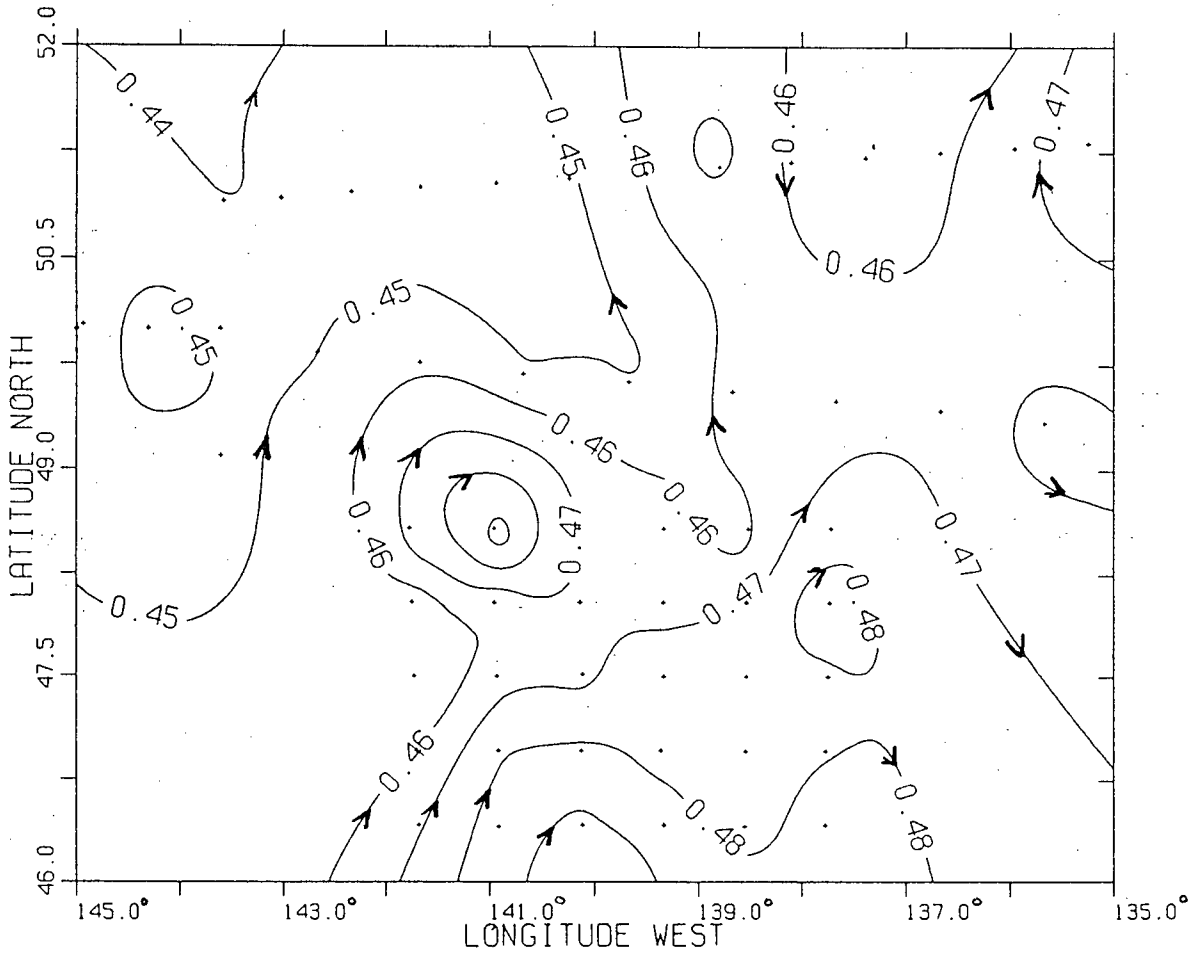


Figure 3.10: Cruise One: Dynamic Height in dynamic meters relative to 1000 dbar at: a) the surface, b) 150 dbar, c) 500 dbar. In these maps the arrows indicate the direction of the geostrophic flow and the dots denote the location of the STP stations obtained during this cruise.

(b)



(c)



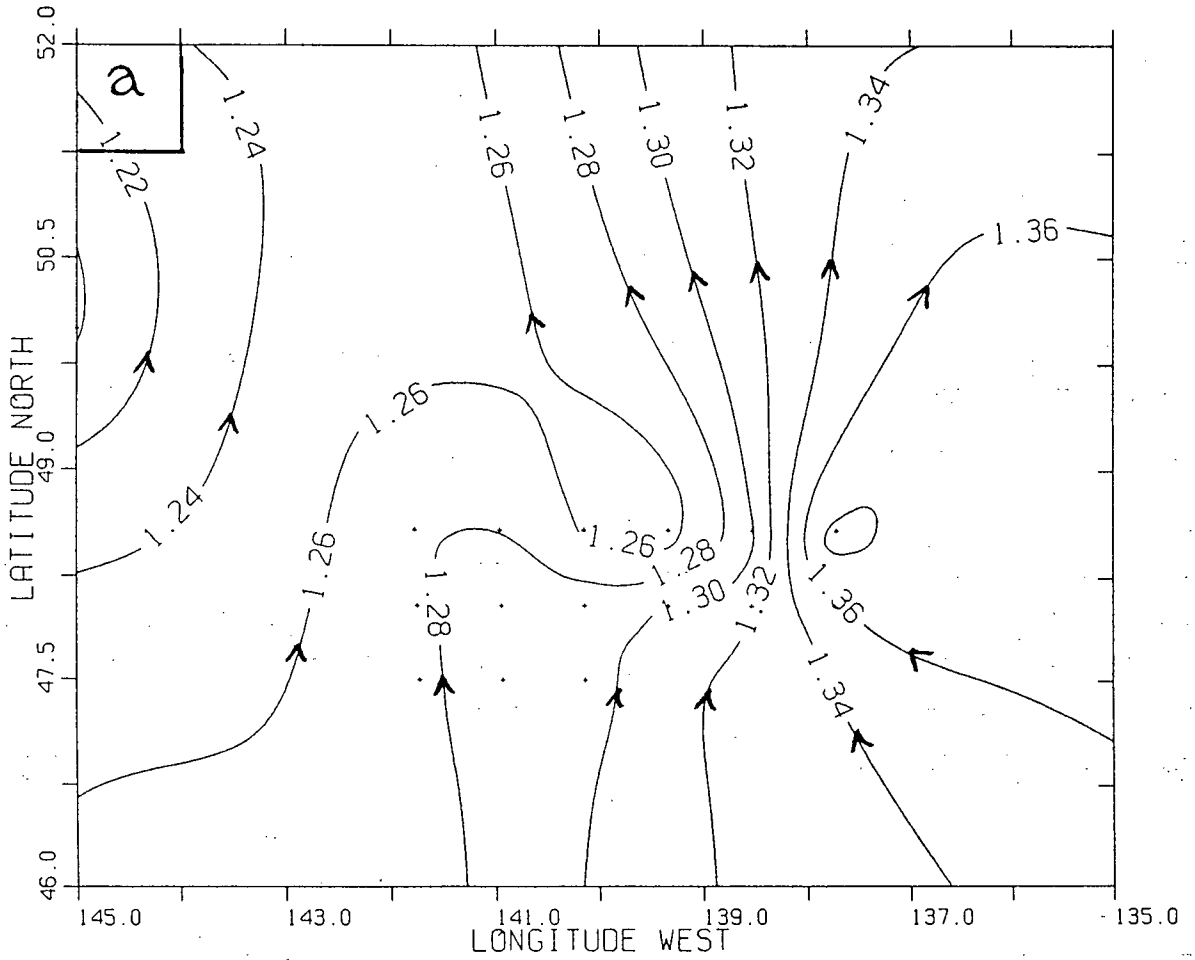
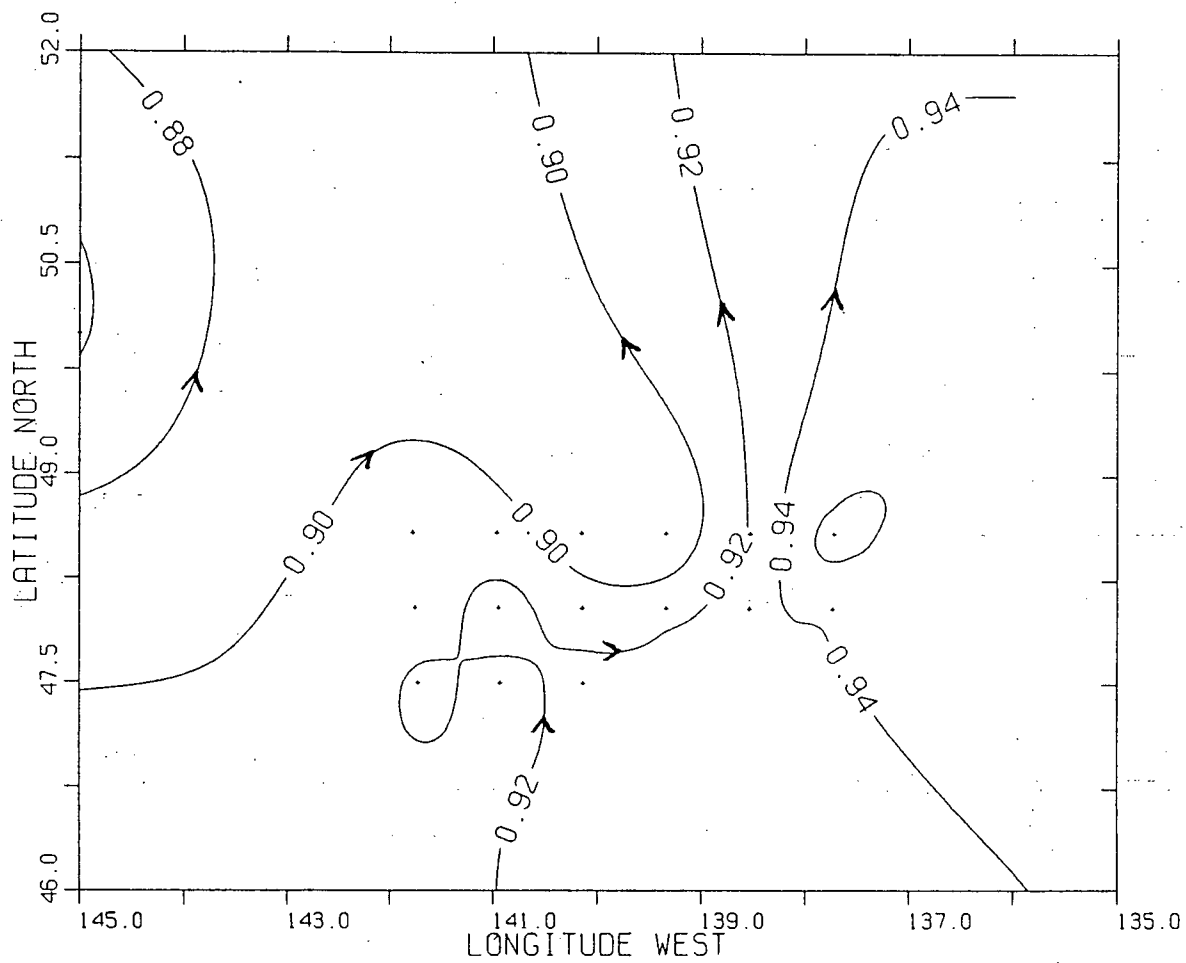
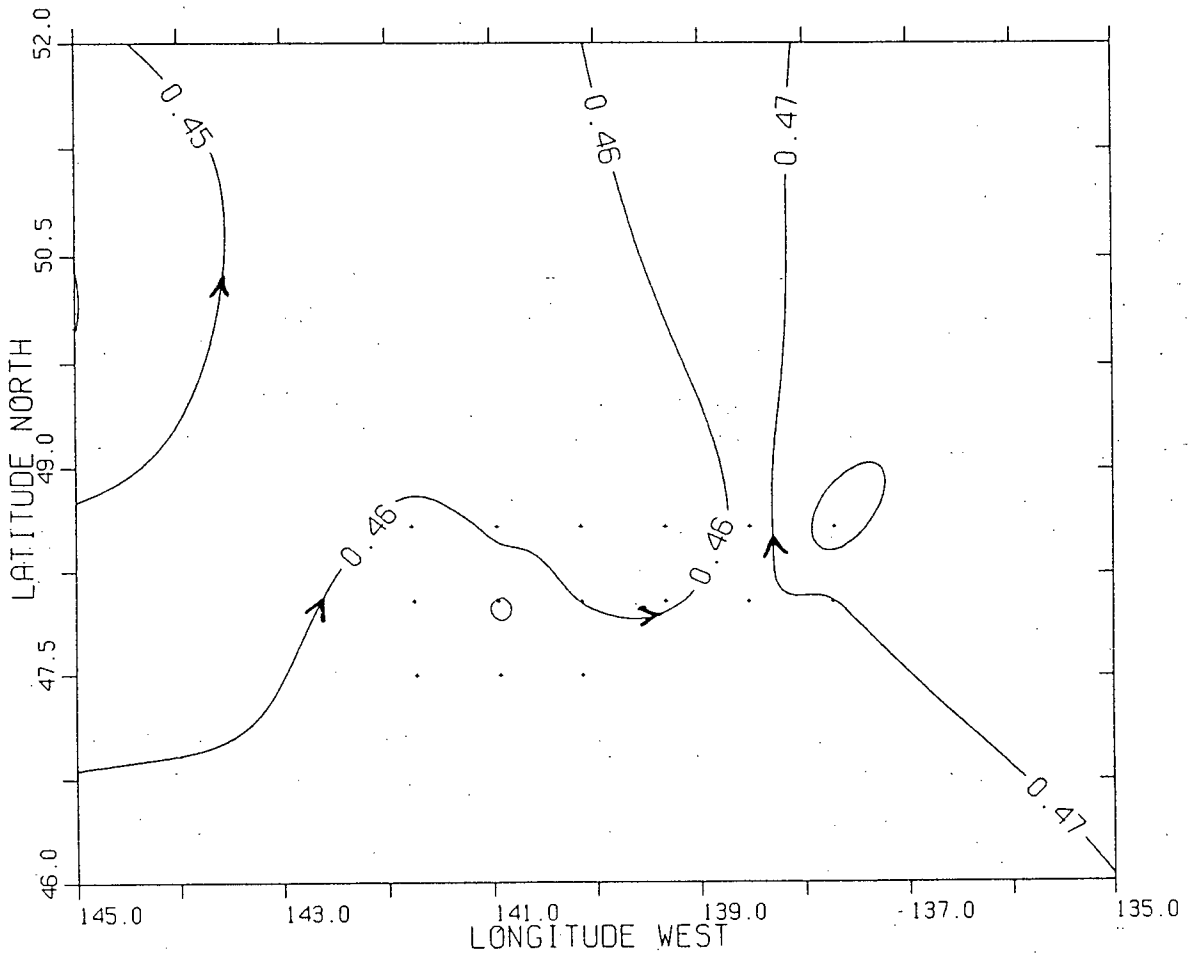


Figure 3.11: Cruise Two: Dynamic Height in dynamic meters relative to 1000 dbar at: a) the surface, b) 150 dbar, c) 500 dbar. In these maps the arrows indicate the direction of the geostrophic flow and the dots denote the location of the STP stations obtained during this cruise.

(b)



(c)



### 3.3.1 Horizontal Distribution of Temperature and Salinity

The horizontal distribution of temperature and salinity contain information on the flow field. In this section, the flow field will be inferred from the temperature and salinity field using isentropic analysis. This flow field will be related to the geostrophic flow evident in the maps of dynamic height.

Isentropic analysis is based on the idea that water preferentially moves along isentropic surfaces [3]. A qualitative description of the flow can be inferred directly from the distribution of the temperature and salinity on these isentropic surfaces. The bending and stretching of the contour lines of these properties are the result of the spatial features in the flow field. For example, the presence of an anomalously large flow in a confined area will stretch the contours of temperature and salinity in this area in the direction of the flow. In oceanography, these isentropic surfaces can be defined by surfaces of constant potential density ( $\sigma_t$ ) [3].

The distribution of temperature and salinity are considered for the three zones which are defined in the temperature and salinity depth profiles at depths comparable to the pressure surfaces used to display the dynamic height. The upper zone is represented by the  $\sigma_t = 25.0$  surface for cruise one and  $\sigma_t = 25.5$  surface for cruise two, the principal halocline by the  $\sigma_t = 26.2$  surface, and the lower zone by the  $\sigma_t = 27.0$  surface. To better define these distributions, STP stations outside the Ocean Storms grid are also included. On these maps, the arrows indicate the inferred direction of flow.

For the first cruise the upper "seasonal" zone is shown in Figure 3.12. These maps indicate that a tongue of warm salty water is moving through the southern part of the Ocean Storms grid in a northeasterly direction. This is similar to the dynamic height map for this zone which displays a strong northeasterly flow in this area (Fig. 3.10a). The geostrophic flow indicated by the dynamic height map would tend to stretch the contours

of temperature and salinity in the direction of this flow. However, the flow inferred from isentropic analysis is more easterly than the geostrophic flow. This indicates the presence of an additional component to the flow. Also present in the temperature and salinity fields in this zone is an oceanic front in the centre of the grid separating the warm salty water in the south from the colder fresher water in the north. Such a feature is not evident in the dynamic height map. Also, the current pattern evident from the temperature and salinity fields gives more details about the flow field than what was evident in the map of dynamic height.

The situation in the halocline for this cruise is very similar (Fig. 3.13). A tongue of warm salty water still appears to be moving through the southern half of the grid in a northeasterly direction. This flow is slightly more northerly than that which was observed in the upper zone. This feature is consistent with the geostrophic flow inferred from the dynamic height map (Fig. 3.10b). A ring of warm salty water is present in this zone in the northwestern corner of the grid. This ring defines the prominent eddy evident in the dynamic height map. The oceanic front still exists in the centre of the grid separating the warm salty water from the colder fresher water. This front observed in the T-S diagrams (Fig. 3.9) cuts through the Ocean Storms grid in a northeasterly fashion.

In the lower zone, the temperature and salinity fields no longer display the presence of the oceanic front (Fig. 3.14). Instead, in the centre of the grid the temperature and salinity fields show no significant flow features this is consistent with the map of dynamic height which indicate that the flow in this area is weak (Fig. 3.10c). The temperature and salinity fields do show that a tongue of cold fresh water is moving southeasterly through the eastern half of the grid and that a tongue of warm salty is moving north in the southeastern corner of the grid. The former feature is not clearly evident in the map of dynamic height but the latter flow feature is. The prominent eddy present in the map

of dynamic height is well-defined in the temperature and salinity fields by a ring of warm salty water near OS02 (48.6° N and 141.0° W).

For the second cruise, the pattern has changed from what was observed in cruise one (Figs. 3.15). In the upper zone the contour lines are meridional and lack any prominent features. In the halocline the pattern is similar, but there is more evidence of a tongue of cold fresh water moving south through the northern part of the grid (Figs. 3.16). In the lower zone this tongue of water still exists but is less prominent (Fig. 3.17). For the second cruise, flow in all zones appear to be north-south which is similar only to the lower zone of cruise one. The analysis of the second cruise is subjective because of the lack of data in the south sections of the grid. This flow is generally comparable to the dynamic height maps but again the lack of data makes the comparison very subjective.

### 3.4 Summary

It is evident in the closely spaced grid of stations in the Ocean Storms area that several mesoscale features existed in this relatively quiet area of the open ocean. It was interesting to observe that in previous maps of dynamic height at the surface, an eddy did occur near the eddy observed in this data at OS02 (48.6° N and 141.0° W) [17]. The existence of eddies in this area with spatial scales of 50 -100 km have been previously observed by Tabata along line P [14].

The circulation pattern deduced from the isentropic analysis is generally consistent with the dynamic height maps. Therefore, the results of the isentropic analysis are considered as supporting any conclusion reached from considering the flow is geostrophic. However, isentropic analysis does reveal more details in the current pattern than what is evident in the maps of dynamic height. This suggests that additional information about the flow field is available from the temperature and salinity data than just using this

data to calculate the dynamic height.

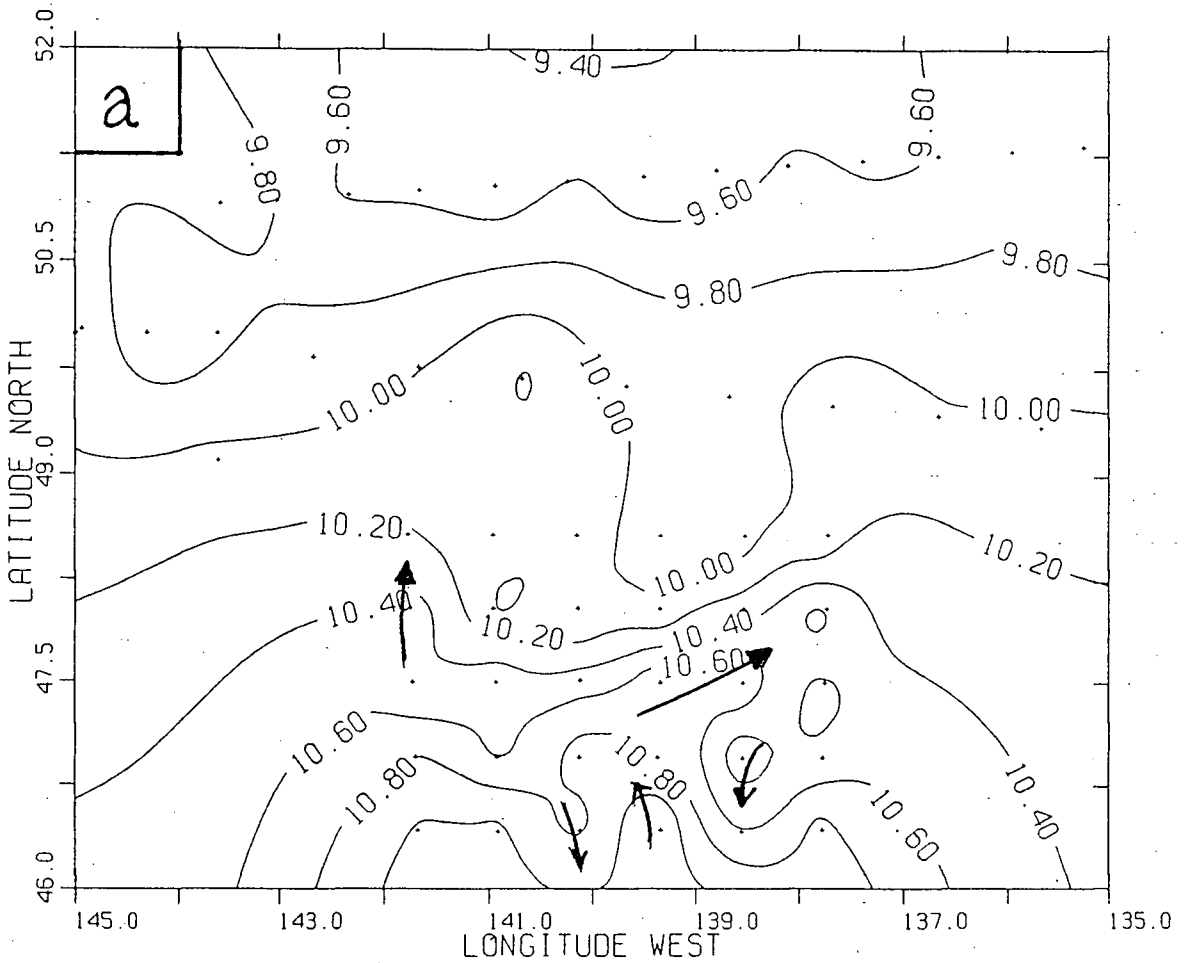
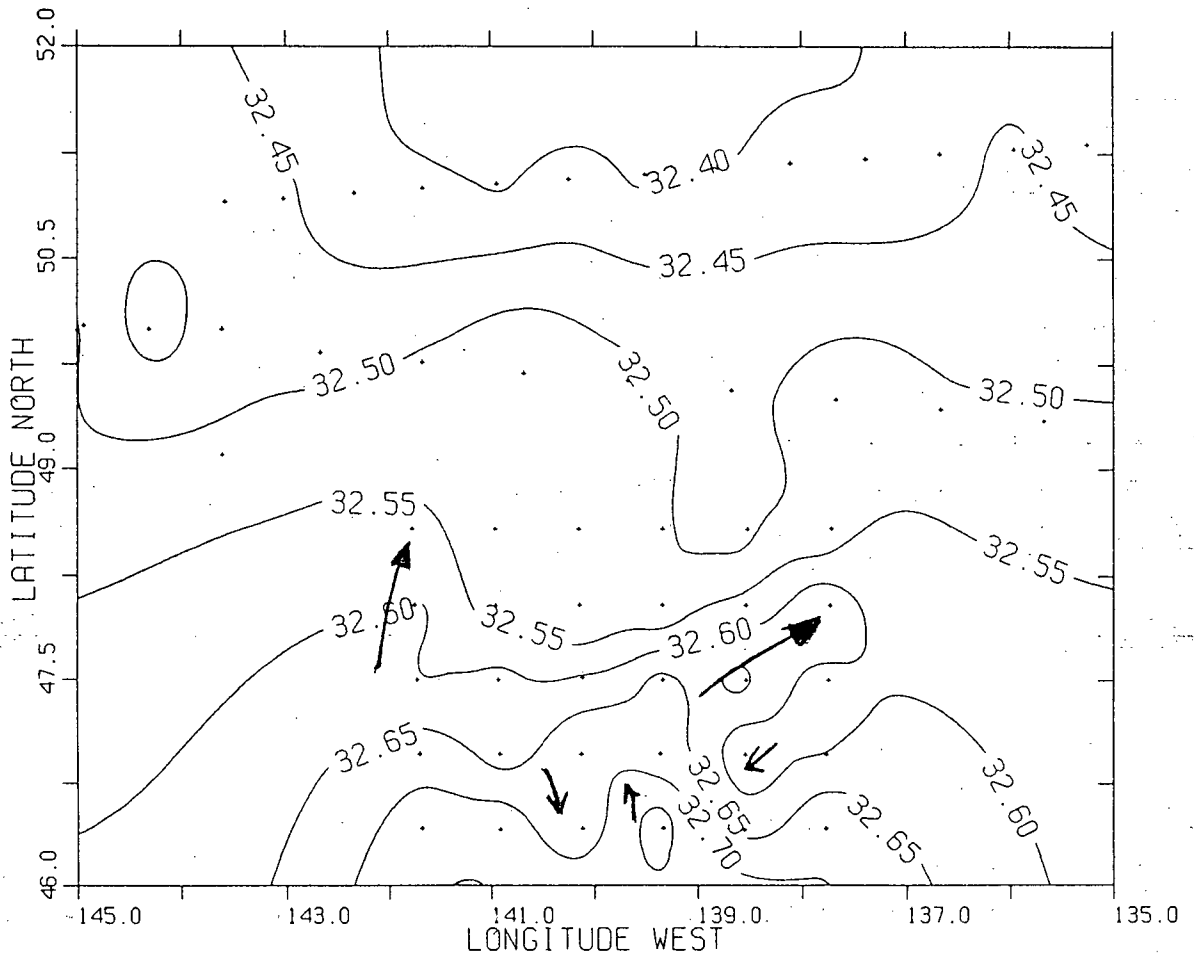


Figure 3.12: Temperature and Salinity distribution for cruise one on the  $\sigma_t = 25.0$  surface for: a) the temperature distribution in deg C, and b) the salinity distribution in ppt. The arrows in these maps indicate the interpretative current pattern.

(b)



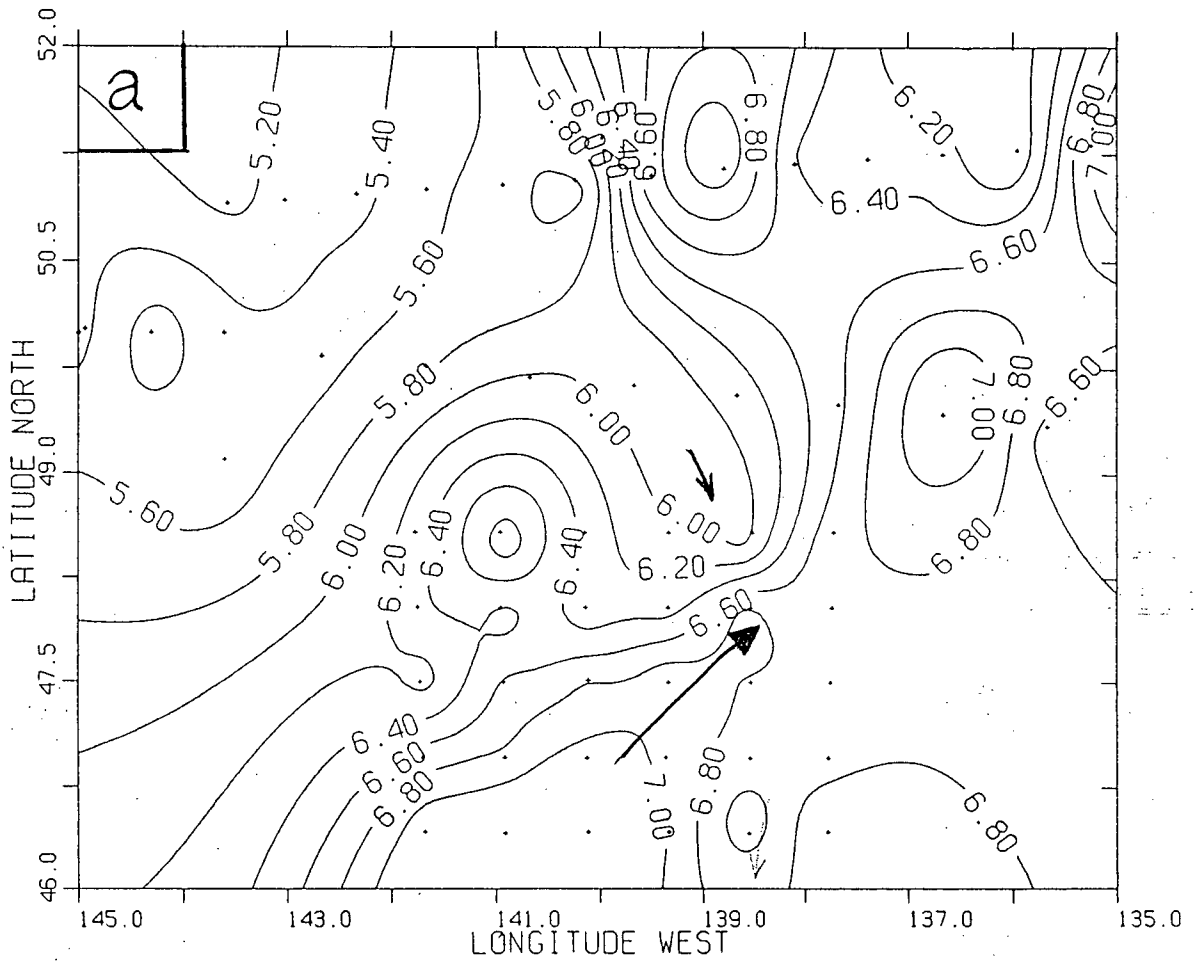
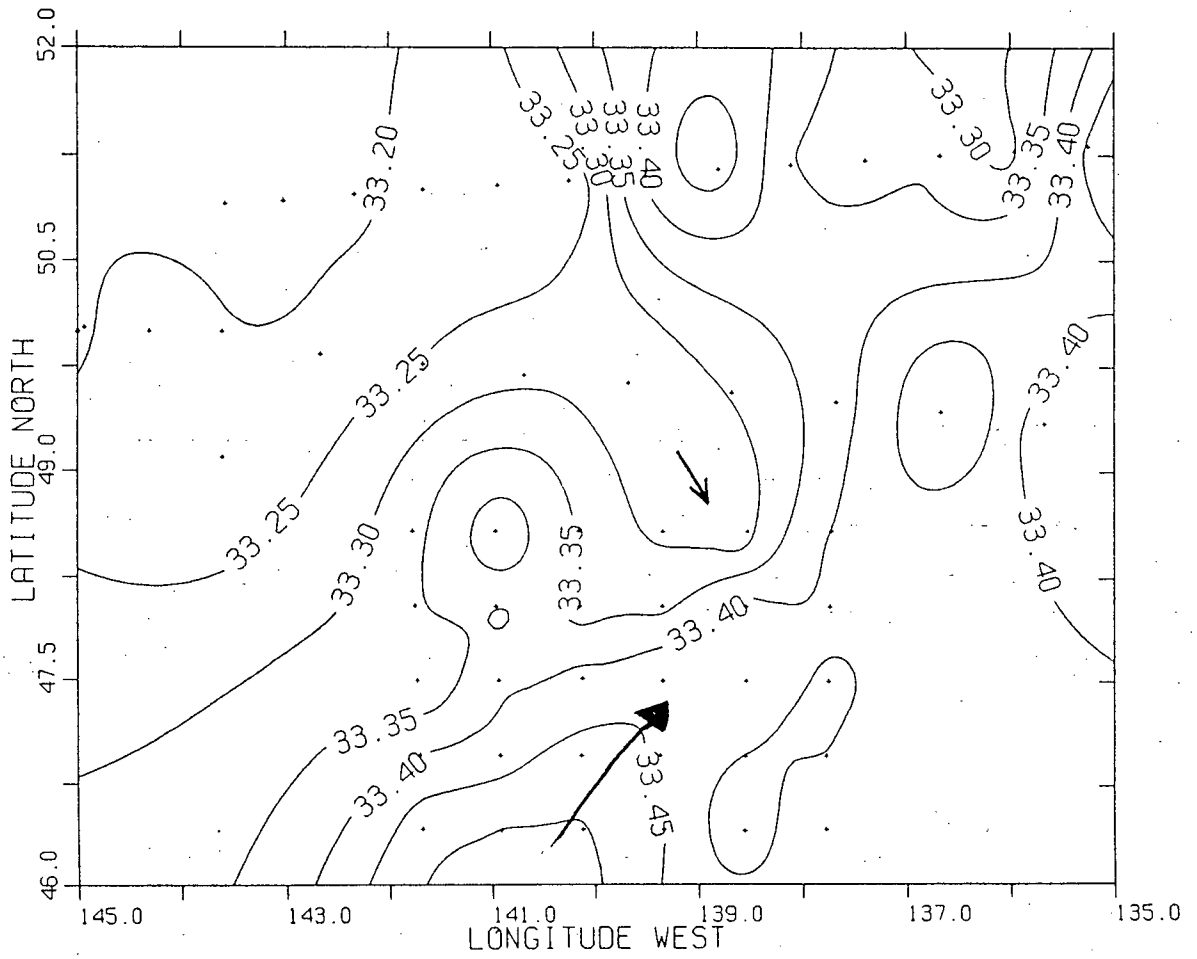


Figure 3.13: Temperature and Salinity distribution for cruise one on the  $\sigma_t = 26.2$  surface for: a) the temperature distribution in deg C, and b) the salinity distribution in ppt. The arrows in these maps indicate the interpretative current pattern.

(b)



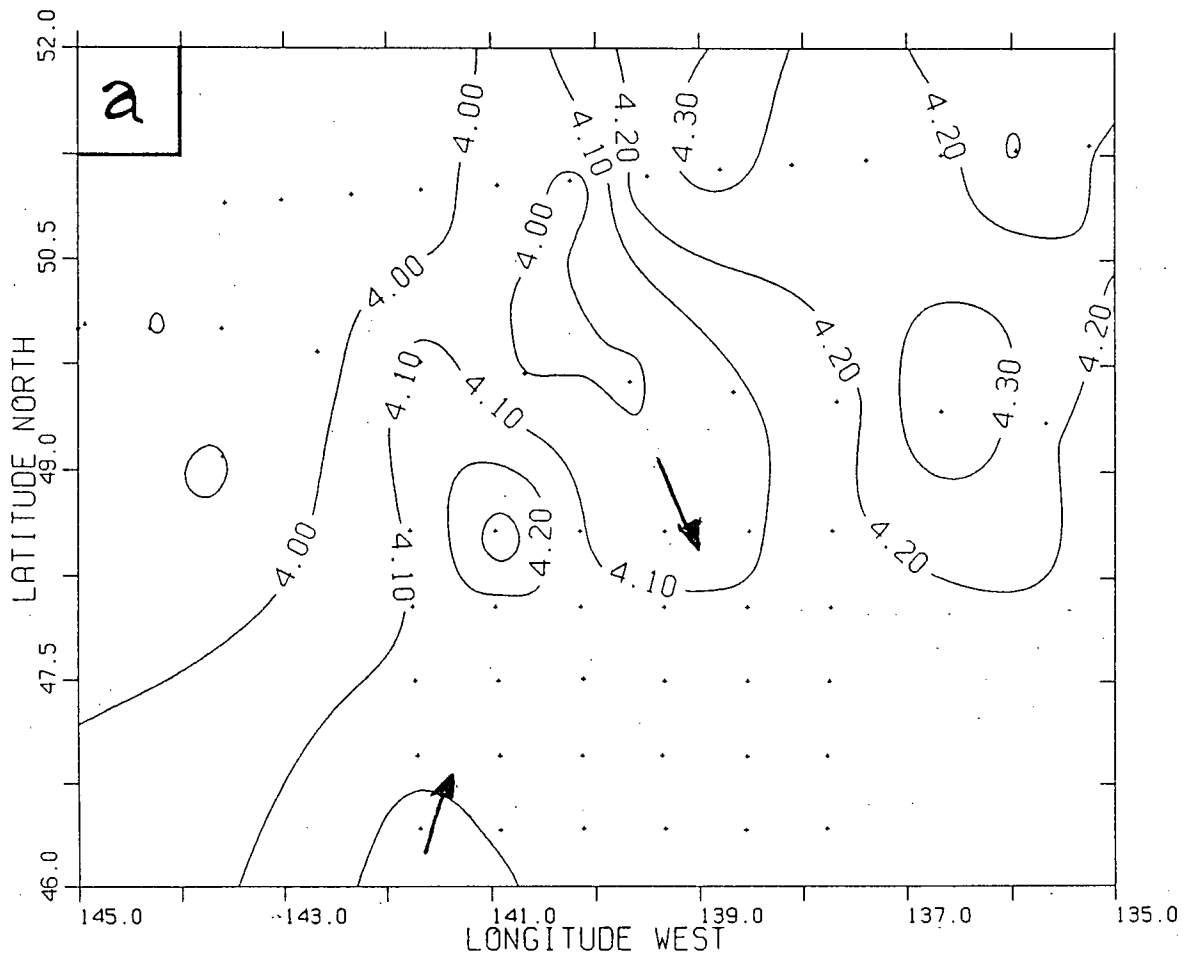
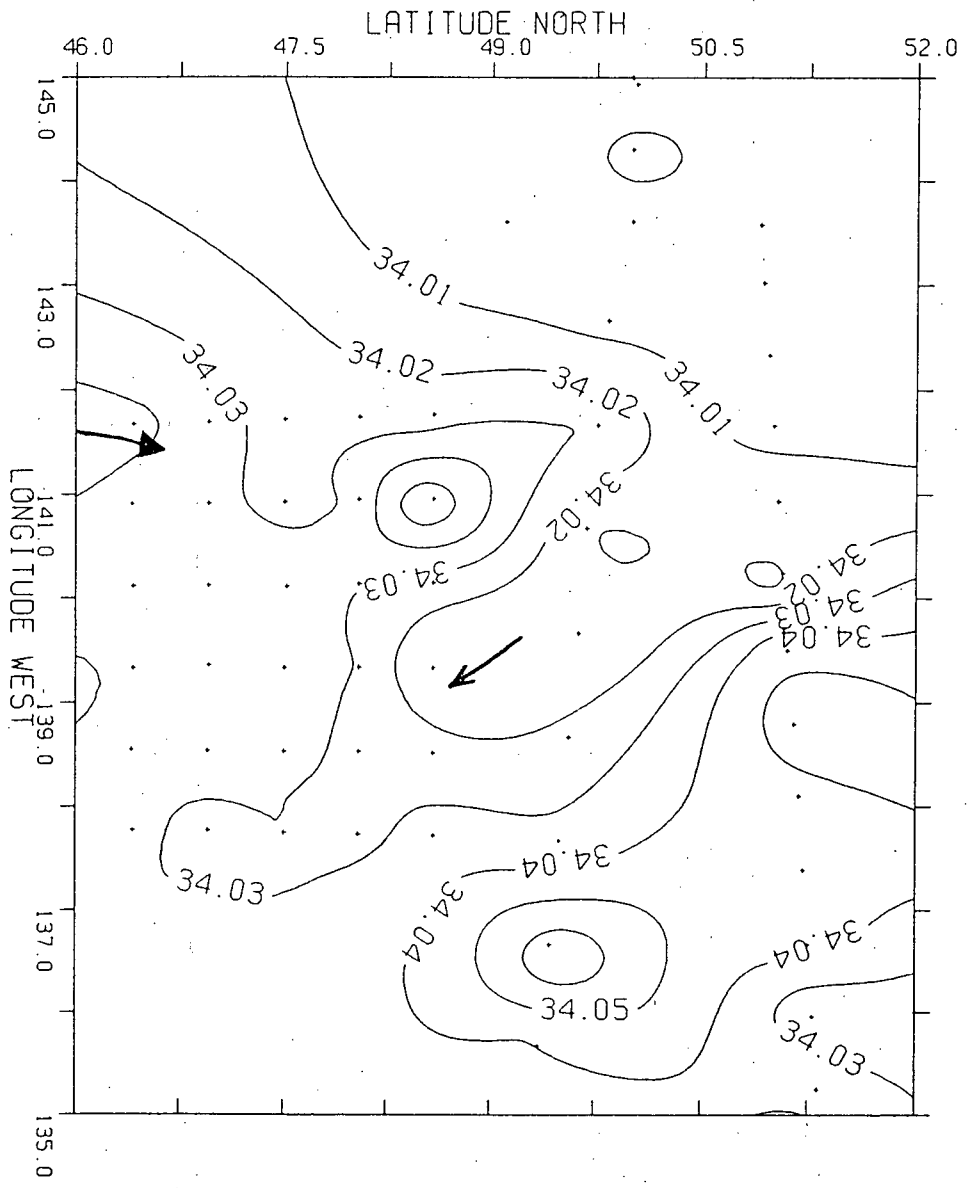


Figure 3.14: Temperature and Salinity distribution for cruise one on the  $\sigma_t = 27.0$  surface for: a) the temperature distribution in deg C, and b) the salinity distribution in ppt. The arrows in these maps indicate the interpretative current pattern.

(b)



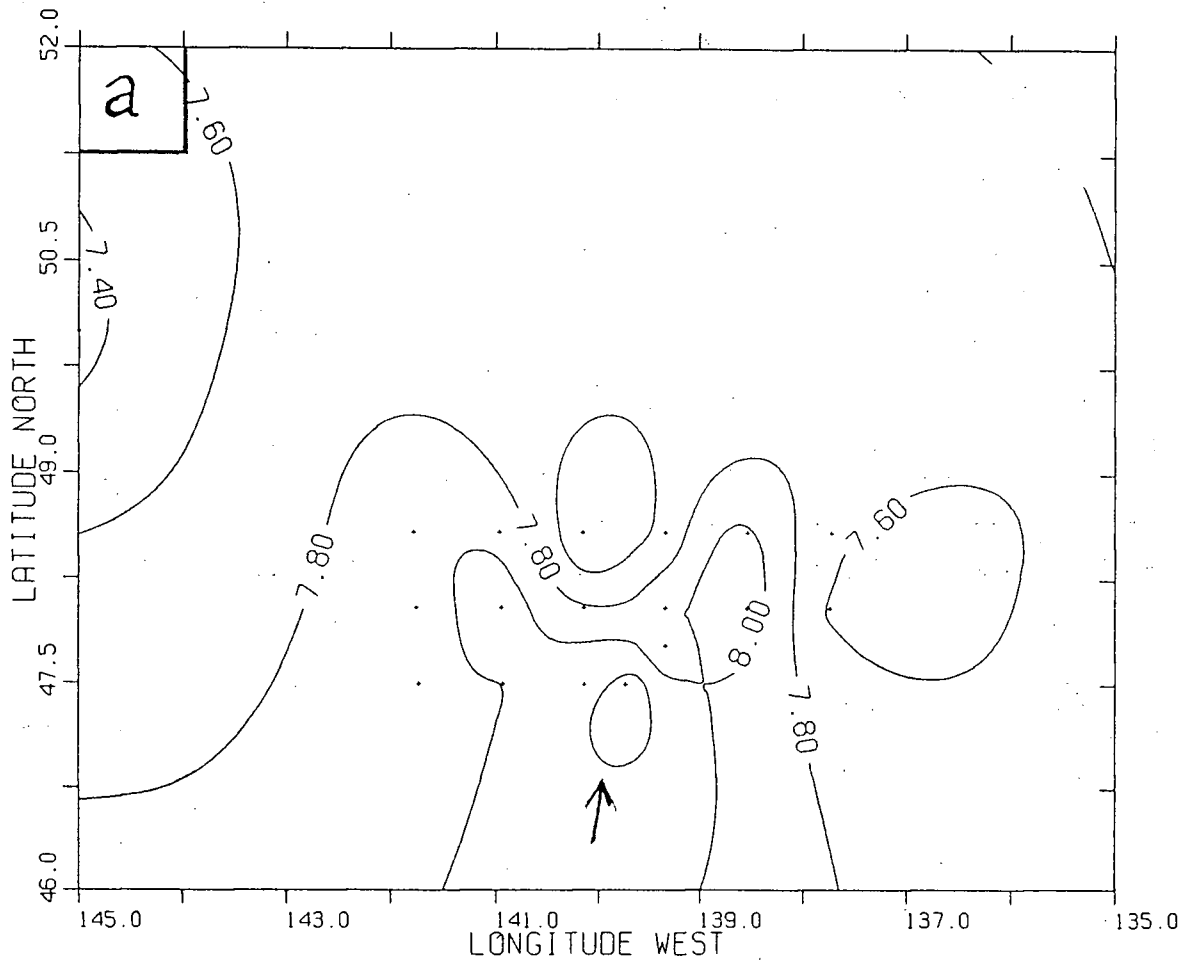
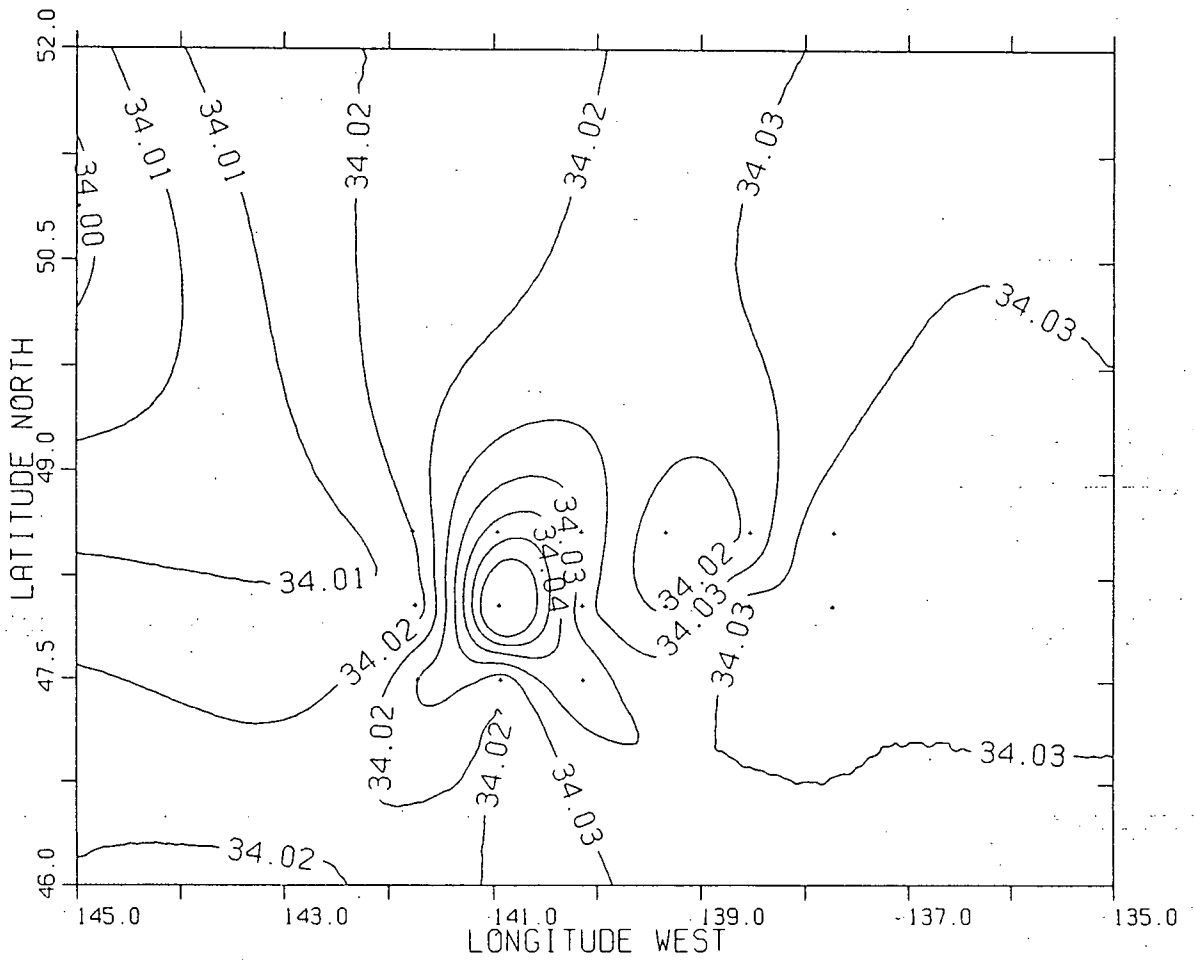


Figure 3.15: Temperature and Salinity distribution for cruise two on the  $\sigma_t = 25.5$  surface for: a) the temperature distribution in deg C, and b) the salinity distribution in ppt. The arrows in these maps indicate the interpretative current pattern.

(b)



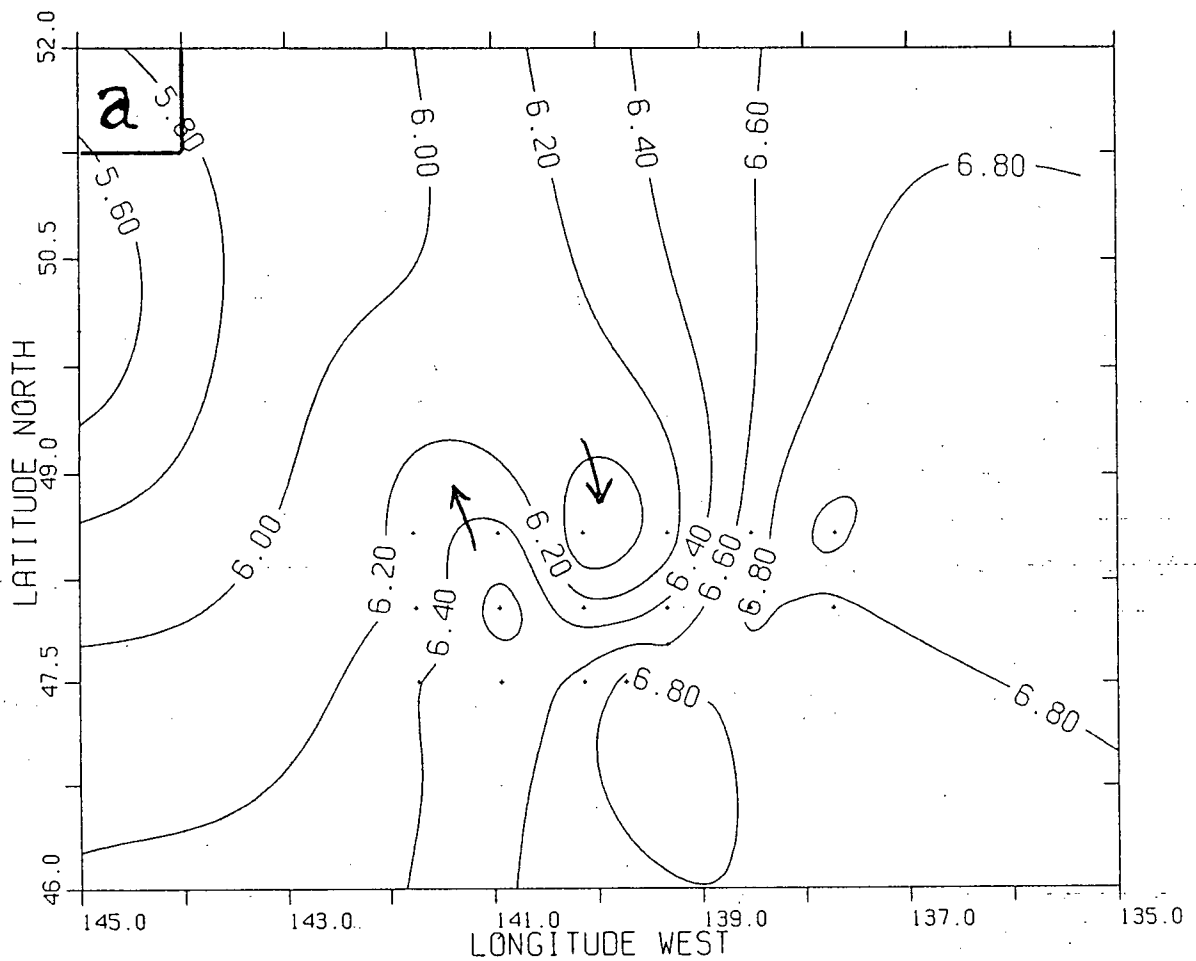
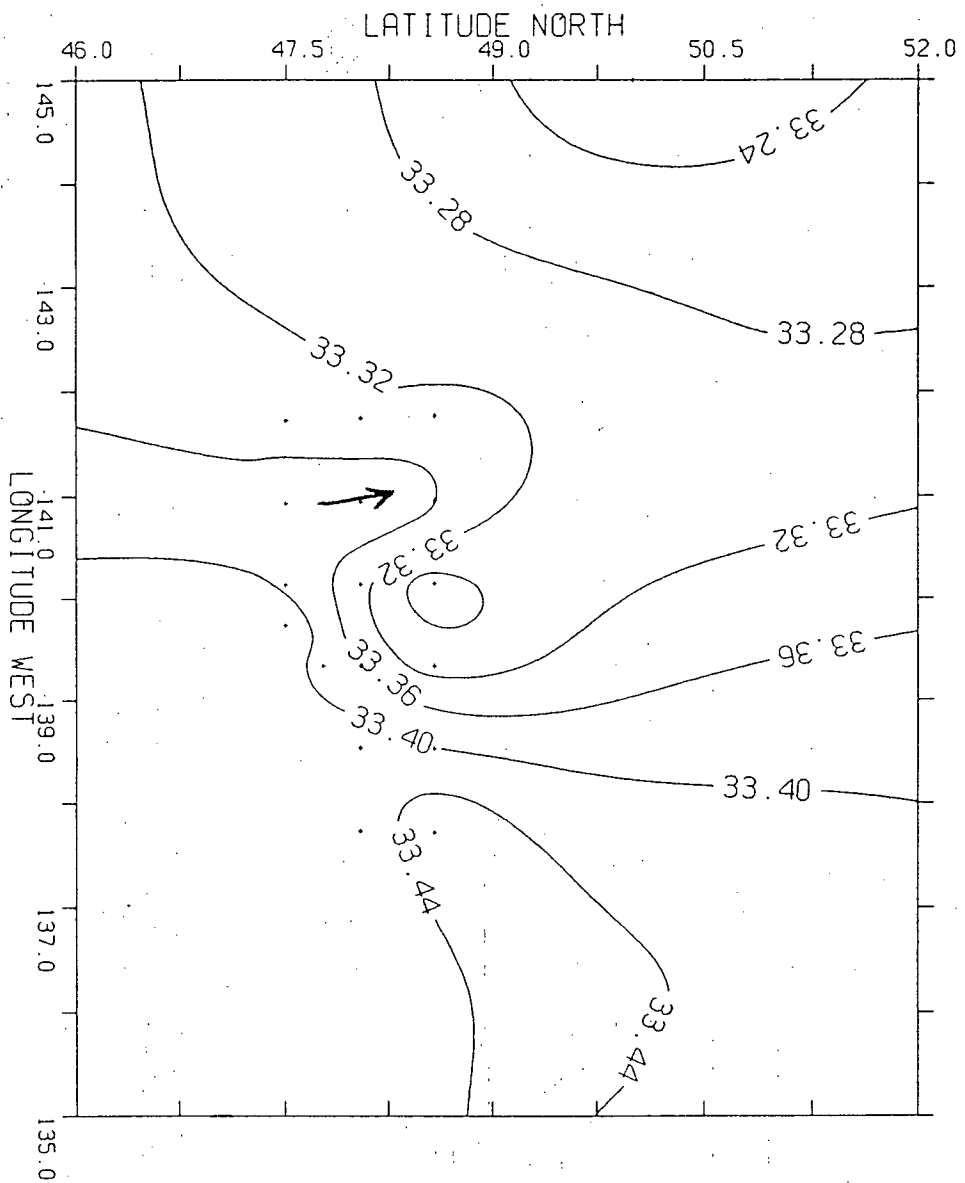


Figure 3.16: Temperature and Salinity distribution for cruise two on the  $\sigma_t = 26.2$  surface for: a) the temperature distribution in deg C, and b) the salinity distribution in ppt. The arrows in these maps indicate the interpretative current pattern.

(b)



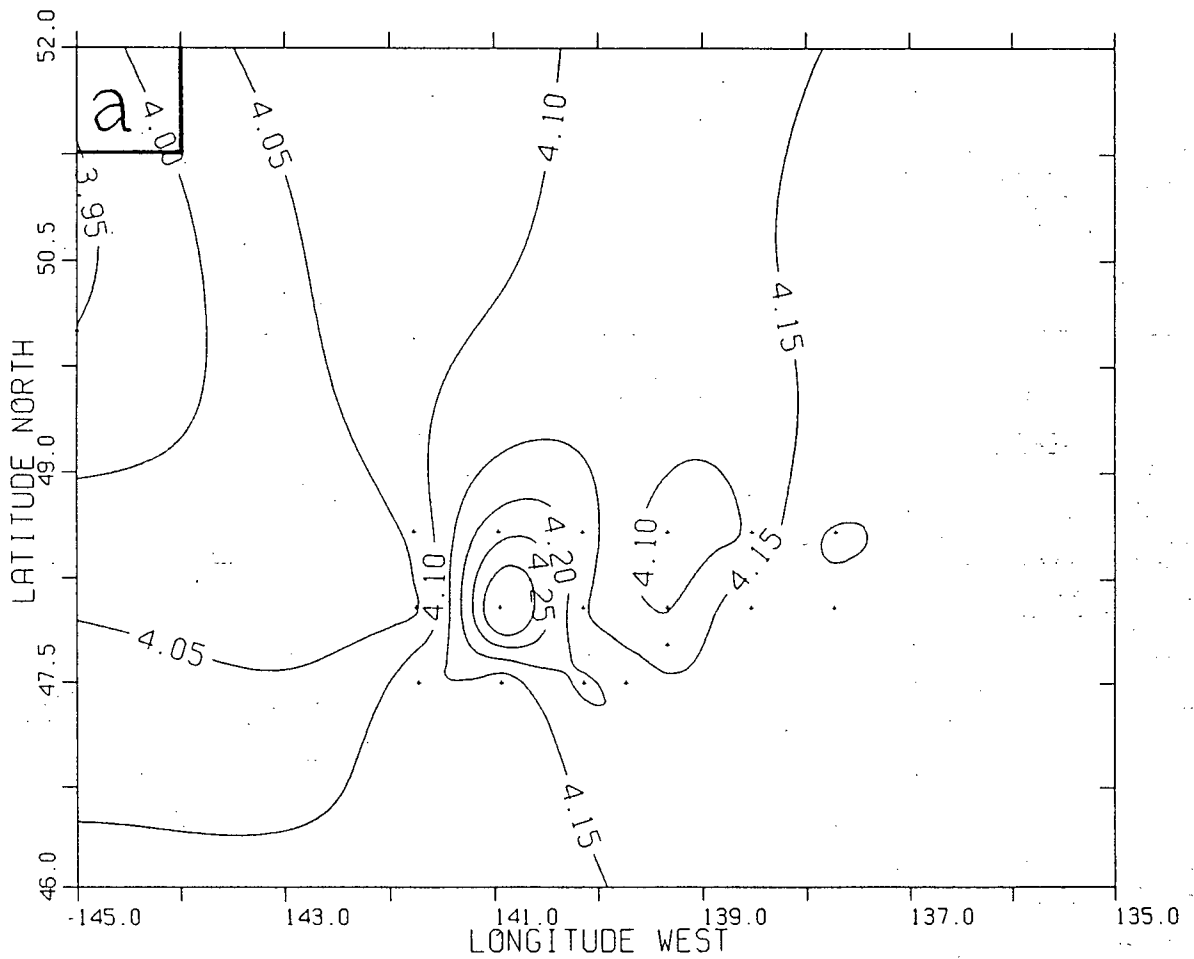
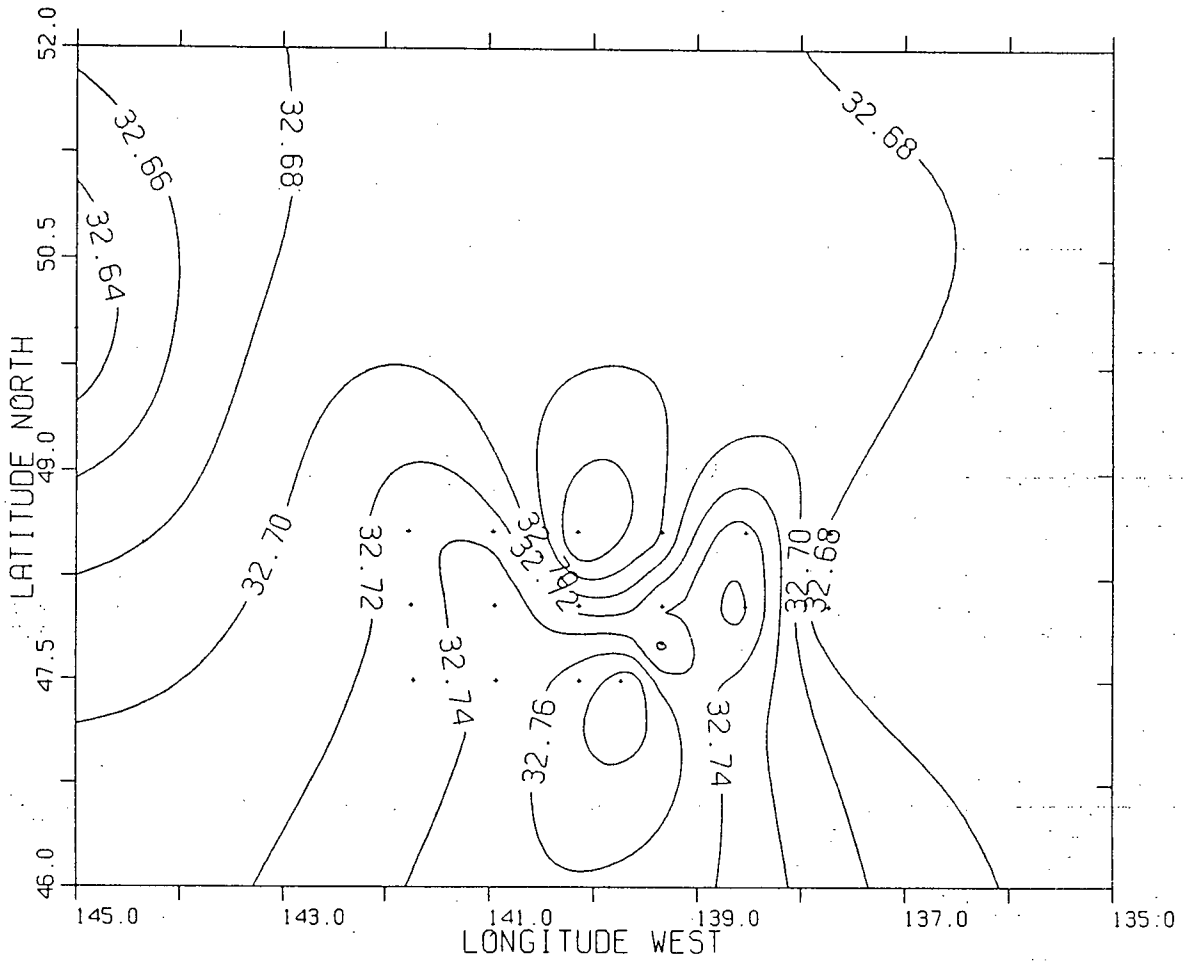


Figure 3.17: Temperature and Salinity distribution for cruise two on the  $\sigma_t = 27.0$  surface for: a) the temperature distribution in deg C, and b) the salinity distribution in ppt. The arrows in these maps indicate the interpretative current pattern.

(b)



## Chapter 4

### Developing and Solving the Inverse Problem

#### 4.1 Determining the Ocean Circulation: The Physical Problem

The method to be presented in this thesis for obtaining ocean circulation from temperature and salinity information is based on the following approximations to the equations of motion. In cartesian coordinates, the equations of motion with the hydrostatic approximation and conservation of mass are

$$u_t + uu_x + vv_y - fv = -\frac{1}{\rho}p_x \quad (4.4)$$

$$v_t + uv_x + vv_y + fu = -\frac{1}{\rho}p_y \quad (4.5)$$

$$p_z = -\rho g \quad (4.6)$$

$$u_x + v_y + w_z = 0 \quad (4.7)$$

The Coriolis parameter is defined as  $f = (f_o + \beta y)$ . By assuming the flow is linear and steady state, and using the Boussinesq approximation, (4.4) and (4.5) can be reduced to the geostrophic equations

$$fv = \frac{1}{\rho_o}p_x \quad (4.8)$$

$$fu = -\frac{1}{\rho_o}p_y \quad (4.9)$$

Differentiating (4.8) and (4.9) with respect to  $z$  and using (4.6) leads to the thermal wind equations

$$fv_z = -\frac{1}{\rho_o}g\rho_x \quad (4.10)$$

$$fu_z = \frac{1}{\rho_0} g \rho_y \quad (4.11)$$

The thermal wind equations relate the vertical shear of the horizontal velocities to the horizontal gradient of the in situ density,  $\rho$ . If (4.10) and (4.11) are now integrated vertically from a reference depth,  $z_r$ , the horizontal velocity is given by

$$v = -\frac{g}{\rho_0 f} \int_{z_r}^z \rho_x dz + v_o = v_r + v_o \quad (4.12)$$

$$u = +\frac{g}{\rho_0 f} \int_{z_r}^z \rho_y dz + u_o = v_r + v_o \quad (4.13)$$

The horizontal velocities are made up of two terms. The first term, the relative velocity ( $u_r, v_r$ ), depends only on horizontal gradients in the density field. The second term is the constant of integration, ( $u_o, v_o$ ), and it refers to the velocity at the reference level  $z_r$ .

By measuring the temperature and salinity distributions at different depths, one can obtain the density field using the equation of state ( $\rho(S, T, P)$ ). Knowing the density field, the relative velocities given in (4.12) and (4.13) can be evaluated.

By differentiating (4.8) with respect to  $y$  and (4.9) with respect to  $x$ , and adding them together, one obtains a linear  $\beta$ -plane vorticity conservation equation

$$\beta v = fw_z \quad (4.14)$$

Integrating this equation from a reference level  $z_r$  one obtains

$$w = \frac{\beta}{f} \int_{z_r}^z v dz + w_o \quad (4.15)$$

The variable  $w_o$  arises from the constant of integration and it refers to the vertical velocity at the reference level  $z_r$ . Using (4.12), one can rewrite (4.15) as

$$w = \frac{\beta}{f} \int_{z_r}^z v_r dz + \frac{\beta}{f} v_o (z - z_r) + w_o = w_r + \frac{\beta}{f} v_o (z - z_r) + w_o \quad (4.16)$$

To evaluate these unknown reference velocities,  $u_o, v_o$ , and  $w_o$ , the equations for conservation of mass (4.7) and conservation of salt and heat are used. The equations for

conserving heat and salt are defined by the following advection diffusion equations

$$uS_x + vS_y + wS_z = \vec{\nabla}(k\vec{\nabla}S) \quad (4.17)$$

$$uT_x + vT_y + wT_z = \vec{\nabla}(k\vec{\nabla}T) \quad (4.18)$$

These equations assume that the ocean is in a steady-state condition with no sources or sinks. Since this assumption is clearly violated at the surface of the ocean, the depth at which these equations are valid must be considered in order to properly apply them to the data available.

The conservation of heat is equivalent to the conservation of temperature multiplied by the heat capacity  $\rho C$ . Over the range of temperatures, salinities, and pressures in the ocean, this term can be considered constant and thus eliminated from (4.18). This allows the conservation of heat equation to be replaced by the conservation of temperature equation.

The variable  $k$  in (4.17) and (4.18) is referred to as the mixing coefficient. This variable parametrizes mixing due to eddies or other features not resolved by the model. In a stratified ocean, mixing along isopycnals is much stronger than cross isopycnal mixing [6]. In the Ocean Storms area the slope of the isopycnal surfaces are almost horizontal. This enables one to replace the isopycnal and diapycnal mixing coefficients by vertical and horizontal mixing coefficients,  $k_z$  and  $k_h$  respectively. This simplification should not introduce large errors because these mixing terms do not play a crucial role of transporting heat and salt in the Ocean Storms area. Because of the small area covered by the data (250 km by 200 km), the mixing coefficients are only considered to be functions of depth. The horizontal variations of these mixing coefficients were ignored.

I now proceed to show how these conservation equations are used to formulate an inverse problem to describe the flow in the ocean.

## 4.2 The Inverse Problem

### 4.2.1 Formulation

To develop a set of equations from the conservation equations, first consider one box in Figure 4.18. This box is bounded horizontally by four hydrographic stations and vertically by two depth surfaces,  $z_1$  and  $z_2$ . The velocity and the mixing coefficients on each face of the box must be determined. For each of these faces, a value for the relative velocity can be determined using the bounding hydrographic stations (equations (4.12), (4.13) and (4.16) ). Only the velocities directed perpendicular to the box faces can be determined. In this scheme no information is available to constrain the flow parallel to the faces of the box.

The conservation of mass constraint for this box can be obtained by integrating the conservation of mass equation around the region enclosed by the box.

$$\iiint \vec{\nabla} \cdot \vec{u} \, dx \, dy \, dz = 0 \quad (4.19)$$

$$\Delta y \, \Delta z \, \bar{u} \Big|_E^W + \Delta x \, \Delta z \, \bar{v} \Big|_S^N + \Delta x \, \Delta y \, \bar{w} \Big|_B^T = 0 \quad (4.20)$$

The overbar denotes the average velocity on each face of the box, with the subscripts E, W, N, S, T, and B referring respectively to the east, west, north, south, top, and bottom faces of the box. By writing the velocities in terms of known relative velocities and unknown reference velocities, one obtains the following equation

$$\begin{aligned} \Delta y \, \Delta z \, u_o \Big|_E^W + \Delta x \, \Delta z \, v_o \Big|_S^N + \Delta x \, \Delta y \, w_o \Big|_B^T = \\ - \Delta y \, \Delta z \, \bar{u}_r \Big|_E^W - \Delta x \, \Delta z \, \bar{v}_r \Big|_S^N - \Delta x \, \Delta y \, \bar{w}_r \Big|_B^T \end{aligned} \quad (4.21)$$

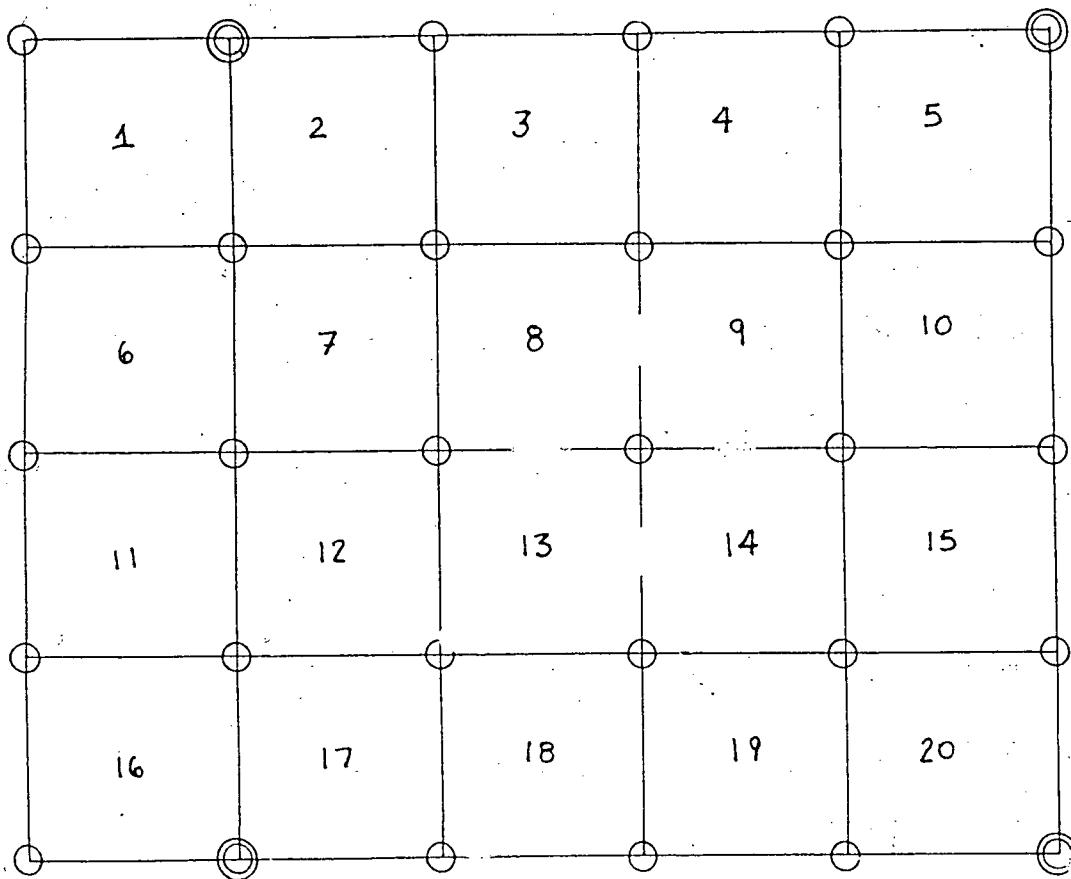


Figure 4.18: The boxes used for the inverse model of the Ocean Storms area. For cruise one, all the boxes are defined.

To obtain an equation for the conservation of salt,  $S$ , one starts by combining the advection diffusion equation and the conservation of mass equation

$$(uS)_x + (vS)_y + (wS)_z = \vec{\nabla}_H(k_h \vec{\nabla}_H S) + \frac{\partial}{\partial z}(k_z \frac{\partial S}{\partial z}) \quad (4.22)$$

An equation is obtained by integrating this equation over an enclosed box

$$\begin{aligned} \Delta y \Delta z \bar{u} \bar{S} \Big|_E^W + \Delta x \Delta z \bar{v} \bar{S} \Big|_S^N + \Delta x \Delta y \bar{w} \bar{S} \Big|_B^T = \\ \Delta x \Delta y k_z \frac{\partial S}{\partial z} \Big|_B^T + \Delta y \Delta z k_h \frac{\partial S}{\partial x} \Big|_E^W + \Delta x \Delta z k_h \frac{\partial S}{\partial y} \Big|_S^N \end{aligned} \quad (4.23)$$

The overbar again denotes the average value on each face of the box. From this, an equation can be generated by rewriting the velocity term in its two parts, the reference velocity and the relative velocity

$$\begin{aligned} \Delta y \Delta z u_o \bar{S} \Big|_E^W + \Delta x \Delta z v_o \bar{S} \Big|_S^N + \Delta x \Delta y w_o \bar{S} \Big|_B^T - \\ \Delta x \Delta y k_z \frac{\partial S}{\partial z} \Big|_B^T - \Delta y \Delta z k_h \frac{\partial S}{\partial x} \Big|_E^W - \Delta x \Delta z k_h \frac{\partial S}{\partial y} \Big|_S^N = \\ - \Delta y \Delta z \bar{u}_r \bar{S} \Big|_E^W - \Delta x \Delta z \bar{v}_r \bar{S} \Big|_S^N - \Delta x \Delta y \bar{w}_r \bar{S} \Big|_B^T \end{aligned} \quad (4.24)$$

This equation relates the unknown transport of  $S$  due to the reference velocities and mixing terms to the known transport of  $S$  due to the relative velocities. An identical equation can be written for the temperature  $T$ .

By applying this idea to many boxes, a set of equations is obtained. This set of equations can be written as the matrix equation  $\mathbf{A}\vec{x} = \vec{b}$ . The vector  $\vec{x}$  represents the unknown variables  $u_o, v_o, w_o, k_z, k_h$ ; the matrix  $\mathbf{A}$  represents the average properties on the faces of the boxes; and the vector  $\vec{b}$  represents the mass, heat, and salt transport due to the relative velocities. This averaging of the variables on each face of the box results in a reduction in the resolution of the model but also reduces the susceptibility of the method to errors in the data.

### 4.2.2 Ocean Storms Grid

In order to use the Box model, one has to select a set of layers over which one can apply the conservation constraints. Traditionally in the large regional studies [1,18,7], the vertical layering was based on isopycnal surfaces. The use of this layering stems from early work of water mass analysis that states that the flow should occur along isopycnal surfaces [3]. In a small regional study such as the Ocean Storms experiment, the slope of the isopycnal surfaces is nearly horizontal over the study area. Therefore it is considered appropriate and convenient to divide the ocean vertically according to pressure surfaces, instead of isopycnal surfaces. These surfaces of constant pressure are almost identical to surfaces of constant depth ( $\pm 0.1m$ ). The layering of the Ocean Storms area is shown in Table 4.1.

By dividing the ocean according to these 17 different levels, one reduces the ocean to 16 layers. The reduced thickness of the layers in the upper ocean is necessary to properly define the features such as the mixed layer, seasonal thermocline, and halocline. The boxes defined in the Ocean Storms grid are shown in Figure 4.18. For every layer considered in the model there are 20 boxes; with a maximum of 16 layers this allows for a maximum of 320 boxes. With three constraints to be applied to each box, the maximum number of equations available to constrain the problem is 960. The maximum number of unknowns to the problem is determined by considering that for any layer one must determine the reference velocity on every face of the box. This requires that 24  $u_o$ 's, 25  $v_o$ 's, and 20  $w_o$ 's be determined. In addition, since the mixing terms are considered to be only functions of depth,  $k_h$  was determined for each layer (16 maximum) and  $k_z$  was determined at each level except at the surface (16 maximum). The total maximum number of unknowns to the problem is 101.

Level	Pressure (dbar)	Depth (m)
1	0.0	0.00
2	40.0	39.8
3	60.0	59.7
4	100.0	99.5
5	150.0	149.1
6	200.0	198.8
7	250.0	248.4
8	300.0	298.0
9	400.0	397.1
10	500.0	496.2
11	600.0	595.2
12	700.0	694.2
13	800.0	793.1
14	900.0	892.0
15	1000.0	990.8
16	1200.0	1188.3
17	1500.0	1484.2

Table 4.1: The levels used to vertically define the boxes used in the model.

Although I have listed the entire layering of the ocean, due to the underlying assumptions made in discussing the physical problem (ie. steady state and neglect of source and sink terms for heat and salinity), the number of layers actually considered in the model is less. The layers to be included in the model are determined by analyzing the temperature and salinity depth profiles obtained in the Ocean Storms area during the two cruises. These profiles show that depths shallower than 150 m clearly violate the assumptions. This reduces the number of unknowns to 94.

One other parameter that must be specified for the inversion is the depth of the reference level used in determining the relative geostrophic flow. Most of the previous work in this area uses the 1000 dbar level as the choice of reference level [17]. This level is also used for the inverse model.

### 4.3 Including A Priori Information

Before proceeding to describe how to obtain a solution to the inverse problem, there is still additional information that can be included to obtain a more realistic solution. A priori information is included in the model through the use of weighting matrices and inequality constraints.

By proper weighting of the system of equations, one can include additional information in the inversion. This method of weighting the equations has been used in previous work on this problem to force the solution to be more physically real [1,19]. The weighted problem can be written as

$$\underbrace{\mathbf{QAW}}_{\mathbf{B}} \underbrace{\mathbf{W}^{-1}\vec{x}}_{\vec{m}} = \underbrace{\mathbf{Q}\vec{b} + \mathbf{Q}\delta\vec{b}}_{\vec{e} + \delta\vec{e}} \quad (4.25)$$

$$\mathbf{B} \quad \vec{m} = \quad \vec{e} + \delta\vec{e} \quad (4.26)$$

The matrices  $\mathbf{Q}$  and  $\mathbf{W}$  are referred to as the data weighting matrix and parameter

weighting matrix respectively. These weighting matrices represent covariance matrices for the errors in the forcing terms,  $\delta\vec{b}$ , and for the unknowns,  $\vec{x}$ . Due to the lack of knowledge about the correlation between unknowns, and the affect of errors in the data on matrix  $\mathbf{A}$ , diagonal matrices are used [19,1].

The errors present in the forcing terms for the inverse problem are in part due to measurement errors, but are mostly due to unresolved small scale processes like internal gravity waves and baroclinic eddies [7]. With no definite information about the magnitude of these errors,  $\delta\vec{b}$ , and with no clear understanding of how errors in the data affect matrix  $\mathbf{A}$ , the rows of  $\mathbf{A}$  are normalized by their length to force all equations to be treated equally by the inversion [19]. An additional factor,  $\vec{C}$ , is added to allow one to easily change the importance of the different constraints. The data weighting matrix is defined as follows

$$Q_{ii} = C_i / \left( \sum_{j=1}^M a_{ij}^2 \right)^{-1/2} \quad (4.27)$$

The parameter weighting matrix  $\mathbf{W}$  is used to include information on the expected magnitude of the different model parameters [19]. This is done by defining a diagonal weighting matrix to be

$$W_{ii} = |x_j|^{1/2} \left( \sum_{i=1}^N a_{ij}^2 \right)^{-1/4} \quad (4.28)$$

In the two equations defining the weighting matrices,  $a_{ij}$  are the elements of the matrix  $\mathbf{A}$ ,  $N$  is the number of equations,  $M$  is the number of unknowns, and  $[x_j]$  is the expected magnitude of the  $j^{\text{th}}$  unknown. The expected magnitudes of the unknowns are set to:

- 1)  $|u_o|$  and  $|v_o| = 10^{-2}m/s$
- 2)  $|w_o| = 10^{-8}m/s$
- 3)  $|k_z| = 10^{-4}m^2/s$
- 4)  $|k_h| = 10^2m^2/s$

Without including any information on the magnitude of the different unknowns, the model will produce a physically unrealistic solution [1]. Thus it is desirable to correct

this problem to ensure that the magnitude of the model parameters are consistent with the physical situation. The use of the parameter weighting matrix forces all the model parameters to be of the same order of magnitude and thus not bias the solution to determine the unknowns which have a large magnitude [20].

Inequality constraints are included in the model to force the mixing coefficients to be positive. This is required because physically meaningful solutions only exist for solutions which have positive mixing coefficients [6]. This extension to the inverse problem is called the least squares inversion with inequality constraints (LSI) [21]. In mathematical notation, the solution to the LSI problem is obtained by minimizing

$$\psi = \|\mathbf{B}\vec{m} - \vec{e}\| \quad (4.29)$$

subject to the inequality constraints

$$\mathbf{H}\vec{m} \geq \mathbf{0} \quad (4.30)$$

The matrix  $\mathbf{H}$  is defined to only allow positive mixing coefficients.

#### 4.4 Solving the Inverse Problem

As formulated, the resulting inverse problem  $\mathbf{B}\vec{m} = \vec{e}$  is overdetermined. In reality, the problem is formally underdetermined and an infinite number of degrees of freedom exists in the solution [7]. It is only through simplifying the physics of the problem (ie. assuming the flow is steady-state and geostrophic) and parametrizing the continuous velocity fields that the problem is made to be overdetermined. Through this simplification of the problem, one hopes to make more efficient use of the data available. But the results of this inverse problem are only of interest if this simplified model captures the essence of the real situation. This is an important point to consider in inverse modelling because considerable uncertainty in the results may stem primarily from this simplification of the

model. This point will be discussed in later chapters when discussing and evaluating the results of the model.

The solution to the inverse problem is obtained using the LSI algorithm developed by Lawson and Hanson [21]. Essential to this method is the singular value decomposition (SVD) of the matrix  $\mathbf{B}$ . To gain additional insight into the ability of the model to predict a solution, the problem is analyzed without the inequality constraints. To include the inequality constraints in such an analysis would be too difficult.

The advantage of using SVD to analyze the inverse problem is that it allows one to identify less certain information in matrix  $\mathbf{B}$ . This factorization provides an excellent way of representing and ranking the information contained in the matrix  $\mathbf{B}$  [20]. This enables one to minimize the effect of the less certain information on the solution [20,22].

Consider solving the inverse problem with  $N$  equations and  $M$  unknowns

$$\underbrace{\mathbf{B}} \quad \vec{m} = \vec{e} \quad (4.31)$$

$$N \times M \quad M \times 1 \quad N \times 1$$

$$(4.32)$$

If there are  $k$  independent equations among the  $N$  simultaneous equations, then the matrix  $\mathbf{B}$  has rank  $k$  and can be factored using SVD as follows [22]

$$\mathbf{B} = \mathbf{U} \quad \mathbf{\Lambda} \quad \mathbf{V}^T$$

$$N \times M \quad N \times k \quad k \times k \quad k \times M$$

$$\mathbf{U} = \begin{vmatrix} | & | & | & \cdots & | \\ u_1 & u_2 & u_3 & \cdots & u_k \\ | & | & | & & | \end{vmatrix}$$

$$\mathbf{\Lambda} = \begin{vmatrix} \lambda_1 & 0 & 0 & \dots \\ 0 & \lambda_2 & 0 & \dots \\ \vdots & 0 & \ddots & 0 \\ 0 & 0 & 0 & \lambda_k \end{vmatrix}$$

$$\mathbf{V} = \begin{vmatrix} | & | & | & & | \\ v_1 & v_2 & v_3 & \dots & v_k \\ | & | & | & & | \end{vmatrix}$$

The matrix  $\mathbf{U}$  contains  $k$  eigenvectors,  $u_i$ , associated with the span of the column vectors of matrix  $\mathbf{B}$ . The matrix  $\mathbf{V}$  contains  $k$  eigenvectors,  $v_i$ , associated with the span of the row vectors of matrix  $\mathbf{B}$  [22]. The matrix  $\mathbf{\Lambda}$  is a diagonal matrix of  $k$  singular values,  $\lambda_i$ , arranged in descending order.

Once the matrix has been decomposed using SVD, the generalized inverse of the matrix  $\mathbf{B}$  is [22]

$$\mathbf{B}^{-1} = \mathbf{V}\mathbf{\Lambda}^{-1}\mathbf{U}^T \quad (4.33)$$

and the solution to the inverse problem is [22]

$$\vec{m} = \mathbf{V}\mathbf{\Lambda}^{-1}\mathbf{U}^T\vec{e} \quad (4.34)$$

or, in component form,

$$m_i = \sum_j \frac{v_{ij}\vec{u}_j e_j}{\lambda_j} \quad (4.35)$$

This equation shows that the calculated solution is very sensitive to small singular values. The relative importance of the small singular values in the calculated solution means that these values will tend to greatly amplify any errors present in the data [22].

In order to use the generalized inverse (4.33), it is essential that one identify the number of non-zero singular values,  $p$  [22]. One must determine if the small singular

values are really non-zero or caused by errors in the matrix equations and calculations of the SVD. This problem is dealt with by either truncating singular values below a specified cutoff or by adding a small constant to all singular values. Both methods were investigated and there were only small differences in the results. In the results to follow, a sharp cutoff will be used.

To determine how these small singular values should be treated, the following will be used: 1) a plot of the magnitude of the singular value versus the index number, 2) a plot of the error reduction versus the number of singular values used, 3) a trade-off curve relating the size of the model variance to the resolution of the model, and 4) the examination of the solutions obtained with different cutoffs. This analysis will be performed on the data from cruise one. Weighting matrices will be applied to the system of equations generated and all equations will be treated equally (ie.  $\vec{C} = 1$ ). The results of this analysis will be applied to solving the LSI problem.

The range in magnitude of the singular values of matrix **B** is displayed in Figure 4.19. This plot shows a gradual decrease in magnitude of the singular value with index number,  $p$ . Only the singular value with index number,  $p \geq 82$ , are significantly smaller than the previous values. These singular value are considered to be zero and will not be used in the solution.

The plot of the normalized residual error versus the number of singular values used in the solution is displayed in Figure 4.20. This plot indicates that at least the first 25 singular values of matrix **B** should be retained in order to adequately reduce the error in the solution.

To really assess how to handle the small singular values, a trade-off curve was constructed that relates the resolution of the model to the variance in the solution. To

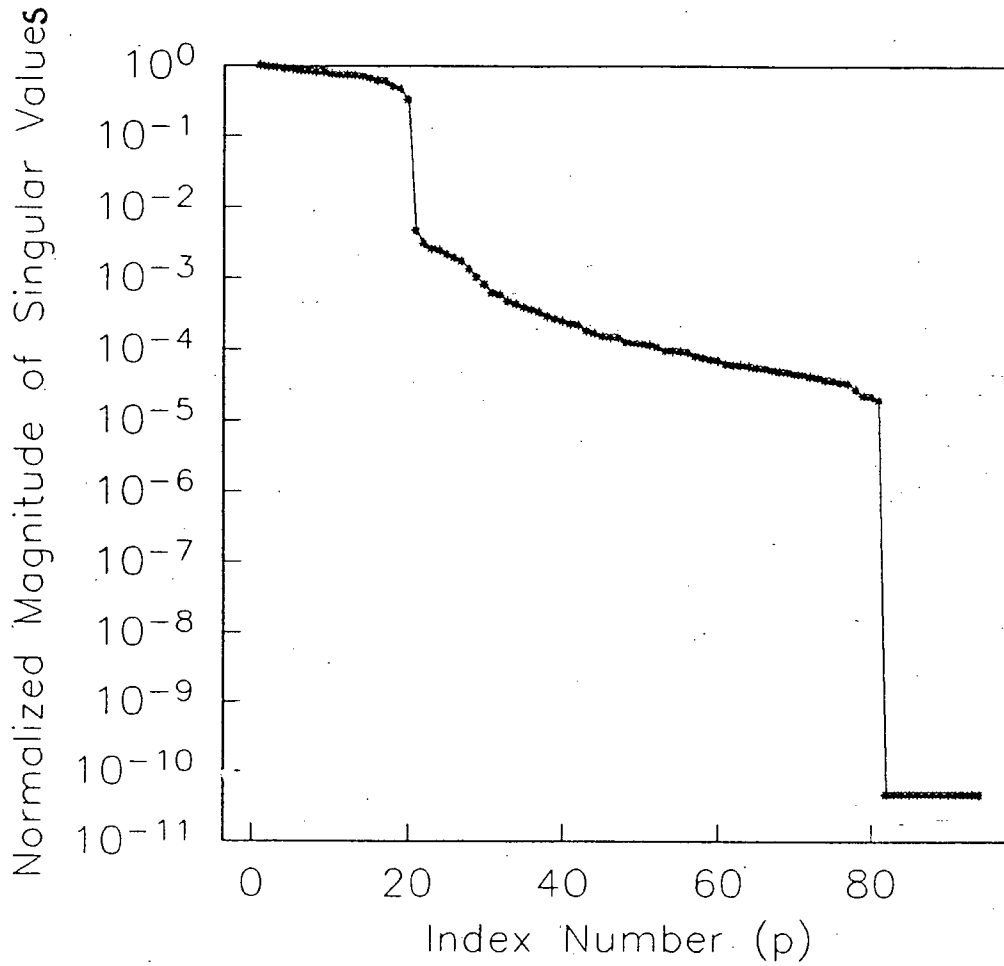


Figure 4.19: A plot of the normalized magnitude of the singular values versus index number p.

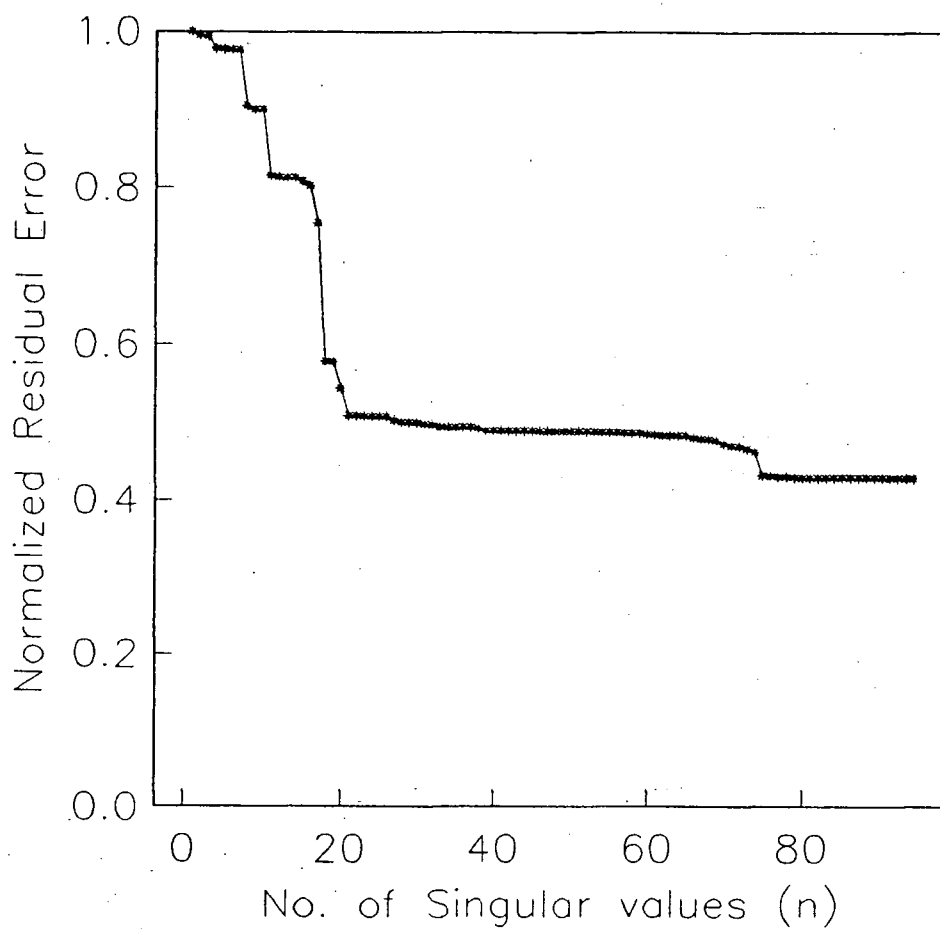


Figure 4.20: The reduction in error versus the number of singular values of matrix  $\mathbf{B}$  that are used in determining the solution. The number of singular values used ( $n$ ), indicates that the first  $n$  singular values of matrix  $\mathbf{B}$  are used.

calculate the variance in the solution, the following definition was used [22]

$$\text{size of solution variance} = \|\sigma_o(\mathbf{V}\mathbf{\Lambda}^{-2}\mathbf{V}^t)\| \quad (4.36)$$

The  $\sigma_o$  is assumed to be constant. The resolution of the solution is determined using the following definition [22]

$$\text{spread of solution resolution} = \|\mathbf{V}\mathbf{V}^t - \mathbf{I}\| \quad (4.37)$$

The trade-off curve was constructed by changing the prescribed cutoff and calculating the model resolution and variance. The value of the cutoff used implied that singular values with normalized magnitude less than this cutoff were omitted in this analysis. The trade-off curve obtained, Figure 4.21, shows that by demanding a model that highly resolves the solution, the spread of the solution resolution will be small, but the variance of that solution will be large. This trade-off curve allows one to assess and determine the optimum cutoff based on the compromise between a well-resolved solution and a model with a satisfactory variance. Based on the trade-off curve,  $10^{-4}$  is selected as the best choice of the cutoff. It is important to realize that the trade-off curve is strictly based on matrix  $\mathbf{B}$ , neither the solution to the inverse problem nor the forcing terms enter into this analysis which only assesses the ability of the model to determine a solution.

A cutoff of  $10^{-4}$  produces a satisfactory solution to the LSI problem. If this cutoff is decreased, the magnitude of the solution becomes unreasonably large. This cutoff represents the minimum acceptable cutoff for determining the non-zero singular values of matrix  $\mathbf{B}$ . It will be shown in the next chapter that this cutoff level will not produce a solution that is very overly sensitive to the expected errors in the data. By using this cutoff the rank of the matrix  $\mathbf{B}$  is reduced to 52. As the problem is mixed-determined the condition of minimizing the energy of the solution will be implicitly used to further constrain the solution.

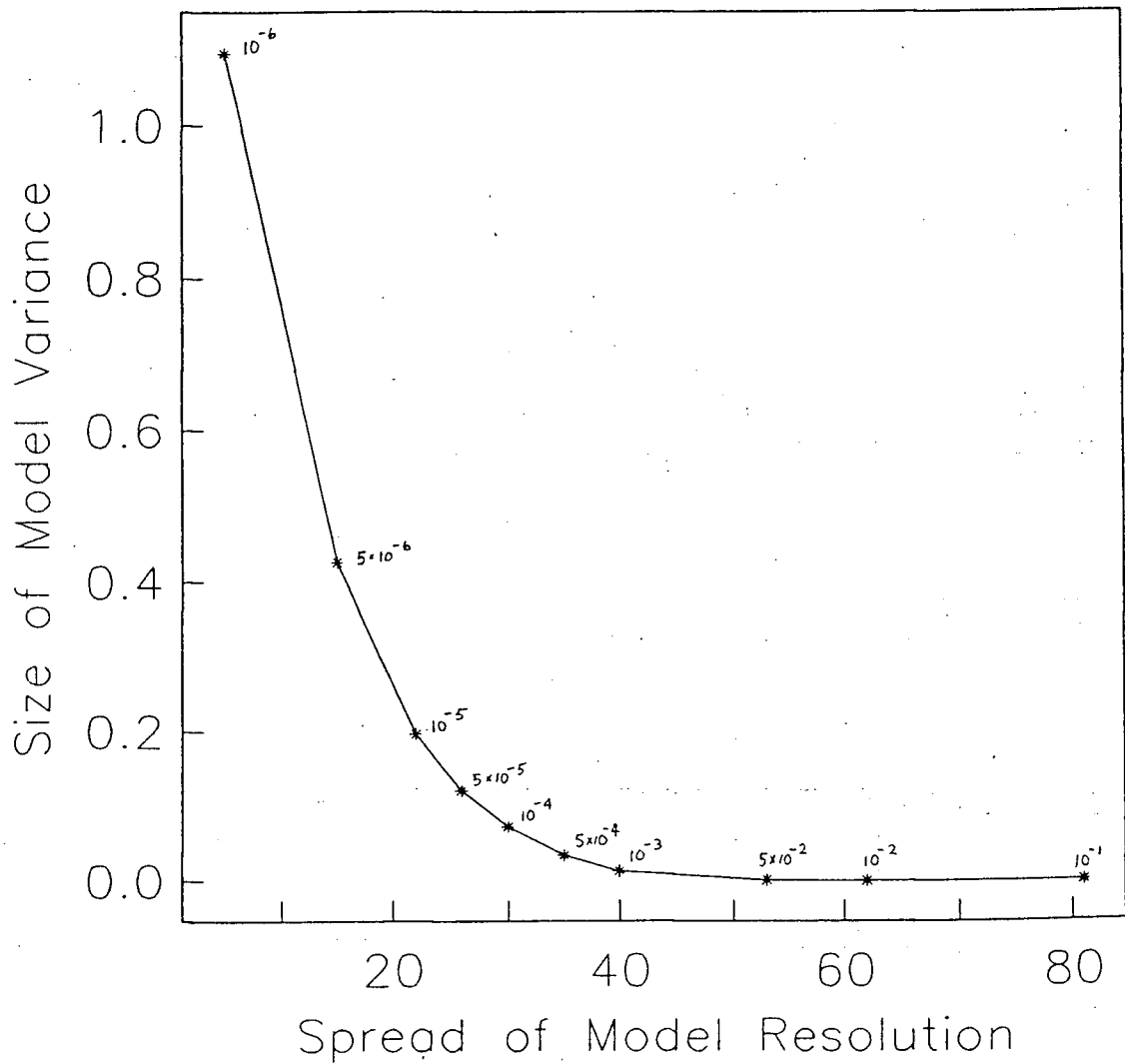


Figure 4.21: The trade-off curve for the inverse model. This curve relates the resolution of the model to the size of the variance of the unknowns. The numbers over the points on this curve indicate the cutoff for the singular values.

## Chapter 5

### Evaluating the Model and Solution

In this chapter I evaluate the model and solution in an attempt to better understand the model and estimate the uncertainty in the solution. I first investigate the importance of the three conservation conditions – temperature, salt and mass – in determining the solution and assess whether modifying the weighting of these conditions is necessary. Second, I examine the layering used in the model. Third, I vary the reference level to see how this affects the solution. Fourth, I evaluate how important the different unknowns are in the solution and estimate how well resolved they are. Fifth, I investigate how sensitive the solution is to errors in the data. The initial solutions are based on a 12-layer model with the reference level at 1000 dbar.

To compare the solutions obtained in the following sections, correlations and regression coefficients are used. To calculate these coefficients, all the unknowns parameters are used (total of 94), and they are weighted so that they are of the same order of magnitude. The error reduction in the different solutions are also used in comparing the different solutions. The normalized residual errors in the three conservation conditions ( $l = \text{either T, S, or M}$ ), are determined as follows

$$E_l = \frac{\sum_{i=1}^N (B_i \vec{m} - e_i)^2}{\sum_{i=1}^{3N} (e_i)^2} \quad (5.38)$$

In this equation,  $N$  refers to the number of constraint equations for that condition,  $B_i$  is the set of rows of matrix  $\mathbf{B}$  describing these equations, and  $e_i$  is the corresponding forcing term. The total of these three errors gives the total reduction in error from the

initial condition where all unknown parameters are zero. Throughout this chapter the null solution will be used to denote the solution where all the unknown parameters are zero.

## 5.1 The Importance of Temperature, Salt and Mass Conditions on the Solution

The solution obtained to the inverse problem  $\mathbf{B} \vec{m} = \vec{e}$  is dependent on the forcing terms  $\vec{e}$ . If this vector is identically zero then the solution vector  $\vec{m}$  will also be zero. It is the non-zero forcing terms that force the solution to the problem to be non-zero. These forcing terms are due to three effects: 1) the relative vertical velocity which affects the conservation of mass in each of the boxes, 2) the transport of heat due to the relative vertical and horizontal velocities, and 3) the transport of salt due to the relative vertical and horizontal velocities.

The following analysis will illustrate the incompatibilities between the different conservation conditions (ie. mass, salt, and heat). It will also show which conditions provide the most constraint on the solution. To assess the importance of these three conditions, they are alternately up-weighted by a factor of five. The solution obtained is then compared to the reference solution which weighted the three conditions equally (S=1, M=1, T=1).

The correlation and regression coefficients between the up-weighted solutions and reference solution are shown in Table 5.2. The biggest value of the correlation coefficient exists for the up-weighted salt condition. This implies that the salt condition plays the dominant role in forcing the reference solution. The much smaller values of the correlation coefficient for the up-weighted temperature and mass conditions indicates that this information is of considerably less importance in forcing the reference solution.

Temp. Weighting	Salt Weighting	Mass Weighting	Correlation coefficient	Regression coefficient
5	1	1	0.357	1.7976
1	5	1	0.789	1.8169
1	1	5	0.165	0.0075

Table 5.2: Correlation and regression coefficients between up-weighted solutions and the reference solution which weighted the three conditions equally (T=1, S=1, M=1).

The value of the regression coefficient for the up-weighted salt and temperature conditions ( $\approx 1.8$ ) indicates that the magnitude of these solutions are almost twice as large as the magnitude of the reference solution. However, the regression coefficient for the up-weighted mass condition is considerably smaller than one. This indicates that the magnitude of the solution obtained from this weighting is considerably smaller than the magnitude of the reference solution. This points out the importance of the mass conditions in the reference solution. The mass condition is not important in forcing the solution, as exhibited by the small correlation coefficients. The role of the mass condition is to damp the magnitude of the solution in order to force the solution to conserve mass.

The normalized residual error for up-weighting the three conditions reveals additional insight into the problem. These errors (Table 5.3), show that the errors in the three conditions differ greatly. The error in temperature in the null solution is extremely small. This small error in the temperature condition is attributed to the fact that the geostrophic flow is almost parallel to the isotherms. This close connection between the dynamic height and temperature field demonstrates the importance of the temperature information in determining the relative geostrophic velocities. Most of the relevant information in the temperature field is used to determine the relative velocities. This prevents this condition

Solution	Temperature error	Salinity error	Mass error	Total error
Null	0.005	0.376	0.619	1.000
Reference	0.012	0.190	0.297	0.499
Temp.	0.001	0.211	0.297	0.509
Salt	0.299	0.142	0.290	0.731
Mass	0.006	0.210	0.295	0.511

Table 5.3: The normalized residual errors in the three conditions for the null solution, the reference solution, and the solution obtained by alternating the up-weighting of the three conditions. The solution for temperature, salt or mass is the solution obtained when this condition is up-weighted by a factor of 5.

from being more effective in the reference solution. The errors in the salt and mass condition for the null solution are two orders of magnitude greater than the error in the temperature condition. The errors in both these conditions are significantly reduced in the reference solution.

By demanding that the salinity condition be highly satisfied, the error in the temperature condition increases drastically. This demonstrates the incompatibility between these two conditions. The situation for the up-weighted temperature condition further clarifies that the temperature information carries similar information as the salt field but it is the salt field that yields additional information to constrain the flow. This incompatibility between these two constraints may arise from the assumptions made in developing the model and the inability of the temperature condition to determine the absolute geostrophic velocity.

It is surprising that the error in the mass condition is so large. It was felt that this condition should be less significant because its forcing ability is probably based on the weakest assumption in the model, the linear  $\beta$ -plane vorticity equation. Also, the solution should approximately conserve mass because the forcing terms for this condition,

the relative vertical velocities, are small. A closer examination of the model does reveal the cause of the large error in this condition. The large error in this condition is an artifact of the row weighting of the matrix equations. The forcing terms for this condition are magnified because the vertical reference velocity is not present in the conservation of mass equations. This is valid because this term does not affect the mass in the boxes. As a result though, when the row weighting is applied to these equations, the calculated row norm is considerably smaller than the other two conditions. This is shown through the use of a simplified conservation of mass equation

$$\frac{\partial}{\partial x}(u_o) dy dz + \frac{\partial}{\partial y}(v_o) dx dz + \frac{\partial}{\partial z}(w_o) dx dy = \frac{\partial}{\partial z}(w_r) dx dy$$

$$dx = 60000m$$

$$dy = 60000m$$

$$dz = 100m$$

Without the term for the relative vertical velocity, the norm of this equation is approximately  $\sqrt{2} dz$ , but if the relative vertical velocity is included the norm increases to approximately  $dx dy/dz$ . Since  $dx$  and  $dy$  are considerably greater than  $dz$ , the norm of the equation is increased greatly by the addition of the third term. By having a much larger norm, the forcing term is reduced because the equation is weighted by the inverse of the norm of the equations. Due to this formulation and weighting of the problem, the mass condition is given additional importance in the solution.

To assess the importance of the weighting of the mass condition on the solution, various weightings of the mass condition are tried. The solutions for these various weights are considered to determine if the weighting of the mass condition should be altered. The correlation and regression coefficients for the various weights are displayed in Table 5.4. These coefficients reveal that for weights smaller than 0.5, the solutions do not change significantly. By down-weighting the mass condition to 0.5 or less, the magnitude of the

Correlation coefficients						
	Mass Weights					
	1.0	0.5	0.25	0.1	0.05	0.01
1.0	1.000	0.664	0.653	0.613	0.612	0.611
0.5		1.000	0.809	0.661	0.605	0.579
0.25			1.000	0.964	0.934	0.918
0.10				1.000	0.995	0.990
0.05					1.000	0.999
0.01						1.000

Regression Coefficients						
	Mass Weights					
	1.0	0.5	0.25	0.1	0.05	0.01
1.0	1.000	2.92	3.07	3.49	3.51	3.52
0.5		1.000	1.695	1.457	1.309	1.242
0.25			1.000	1.047	1.012	0.992
0.10				1.000	0.999	0.994
0.05					1.000	1.000
0.01						1.000

Table 5.4: Correlation and regression coefficients between solutions with various weights for the conservation of mass condition. The weighting of the temperature and salt conditions are held fixed at one.

	Weight of conservation of mass constraint						
	1.0	0.5	0.25	0.1	0.05	0.01	Null
Temp	0.012	0.016	0.017	0.020	0.020	0.020	0.005
Sal.	0.190	0.174	0.173	0.165	0.165	0.165	0.376
Mass	0.297	0.306	0.314	0.329	0.330	0.331	0.619
Total	0.499	0.496	0.504	0.514	0.515	0.516	1.000

Table 5.5: The normalized residual errors in the conservation of temperature, salt, and mass conditions for various weights for the conservation of mass condition. The Null column refers to errors in these three conditions if the solution is identically zero.

resulting solutions increases by threefold over the reference solution. This emphasizes the importance of the mass condition in damping the reference solution.

The effect of changing the weight of the mass condition on the residual errors is shown in Table 5.5. All errors have been referenced back to the weighting of the reference solution ( $T=1$ ,  $S=1$ ,  $M=1$ ) for easy comparison. As expected, reducing the weight on the mass condition increases the error in this condition slightly. Accompanying this increase in error is a slight reduction in the salt error and a slight increase in the temperature error. The down-weighting of the mass condition appears to allow the salinity information to be even more significant in forcing the solution.

The result of varying the conservation of mass equation reveals that down-weighting the mass condition produces a dramatic change in the solution without significantly affecting the total reduction in errors. The magnitude of the solution increases abruptly as the mass condition is down-weighted. From this analysis it seems best not to down-weight the mass condition. The mass condition includes very relevant information to the problem and should clearly be included in the model. Furthermore, it can be argued that a physically real solution only exists for the situation where the mass in the interior of the ocean is exactly conserved. This extreme could be followed to further constrain the solution [23] but it is felt that a more moderate approach should be taken because

errors in this condition may exist arising from assumptions in the model and errors in the relative velocities.

It is clear that by subjectively changing the weighting of these three conditions, the solution to the problem will change significantly. In light of the present situation, it was not considered appropriate to bias one of the conditions more heavily than the others. The unbiased weighting of the equations will be used in obtaining a solution to the model. The layering of the ocean will now be investigated using this equal weighting of the three conservation conditions.

## **5.2 The Effect of the Layering of the Ocean on the Solution**

In this section I will first look at how the solution is affected by the number of layers used in the model. Then I will consider how changing the layering of the ocean in the model will affect the solution.

By changing the number of layers included in the model, one can determine which layers are important in forcing the model. In Table 5.6, the solutions obtained using various numbers of layers are compared to the reference solution, a 12-layer model. To calculate the correlation and regression coefficients displayed in this table only the reference velocities are used, this gives a sample size of 69 parameters. The minimum depth in the table indicates that data obtained from depths shallower than this level will be neglected in the model.

It is evident from this table that the data from the 150 - 200 dbar layer does not greatly affect the reference solution. By including data shallower than 150 dbar (149.1 m), the solution does change significantly. The magnitude of the solution increases rapidly as the surface is approached. From the large difference in solutions between the 12- and 13-layer models, 150 m is assumed to represent the upper boundary on the model.

Min. Depth (dbar)	Number Layers	Correlation coefficient R	Regression coefficient slope ( X)
400.0	8	0.723	0.534
300.0	9	0.804	0.610
250.0	10	0.875	0.690
200.0	11	0.991	0.970
150.0	12	1.000	1.000
100.0	13	0.900	1.107
60.0	14	0.894	1.090
40.0	15	0.873	1.082
0.0	16	0.443	1.300

Table 5.6: The correlation and regression coefficients between the reference solution, a 12-layer model with solutions obtained from models using different numbers of layers.

This table clearly displays the importance of the data between 200 and 500 dbar in forcing the solution. Basing the solutions largely on data from this range of depth is considered valid because for depths greater than 500 dbar the horizontal gradients of the salt and temperature field are small and they approach the accuracy of the measurements. The assumption of the steady-state condition for temperature may be questioned in the upper layers of this model but with the salt condition dominating the forcing of the solution, this assumption appears to be valid at least for the time interval between the two cruises.

To investigate the problem of how to divide the ocean into layers, results were obtained using a simplified layering of the ocean. The solutions obtained for models with different layerings of the ocean are shown in Table 5.7. This illustrates that the solution is quite independent of how the ocean is divided into layers. A 12-layer model will be retained in order to increase the resolution of the vertical mixing coefficients.

Number of Layers	Correlation coefficient	Regression coefficient
6	0.9802	0.9729
5	0.9627	0.9571

Table 5.7: The correlation and regression coefficients between the reference solution and solutions obtained by doubling the thickness of the layers considered in the model. For the 6-layer model the ocean is divided according to the following pressure surfaces, 150, 250, 400, 600, 800, 1000, 1500 dbar. The 5-layer model divides the ocean according to the following surfaces, 150, 250, 500, 800, 1000, 1500 dbar. Only the reference vertical and horizontal velocities are used in determining the regression and correlation coefficients.

### 5.3 The Sensitivity of the Solution to the Choice of Reference Level

All the previous solutions were obtained using the reference level of 1000 dbar. To observe how sensitive the model is to the choice of reference level, solutions can be obtained using different reference levels. These solutions are compared to the reference solution that used 1000 dbar as the reference level. The velocities from these different solutions are compared to the reference solution at the 1000 dbar level. The calculated mixing coefficients are also included in calculating the correlation and regression coefficients (Table 5.8)

The high correlation coefficients indicates that the calculated flow patterns are nearly depth independent. However, the regression coefficient indicates that the magnitude of the solutions are dependent on the choice of the reference level. Most of the variance the solutions occurs in the vertical reference velocities ( $\pm 20\%$ ), and the horizontal mixing coefficients ( $\pm 40\%$ ). The horizontal velocities and the vertical mixing coefficients are nearly independent of depth being determined to  $\pm 15\%$  and  $\pm 5\%$  respectively. This indicates that these unknowns are well resolved by the model. This can readily be shown from the matrix equation. The changing of the reference level of the model is equivalent to adding an additional term to the forcing terms. Due to the formulation of the problem,

Reference Level	Correlation coefficient	Regression coefficient
500	0.957	0.810
600	0.977	0.857
700	0.970	0.947
800	0.996	0.942
900	0.999	0.974
1000	1.000	1.000
1200	0.998	1.043
1500	0.989	1.060

Table 5.8: The correlation and regression coefficient between solutions using different reference levels and the reference solution that used 1000 dbar. The correlation and regression coefficients were calculated using the velocities from 1000 dbar and all of the mixing coefficients.

this additional forcing term is equal to  $\vec{b}'$ , where  $\vec{b}' = \mathbf{B}\vec{x}_c$ . The vector  $\vec{x}_c$  is the velocity difference between the 1000 dbar level and the new reference level. Thus the new problem is

$$\mathbf{B}\vec{x} = \vec{b} + \vec{b}' \quad (5.39)$$

$$\vec{x} = \mathbf{B}^{-1}(\vec{b} + \vec{b}') \quad (5.40)$$

$$\vec{x} = \mathbf{B}^{-1}(\vec{b}) + \mathbf{V}\mathbf{V}^t\vec{x}_c \quad (5.41)$$

Therefore if the matrix  $\mathbf{V}\mathbf{V}^t$ , the resolution matrix, is equal to the identity matrix, the solution will be exactly independent of the choice of the reference level. In the model used here the resolution matrix is not exactly equivalent to the identity matrix. This allows the solution to change slightly depending on the choice of reference level. The standard deviation of the unknown parameters about the solution using the 1000 dbar reference level is used to estimate the errors in the solution. The estimated errors in the

unknown parameters are

$$1) u_o = \pm 0.12 \text{ cm/s}$$

$$2) v_o = \pm 0.10 \text{ cm/s}$$

$$3) w_o = \pm 0.20 \text{ } \mu\text{m/s}$$

$$4) k_h = \pm 100 \text{ m}^2/\text{s}$$

$$5) k_z = \pm 0.3 \text{ cm}^2/\text{s}$$

It is observed that the errors in the conservation of salt, heat and mass is minimized by assuming a level of no motion at 700 dbar. This suggests that the best choice for the level of no motion exists at about this pressure level. However the error in the salt condition is still significantly reduced in the inverse solution from that of assuming a level of no motion at 700 dbar. Furthermore, the result of the inverse solutions do not indicate that a level of no motion should exist at 700 dbar since there is still a well-defined structure to the flow field. The model will continue to use the 1000 dbar level as the reference level. The high correlation coefficient indicates that the flow field will not be significantly affected by this choice.

#### 5.4 The Importance of the Different Unknown Parameters on the Solution

The result of varying the reference level confirms that not all the unknowns are equally well resolved. The resolution matrix ( $VV^t$ ), described in the previous section, provides information on how well the model can resolve the different unknown parameters. Each  $i^{th}$  row of the matrix gives the resolution of the  $i^{th}$  unknown parameter in terms of an average of all the unknown parameters. If the diagonal element of the  $i^{th}$  row of the matrix is 1, then the resolution of the  $i^{th}$  unknown parameter is perfectly resolved, ie. 100% resolution. The vertical mixing coefficients are well determined by the model, the resolution of these parameters ranges from 81% to 99%. The shallower mixing terms are

better resolved than the deeper mixing terms. The horizontal velocities are also quite well resolved. The resolution of these parameters ranges from about 75% to 80%. The  $v$ -component of the horizontal velocities is slightly better resolved than the  $u$ -component. The resolution of the vertical reference velocity and horizontal mixing coefficients is considerably smaller. The vertical reference velocity is resolved to about 25% and the horizontal mixing coefficients are resolved to about 10%.

To explore the importance of the unknown parameters on the solution, different parameters are neglected in the model to observe how the solution changes. The correlation and regression coefficients for the horizontal reference velocities between the reduced model and the reference model are shown in Table 5.9.

It is evident from this table that the vertical mixing coefficients are important factors in determining the reference solution. However, the horizontal mixing terms do not significantly alter the solution. This result, coupled with the poor resolving capability of the model for this variable, led to the decision to neglect the horizontal mixing term from the model. By neglecting the vertical reference velocity in the model, a significant change in the solution occurs. Although the vertical reference velocities are not well determined, their importance in the solution is recognized and thus they are retained in the model. It was observed that by neglecting the vertical reference velocities, the value of vertical mixing coefficients decreases.

### 5.5 Sensitivity of the Solution to Errors in the Data

To evaluate how sensitive the model is to errors in the data, random gaussian errors and coherent errors were added to the original temperature and salinity data before obtaining a solution. By adding these errors to the original data, both the effect of these errors on matrix  $\mathbf{B}$  and on the forcing terms  $\vec{e}$  can be observed.

Parameter Not Included	Correlation coefficient	Regression coefficient
$k_z$	0.368	0.164
$k_h$	0.993	0.990
$w_o$	0.684	0.621

Table 5.9: The correlation and regression coefficient for horizontal reference velocities between solutions obtained with a reduce set of unknown parameters.

Random Error $\sigma$	Correlation coefficient	Regression coefficient
0.005	1.00	1.00
0.01	1.00	1.01
0.05	0.65	0.84
0.10	0.11	0.17

Table 5.10: The correlation and regression coefficients between the reference solution and solutions obtained using data with random errors added. The random errors with standard deviation  $\sigma$  are add to the original data as follows: a) salinity,  $\pm\sigma$  ppt and b) temperature,  $\pm\sigma$  °C.

The addition of random errors to the original data simulates the effect of instrument measurement errors on the data. Table 5.10 shows the correlation and regression coefficients between the reference solution and solutions obtained from the data with additional random errors added.

This table shows that the solution is quite insensitive to small random errors in the data. Random errors with standard deviation greater than  $\pm 0.05$  ppt and  $\pm 0.05$  °C need to be added to the original data to significantly change the solution. This value far exceeds the expected errors introduced by limitations in the instruments.

Additional errors in the data arise from the unresolved spatial and temporal features.

Depth-Coherent Errors		Correlation coefficient	Regression coefficient
C	ppt		
0.01	0.002	1.00	0.99
0.05	0.01	0.87	0.94
0.10	0.02	0.63	0.89
0.5	0.10	0.13	0.15

Table 5.11: The correlation and regression coefficients between the reference solution and solutions obtained using data with coherent temperature and salinity errors added to the data.

The temperatures of the ocean obtained from a deep mooring in the centre of the Ocean Storms area clearly illustrates the high frequency variability that is present in the ocean and not resolved by the STP data (Fig. 5.22). The fluctuations in temperature are attributed to isopycnal displacements caused by internal gravity waves. The affects of turbulent mixing are considered to be small. The estimated standard deviation of the all the temperature measurements for the upper 1500 m of the ocean is about  $\pm 0.05^{\circ}\text{C}$ . The fluctuations in the salinity measurements is estimated from the corresponding depth fluctuations shown in this figure and the observed gradient of salinity with depth. The standard deviation of salinity measurement is about  $\pm 0.01$  ppt for the upper 1500 m of the ocean. The salinity errors will have the opposite signs as the temperature errors because of the assumption that this error is due to displacements of isopycnal surfaces.

To simulate these errors in the data, the data at each station is perturbed by a random error where the error in salinity is always  $-1/5$  of the temperature error. Table 5.11 shows the correlation and regression coefficients between the reference solution and solutions obtained from the data with additional coherent errors added.

The large correlation coefficients in this table imply that the pattern of the flow determined the model does not change significantly with the addition of this error. The

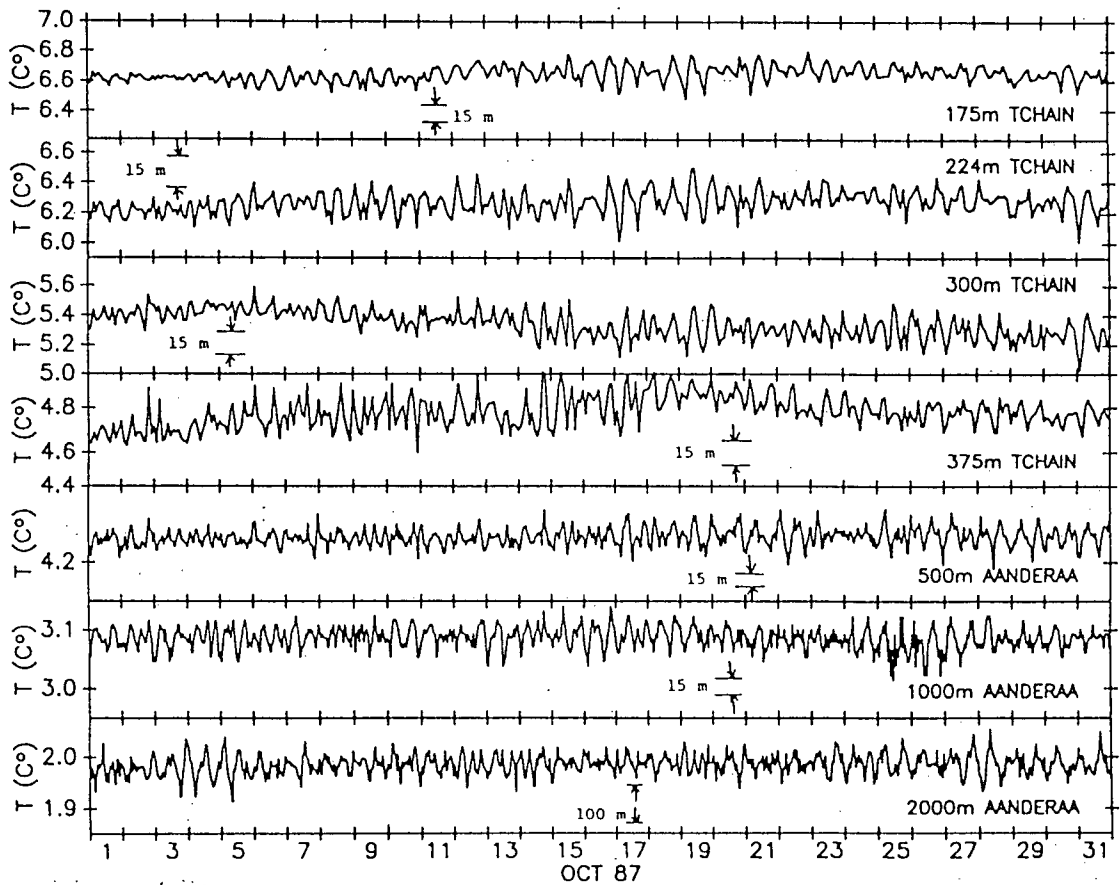


Figure 5.22: The high frequency fluctuations of the temperature measurements obtained from a mooring located in the centre of the grid.

[24]

regression coefficient implies that the magnitude of the solution is not overly sensitive to the expected magnitude of the error present in the data. Using the estimated errors determined from the mooring the estimated one standard deviation errors about the reference solution are:

$$1) u_o = \pm 0.20 \text{ cm/s}$$

$$2) v_o = \pm 0.15 \text{ cm/s}$$

$$3) w_o = \pm 0.30 \text{ } \mu\text{m/s}$$

$$4) k_z = \pm 0.7 \text{ cm}^2/\text{s}$$

These error estimates do show that the errors introduced by features not resolved by the data do place significant limitations on applying this inverse model to synoptic data.

## 5.6 Reference Solution

The results of the model to be presented in the next chapter are based on a 12-layer model using a reference level of 1000 dbar. This model will not use data shallower than 150 dbar (149.1 m) because this data does not satisfy the assumptions made in developing the model. The unknown horizontal and vertical reference velocities and the vertical mixing coefficients will be determined using this model. The horizontal mixing coefficients are omitted because they are poorly determined by the model and unimportant in conserving salt and heat.

The reference solution calculated from this model does achieves a 50% reduction in error over specifying the 1000 dbar level as the level of no motion (reference solution in table 5.3). The estimated one standard deviation errors in this solution are as follows

$$1) u_o = \pm 0.32 \text{ cm/s}$$

$$2) v_o = \pm 0.25 \text{ cm/s}$$

$$3) w_o = \pm 0.5 \text{ } \mu\text{m/s}$$

$$4) k_z = \pm 1.0 \text{ cm}^2/s$$

These errors are determined from the sensitivity of the solution to the choice of reference level and to the presence of error in the temperature and salinity measurements. The results obtained using the reference solution will be presented in chapter 6.

## Chapter 6

### Results of the Model

The results of the inverse model for the data collected during cruise one will be presented in this chapter. This inverse model determined the vertical mixing coefficients for depths  $\geq 149.1$  m, and the vertical and horizontal velocities at the reference level. The determination of the reference velocities does allow one to calculate the flow field at any depth by applying the thermal wind equations and linear  $\beta$ -plane vorticity equation. The only restriction in applying these equations is that the vertical velocities at the surface of the ocean must be zero.

The results of the model for the mixing coefficients and vertical velocities are difficult to verify because of the lack of independent measurements for these quantities. The horizontal flow obtained from the inverse model will be compared to velocity measurements obtained from a current mooring and mixed layer drifters.

#### 6.1 Vertical Velocity

The vertical velocity at the base of the mixed layer (50 m) and in the halocline (150 m) are displayed in Figure 6.23. For depths shallower than 50 m the vertical velocity is assumed to linearly decrease to zero at the surface. In these maps a positive value indicates that the vertical velocity is directed upward. Both these maps are similar, with the vertical velocity in the halocline slightly smaller than the vertical velocity at the base of the mixed layer. Evident in both these maps are the two downwelling zones in the north central and south central part of the Ocean Storms grid. Separating these two

zones is a weak upwelling area. On the west portion of the Ocean Storms grid, a zone of intense upwelling occurs. The vertical velocity at the base of the mixed layer appears to correlate with the convergent and the divergent zones evident in the horizontal flows at the surface (Fig. 6.25). The average vertical velocity at this depth is  $0.96 \pm 0.22 \mu\text{m/s}$ , the error is the two standard deviation error determined from the estimated uncertainty in the vertical reference velocities. Although no direct measurements of this vertical velocity exist, this value is consistent with the vertical velocity of  $0.63 \mu\text{m/s}$  ( $20 \text{ m/yr}$ ) upward determined by Tabata [14]. He estimated this value from the freshwater budget, divergence of the Ekman transport, and convergence of the deep geostrophic transport.

## 6.2 Vertical Mixing Coefficients

The model results for the vertical mixing coefficients are shown in Figure 6.24. This plot of the vertical mixing coefficients shows that  $k_z$  gradually increases with depth to a maximum of  $9.8 \text{ cm}^2/\text{s}$  at 600 dbar. Below this maximum, the values of  $k_z$  gradually decrease to zero. The magnitude of these values is large, but this is attributed to the presence of small scale features in the data. These features in the ocean not resolved by the model were evident in the higher frequency sampling of the ocean (Fig. 5.22). The estimate uncertainty in these coefficients is about  $\pm 1.0 \text{ cm}^2/\text{s}$ . The lack of other measurements for comparison makes it difficult to assess the calculated the vertical mixing coefficients.

## 6.3 Horizontal Velocities

In this section, I will present the model results for the horizontal velocities. In the two sections to follow, the flow field determined from the model will be compared to current meter observations and to velocities inferred from Lagrangian drifters.

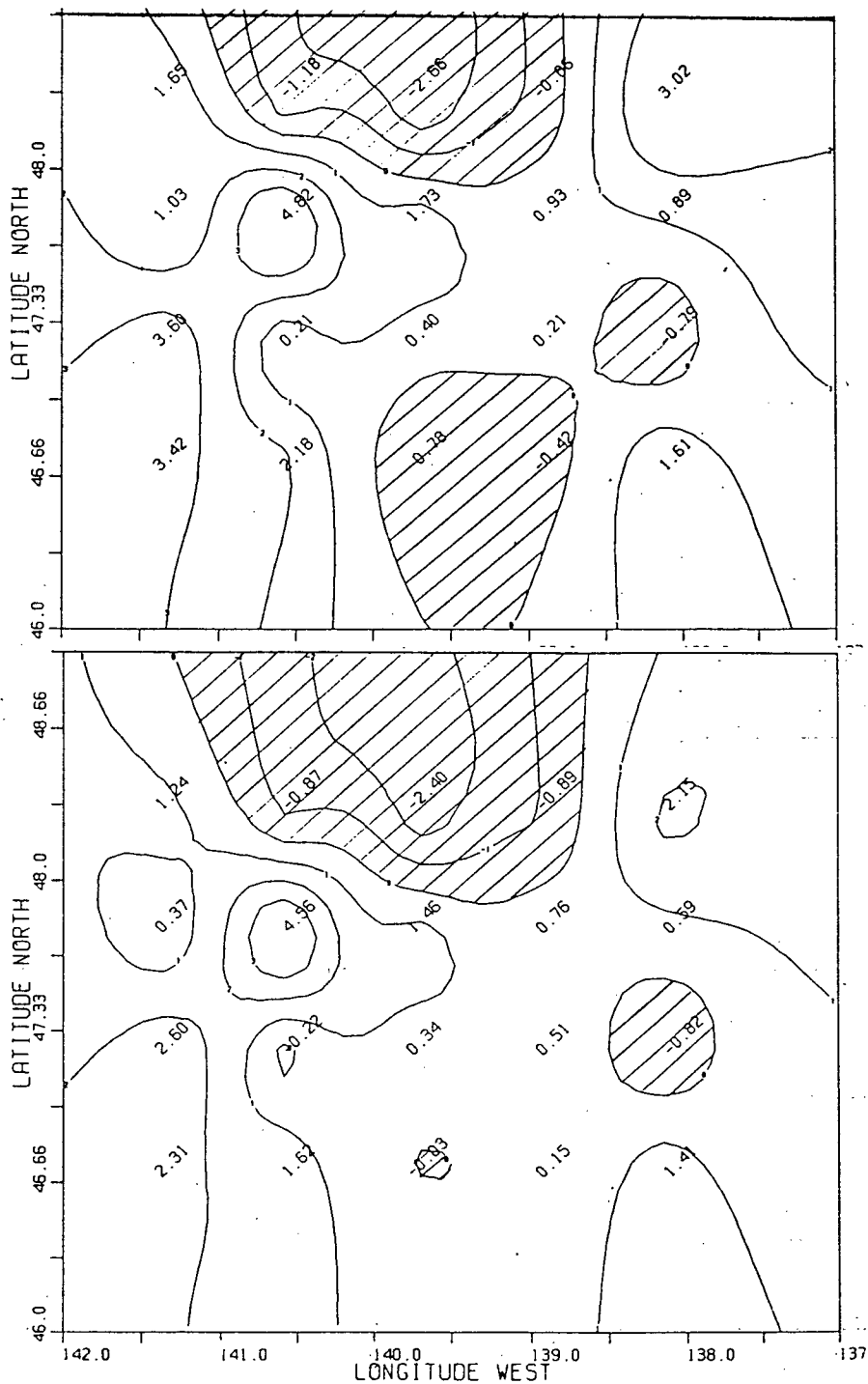


Figure 6.23: The vertical velocity determined from the inverse model. The velocities are in  $\mu\text{m/s}$  and a positive value means the flow is upward. The top map shows the vertical velocity at the base of the mixed layer (50 m). The lower map is the vertical velocity at the base of the halocline (150 m).

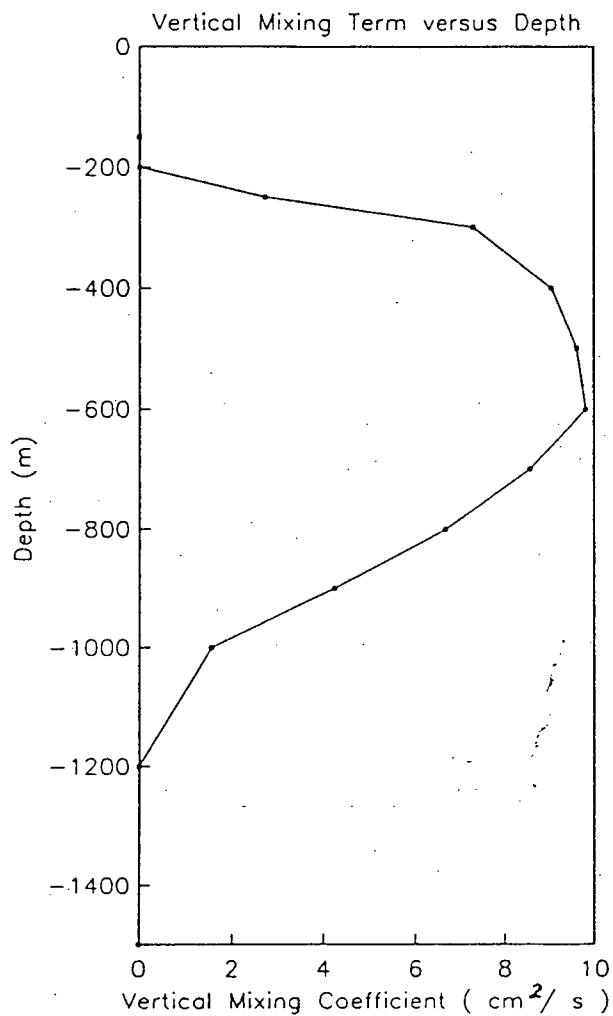


Figure 6.24: The vertical mixing coefficients,  $k_z$ , determined from the inverse model.

The horizontal velocities determined from the inverse model represent the “absolute” geostrophic flow field in the Ocean Storms area. As stated in the previous chapter, the one standard deviation in the horizontal velocities is approximately  $\pm 0.3$  cm/s. This uncertainty present in the reference velocities does not detract greatly from the observed flow pattern. To simplify discussion of the results, I will divide the ocean into three zones, an upper zone (0-200 m), an intermediate zone (200-900 m), and a deep zone (900-1500 m). To display the flow field in these zones I have selected several depth surfaces.

The flow in the upper zone of the ocean, Figure 6.25 exhibited three distinct features. One feature is the presence of an eddy in the northwest corner of the grid. A second feature is the smooth northeasterly flow displayed in the centre of the survey area. The third feature is the distortion in the flow in the southeast corner of the grid. As one moves down from the surface to deeper levels within this zone, the flow in the centre of the grid rotates slightly to the south. The eddy present in the northwest corner of the grid remains almost unchanged within this zone. The feature in the southeast corner of the grid does evolve with depth. What appears as a slight distortion in the flow at the surface develops into a strong countercurrent by a depth of 200 m. At this depth the boundary between the countercurrent and the northeasterly flow is correlated with oceanic front observed in the principal halocline in the maps of the temperature and salinity fields (Fig. 3.13).

In the intermediate zone (Fig.6.26), the three features observed in the upper zone are still evident. The strong eddy found in the northwest corner of the grid is present throughout this zone but by a depth of 900 m this eddy has severely weakened. The smooth flow in the centre of the grid decreases in magnitude with depth. The countercurrent that developed in the lower half of the upper zone is found down to a depth of 900 m. By this point, it is this feature that is most prominent in the flow and encompasses almost half of the survey area.

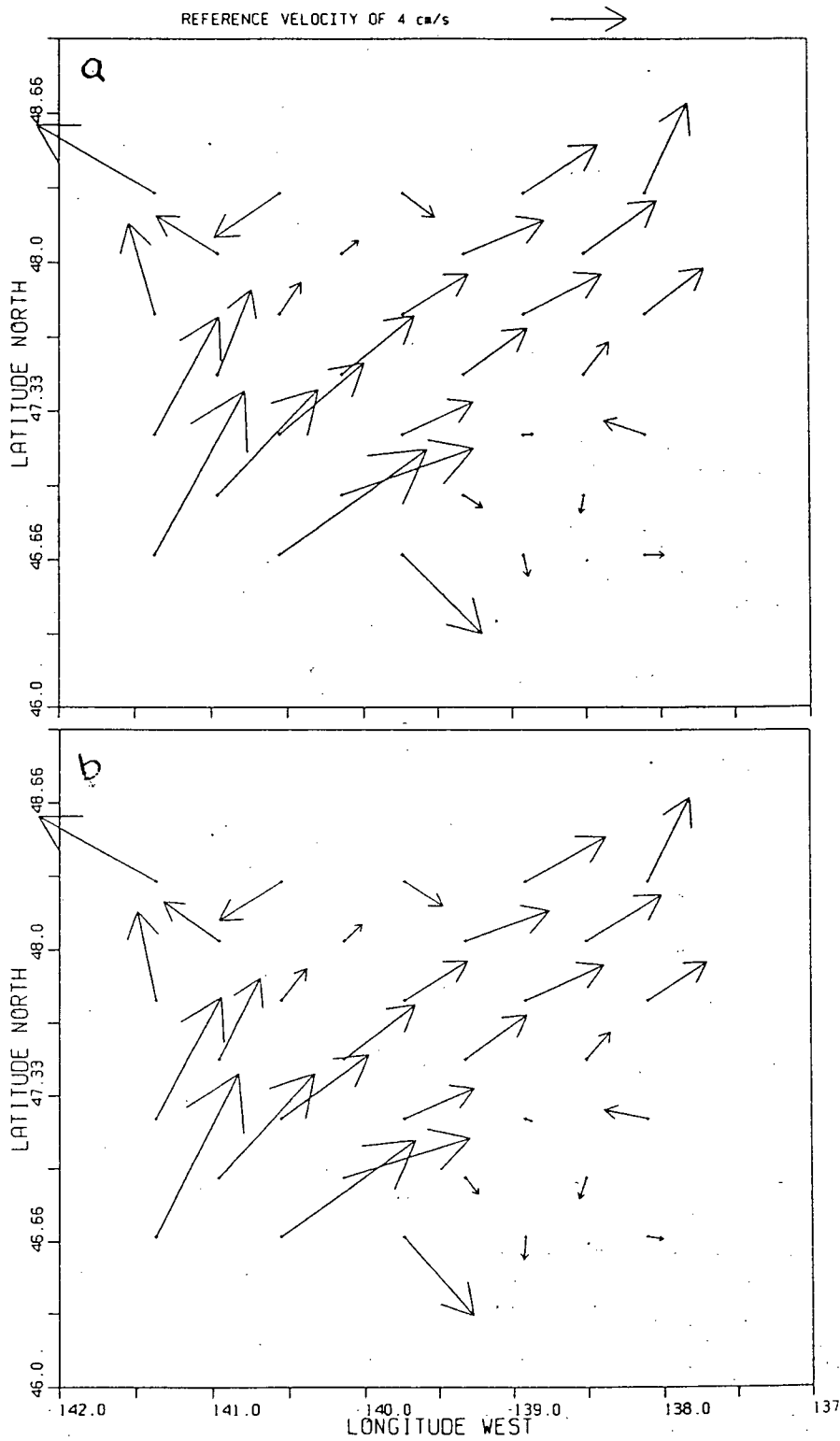
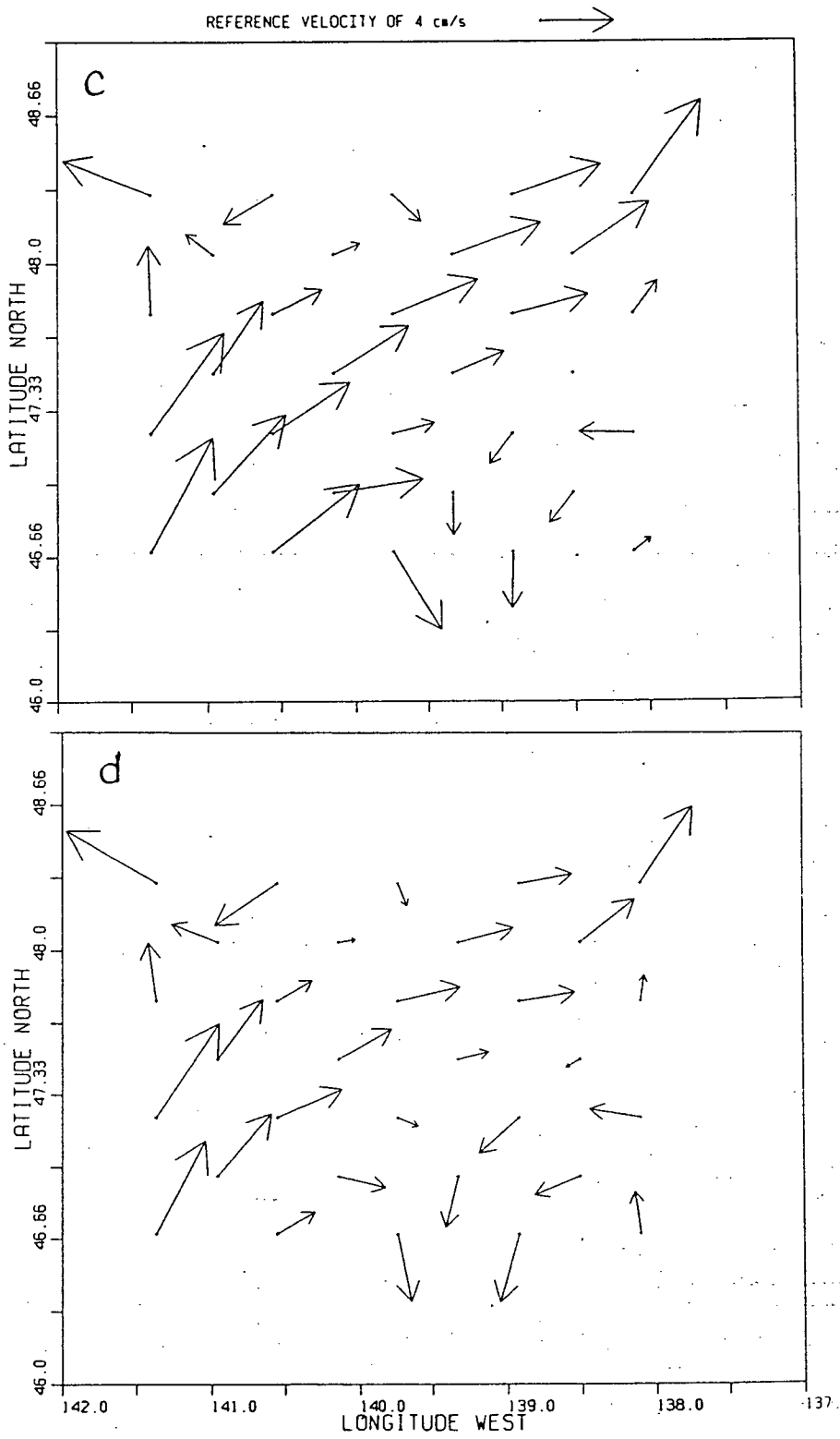


Figure 6.25: The horizontal flow field for selected depth surfaces of the upper zone (0-200 m). The velocity is shown at: a) the surface, b) 15 m, c) 100 m, and d) 200 m.



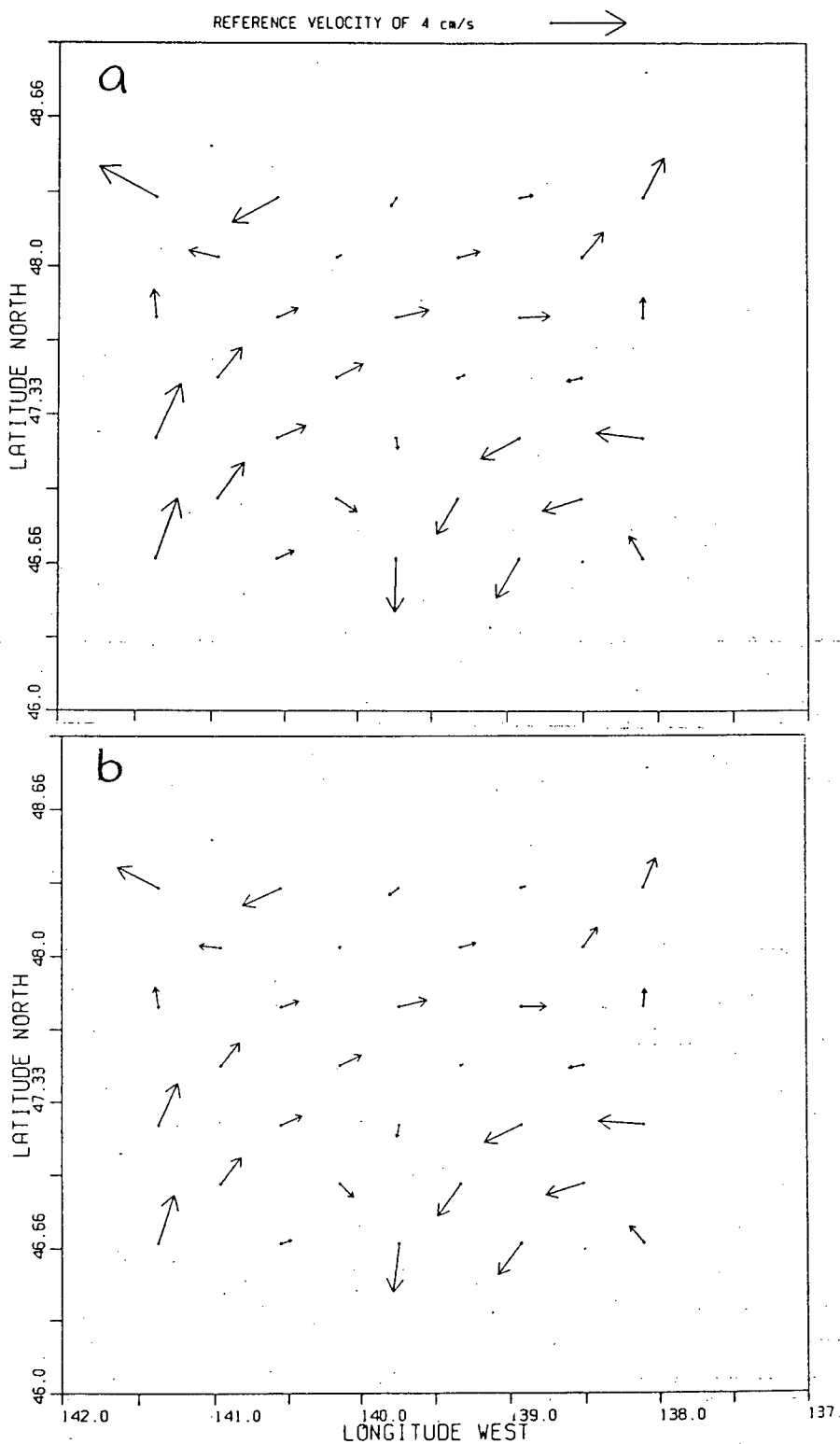
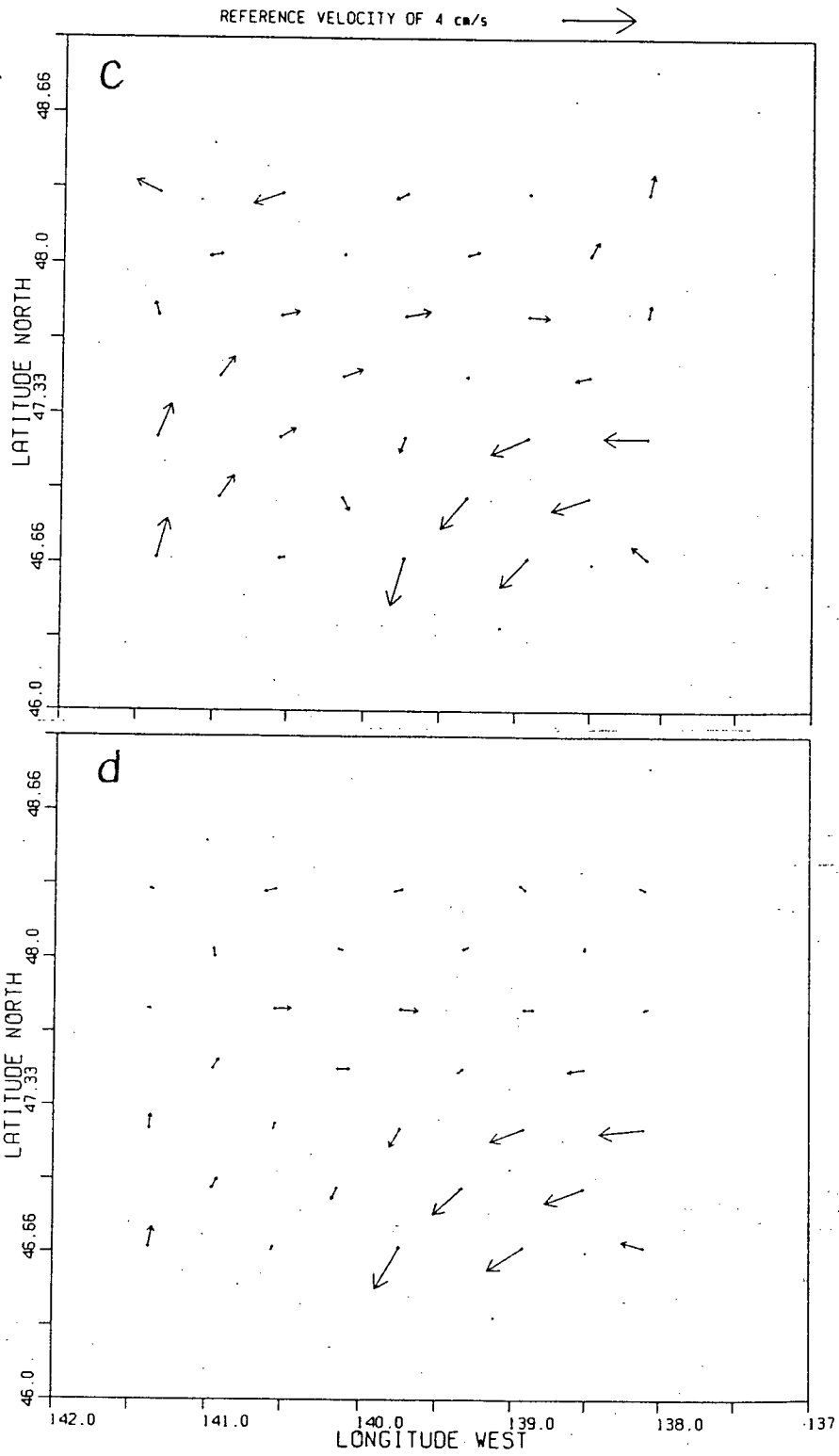


Figure 6.26: The horizontal flow field in the intermediate zone (200- 900 m) at selected depths. The velocity is shown at depths: a) 500 m, b) 600 m, c) 700 m, and d) 900 m.



In the deep zone (Fig.6.27), the flow exhibits much smaller length-scales than what were observed in the previous two zones. The prominent countercurrent is present in this zone but the other two features have disappeared. This leaves the northwest half of the grid without a distinct flow field. At 1000 m the smaller scale features dominate the flow in the northwest. Proceeding to deeper levels, the flow becomes more southerly. The flow pattern at 1500 m appears to reverse from what was observed at the surface.

The flow at 1000 m from the inverse model results shows the difference between the model results and the flow displayed by the maps of dynamic height (Chapter 3). The most significant difference between these two flow fields is the presence of the strong southwesterly flow in the southeastern corner of the grid of the inverse results.

From the flow field determine by the model it is clear from that at no point does the flow field display a clear depth of no motion. As mentioned in the previous chapter, the 700 dbar reference level is appears to be the best choice of a level of no motion. The calculated flow field from the inverse model at 700 m clearly is not consistent with a depth of no motion existing at this level.

#### 6.4 Direct Current Measurements

To validate the velocities determined from the inverse model and to obtain an estimate of the time scale of geostrophic flow, the model results are compared to the velocity measurements made by current meters moored in the centre of the Ocean Storms grid, the OSU mooring (at  $47^{\circ} 28.4'$  N,  $139^{\circ} 16.0'$  W). The current meter observations from this mooring are provided by M. Levine and C. Paulson of Oregon State University. In the upper part of the mooring, seven Vector Measuring Current Meters (VMCM) were distributed from 60 m to 195 m. The lower part of the mooring included five Aanderaa meters distributed from 500 m to 4000 m.

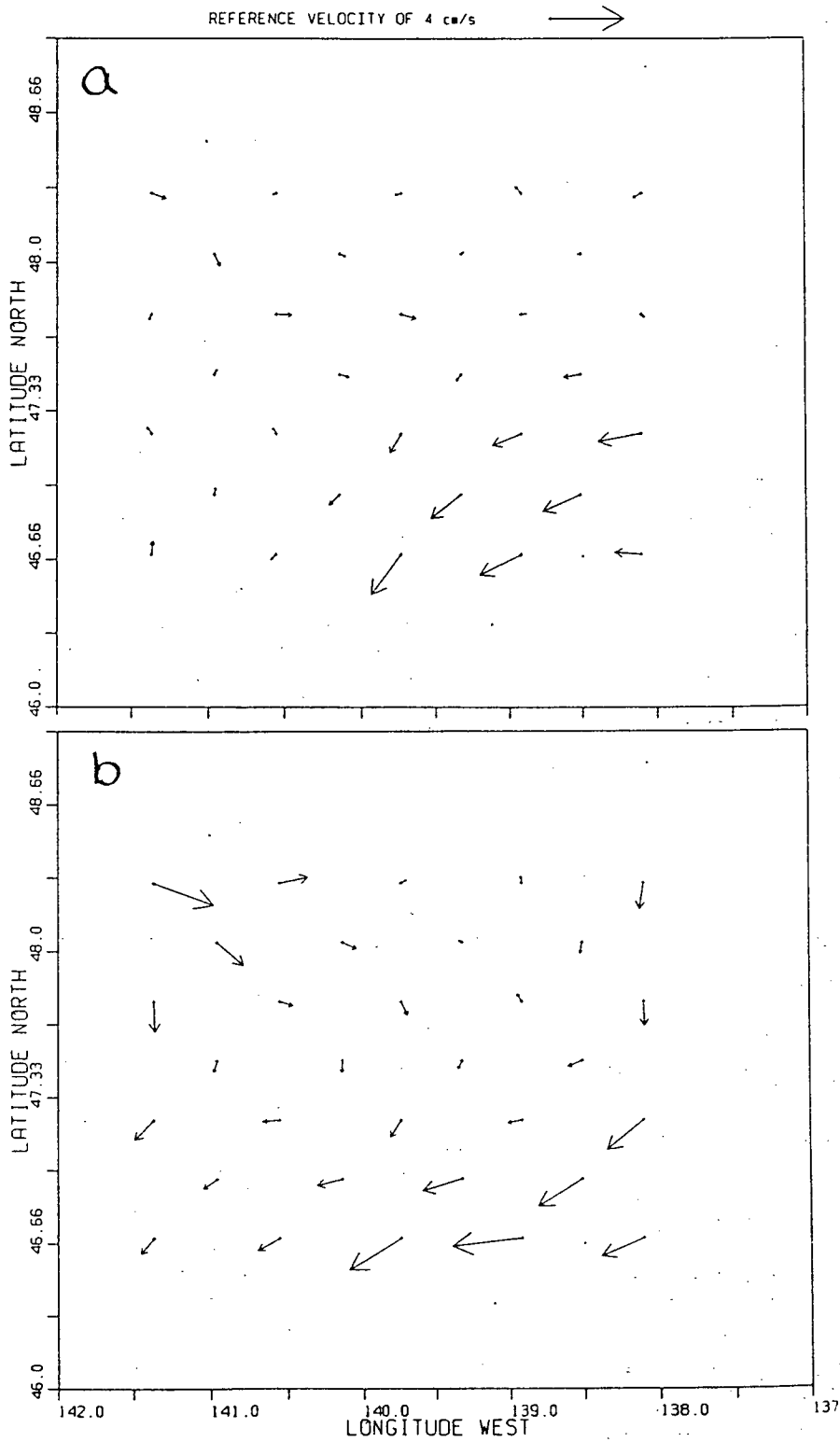


Figure 6.27: The horizontal flow field in the deep zone (900-1500 m) at selected depths. The velocity at depths of a) 1000 m and b) 1500 m.

Depth (m)	Geostrophic Velocity (cm/s)		Averaging Interval (days)	Time Interval (yeardays)		Current Meter Velocity (cm/s)	
	U	V		start	end	U	V
1000	-0.28	-0.36	7	277	284	-0.24	-0.39
500	0.39	0.17	7	263	269	0.40	0.16
195	1.70	0.43	7	255	261	1.75	0.30
160	1.98	0.53	7	255	260	1.99	0.61
140	2.28	0.66	7	257	263	2.16	0.61
120	2.70	1.00	7	246	252	1.70	0.13
100	2.82	1.20	7	233	244	2.82	0.86
60	2.90	1.70	40	251	290	2.27	1.67

Table 6.12: A comparison of the geostrophic velocities calculated from the model to the current meter observations.

The raw data that I received from this mooring had already been low-passed filtered to remove the inertial oscillations and averaged to one-day intervals. From these velocity measurements I further reduced the variability in the data by calculating several time averages. Time averages of the velocity data were obtained for 7 day, 14 day and 21 day time intervals. The results of these times averages are displayed in Figures 6.28, 6.29, and 6.30. In these diagrams the stick points in the direction of the flow, with north being up. The last stick on the right side of the plots are the corresponding geostrophic velocities determined from the inverse model. The time of the first cruise is from 274 to 284 yeardays. The occurrence of the October 4th storm (278 yeardays), is evident in the shallow current measurements by the large increase in velocity that occurred around this time.

The comparison between the current meter observations and the inverse model are summarized in Table 6.12. The calculated geostrophic flow field at the current mooring is comparable to a seven day average of the current meter observations. At 500 m and

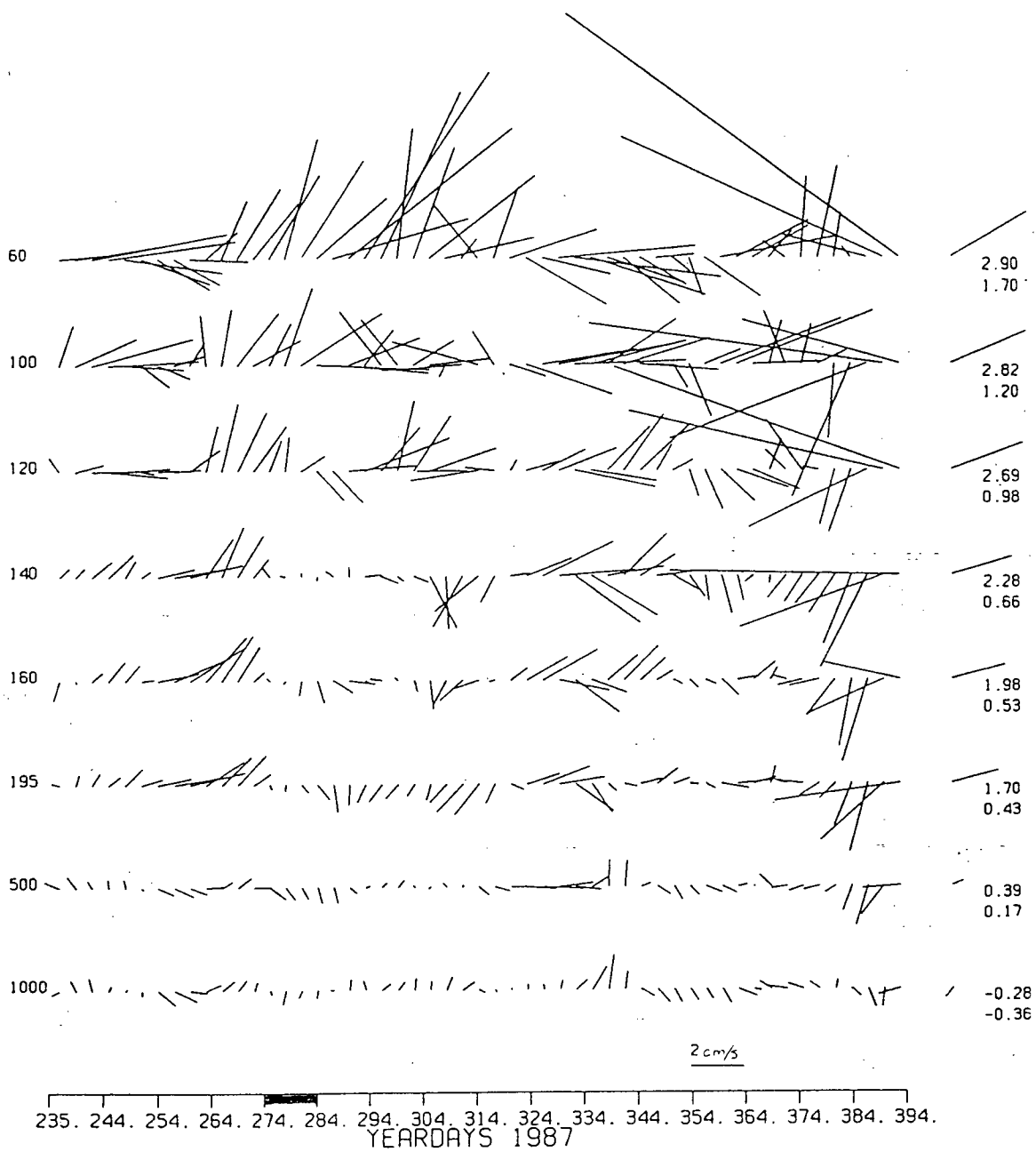


Figure 6.28: The velocities from the current meter observations for a seven day average plotted every three days. In this figure the stick points in the direction of flow, with north being up. The numbers on the left side of the plot are the corresponding depths in meters of the current meter. On the right side of the plot, the velocities calculated from the inverse model at the location of the mooring are displayed.

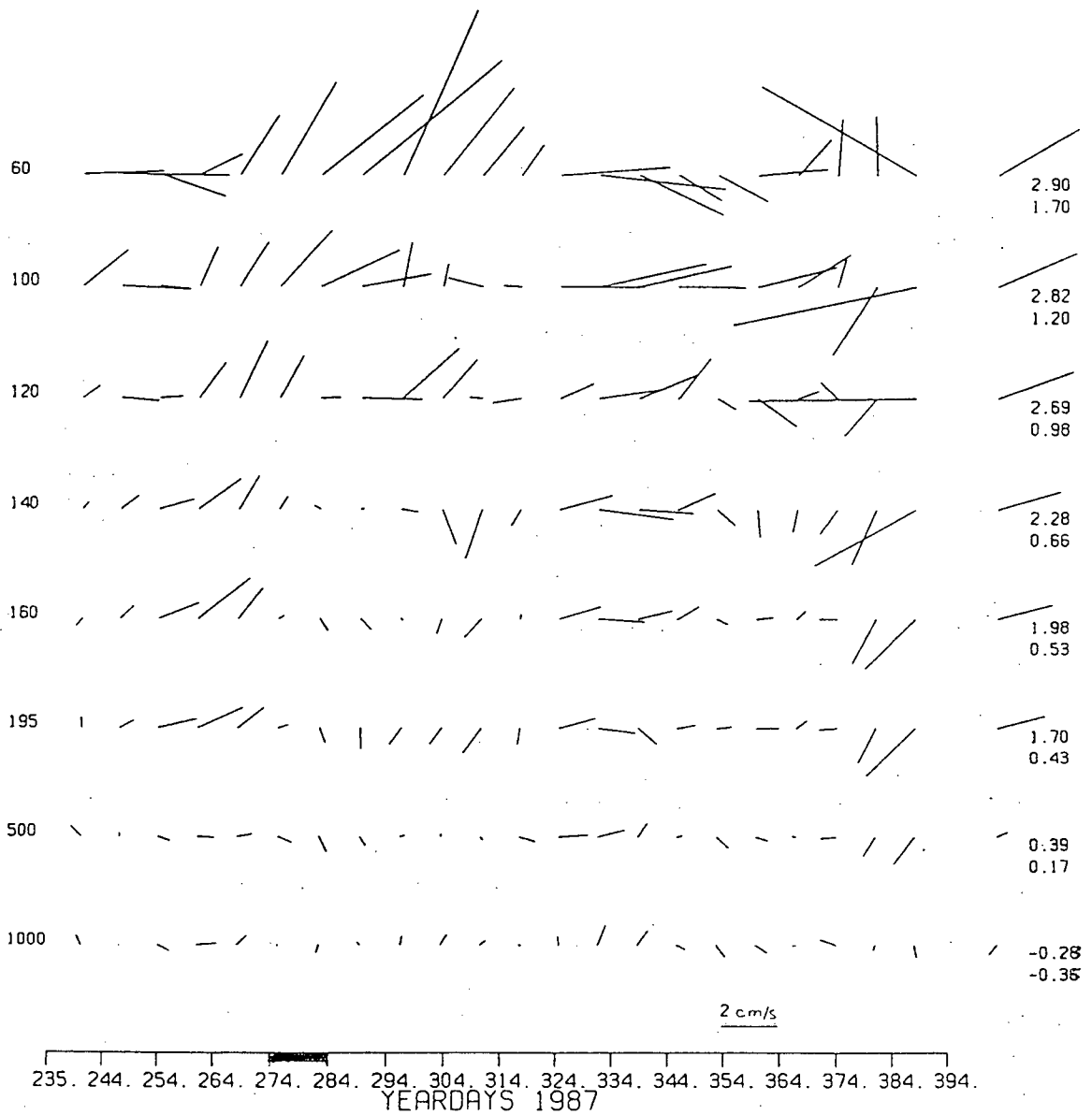


Figure 6.29: The velocities from the current meter observations for a fourteen day average plotted every seven days. In this figure the stick points in the direction of flow, with north being up. The numbers on the left side of the plot are the corresponding depths in meters of the current meter. On the right side of the plot, the velocities calculated from the inverse model at the location of the mooring are displayed.

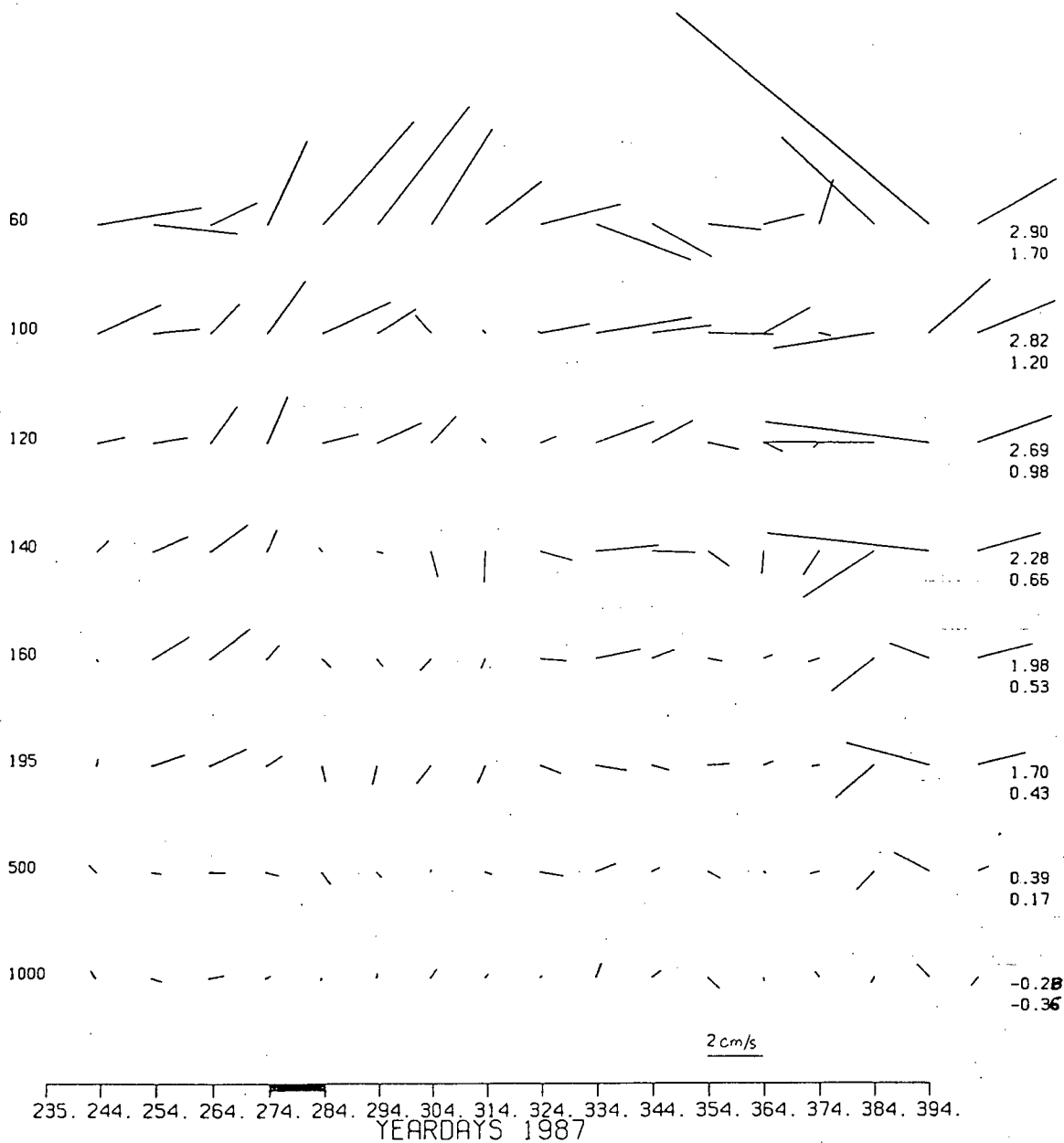


Figure 6.30: The velocities from the current meter observations for a 21 day average plotted every 10 days. In this figure the stick points in the direction of flow, with north being up. The numbers on the left side of the plot are the corresponding depths in meters of the current meter. On the right side of the plot, the velocities calculated from the inverse model at the location of the mooring are displayed.

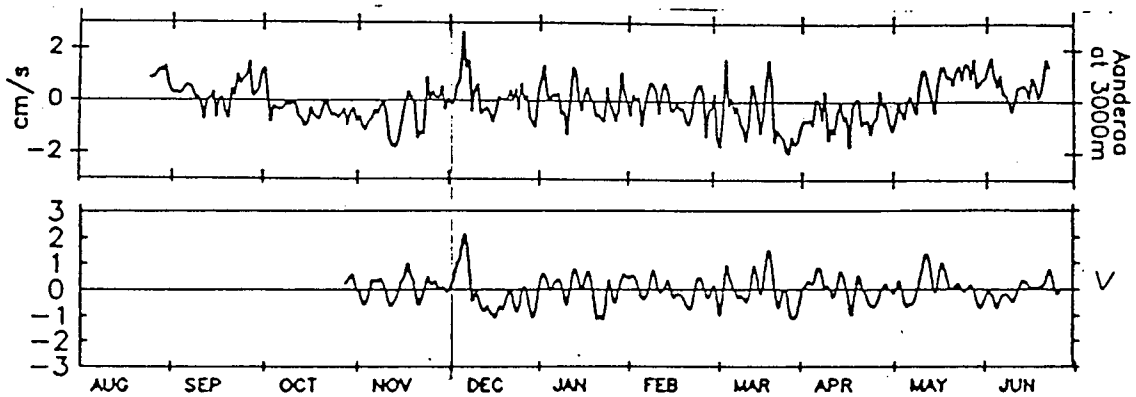


Figure 6.31: The v-component of the velocity measured at 3000 m on the OSU mooring (upper panel) and the v-component computed from the geostrophic relation and data from the bottom pressure sensor array.

[24]

1000 m, the agreement between these two measurements is excellent. At a depth of 1000 m, the geostrophic velocity inferred from the density field is comparable to the average of the current meter observations obtained during the time of this cruise. A bottom array of pressure gauges deployed in the Ocean Storms area also appears to show that the deep geostrophic current measurements inferred from this array are comparable to the current meter observations for periods of a few days to a week (Fig. 6.31) [24].

As one moves upward from 1000 m toward the surface, the geostrophic velocity appears to lag the current meter measurements. This situation may be explained by two possible effects. One, it takes a finite amount of time for the density field to adjust to the present current system. This allows the density field, and hence the geostrophic velocity, to retain information on the previous current field. This suggests that it is the current system that forces the geostrophic flow in the ocean. However, this effect does not explain why the geostrophic flow at the surface lags the current meter observations more than the deeper current meters. The second reason is unrelated to the first but is related to the effects of the October 4th (yearday 278) storm on the current meters. The

energy input into the ocean by this storm at the surface slowly propagated downward. Thus the deeper current meters experienced the effects of the storm at a later time. This implies that at the time of the storm, the flow at the deeper levels was less corrupted by the storm. At 1000 m the average of the current meter observations during the time of the cruise is comparable to the geostrophic flow from the model. As one moves upward toward the surface, the storm effects arrive earlier in time therefore one must move further back in time to observe the geostrophic flow. This effect does not explain why there is a large difference between the current meter observations and geostrophic velocities at a depth of 120 m. At this depth another effect must be considered to explain this large difference.

The lack of an exact agreement between the two velocity measurements can be explained by several reasons. One, direct current measurements do not provide any information on the spatial structure of the flow. But it is clear from the maps of the geostrophic flow that significant spatial features existed in the vicinity of the current mooring. The velocities determined from the inverse model assume some spatial averaging of the velocity field. The most noticeable spatial structure of the flow in the vicinity of the current mooring occurs for depths greater than 500 dbar. Two, the existence of a significant ageostrophic component to the flow may exist. This effect is expected to be greatest near the surface where the forcing function, the wind, is largest and is capable of generating a large ageostrophic component.

Although a seven day average of the current meter measurements provided a good agreement to the geostrophic flow up to 140 m, it does appear that the geostrophic flow may represent time-scales longer than seven days. It is clear from the current meter observations that after the storm the flow again becomes consistent with the calculated geostrophic flow. This most clearly holds true for the depths shallower than 500 m. This observation is also evident in the longer time-averaging of the current meter observations

in the upper 200 m. Although these longer averages produce a good comparison between the two velocity measurements, significant differences still exist. This suggests that the ageostrophic component has a significant low frequency component.

Using a seven day average of the current meter observations obtained during the time of the first cruise, 277 to 284 yeardays, an estimate of the ageostrophic component of the flow is calculated. This estimate of the ageostrophic flow is obtained by subtracting the geostrophic velocities determined by the inverse model from these seven day averages of the current meters. The profile of the geostrophic, ageostrophic, and total flow field are displayed in Figure 6.32. This figure shows that the ageostrophic component of the flow is greatest in the upper ocean (60 - 195 m). The ageostrophic flow is maximum at 60 m but the magnitude of this component is quite uniform between depths of 60 -195 m. The ageostrophic component also undergoes a cyclonic rotation as one moves downward from the surface. This is opposite to the rotation of the Ekman spiral, but this is acceptable because the Ekman spiral only exist in steady winds which is not the case during a storm. The absence of a strong decay in the ageostrophic component with depth suggest that this flow is not forced by the wind. However, the lack of significant total current flow between 140 m and 195 m implies that the geostrophy is not forcing the flow at these depths. Does a depth of no motion exist at this between these depths? If one assumes a depth of no motion at 150 dbar, the errors in the conservation of salt and heat increases drastically. Based on this the 150 dbar level is a poor choice for the level of no motion if one desires that temperature and salinity in the interior of the ocean be conserved.

To explain these features in the ageostrophic flow and total flow, it appears that one must evoke additional terms in the equations of motion

$$\frac{\partial u}{\partial t} + u \frac{\partial u}{\partial x} + v \frac{\partial u}{\partial y} - fv = \frac{-1}{\rho} \frac{\partial p}{\partial x} + \nu \frac{\partial^2 u}{\partial z^2} \quad (6.42)$$

$$\frac{\partial v}{\partial t} + u \frac{\partial v}{\partial x} + v \frac{\partial v}{\partial y} + fu = \frac{-1}{\rho} \frac{\partial p}{\partial y} + \nu \frac{\partial^2 v}{\partial z^2} \quad (6.43)$$

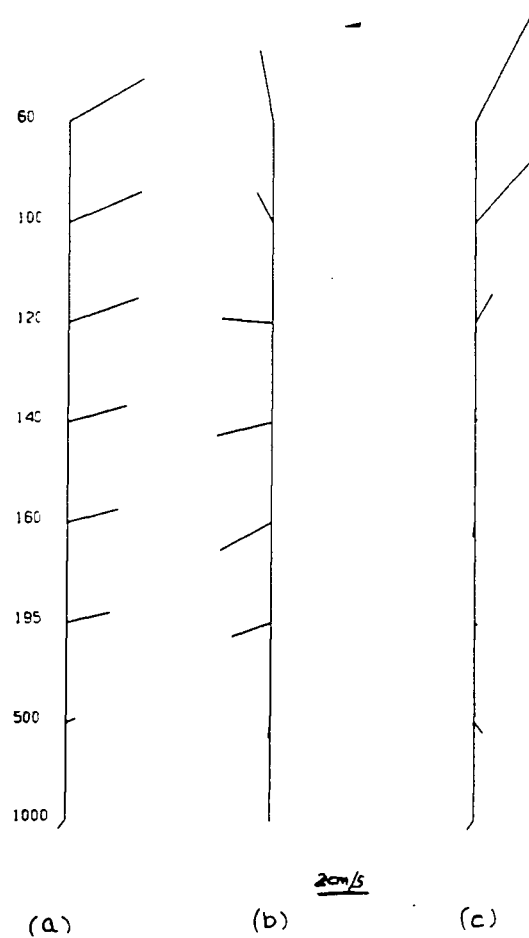


Figure 6.32: The horizontal velocity profiles for a) the geostrophic flow, b) the ageostrophic flow, and c) the total flow.

If this flow is not consistent with being forced by the pressure gradient ( $\bar{\nabla}p$ ) and the windstress ( $\nu\partial^2u/\partial z^2$ ,  $\nu\partial^2v/\partial z^2$ ), the nonlinear terms and acceleration terms must be important.

Any error present in the determination of the velocity of the flow at the reference level will be equivalent to adding an additional constant to all of the ageostrophic measurements. The depth structure of the ageostrophic flow will not be affected by this term.

## 6.5 Mixed Layer Drifters

In the Ocean Storms area, 49 satellite-track TRISTAR drifters were deployed. These instruments consist of a small surface float containing radio transmitting equipment and a large three-axis symmetric drogue element centred at a depth of 15 m. The processed position of all the Ocean Storms drifters are shown in Figure 6.33. The flow evident by this data have similar features to the geostrophic flow determined from the inverse model. The three distinct features evident in the surface geostrophic flow are evident in this data.

In order to better compare these two velocity measurements, a simple algorithm was developed to calculate the velocity from the drifter positions. The area of the Ocean Storms experiment was divided into the same boxes that were used in the inverse model. An average value of the velocity in each of these boxes was determined by calculating the velocity from the change in position of the drifter over one inertial period. This time sampling is necessary to remove the inertial oscillations from the data. Using the time interval of one inertial period, each inertial period provides one independent estimate of the flow for each drifter. By averaging all of these velocities from all of the drifters, the average flow in each of the boxes defined is determined. The resulting flow field estimated from the drifter data over the period of 275 to 295 yeardays is shown in Figure 6.34. Considering a longer time interval does not alter the observed flow in the Ocean Storms area because by this point most of the drifters are no longer present in the grid.

The calculated flow field from the drifter data displays the three characteristic features that were present in the geostrophic flow. These features are a prominent eddy in the northwest corner of the grid, a distortion in the flow in the southeast corner of the grid, and the generally smooth northeasterly flow through the centre of the grid. The fact that these features are evident in this velocity map implies that these major features in

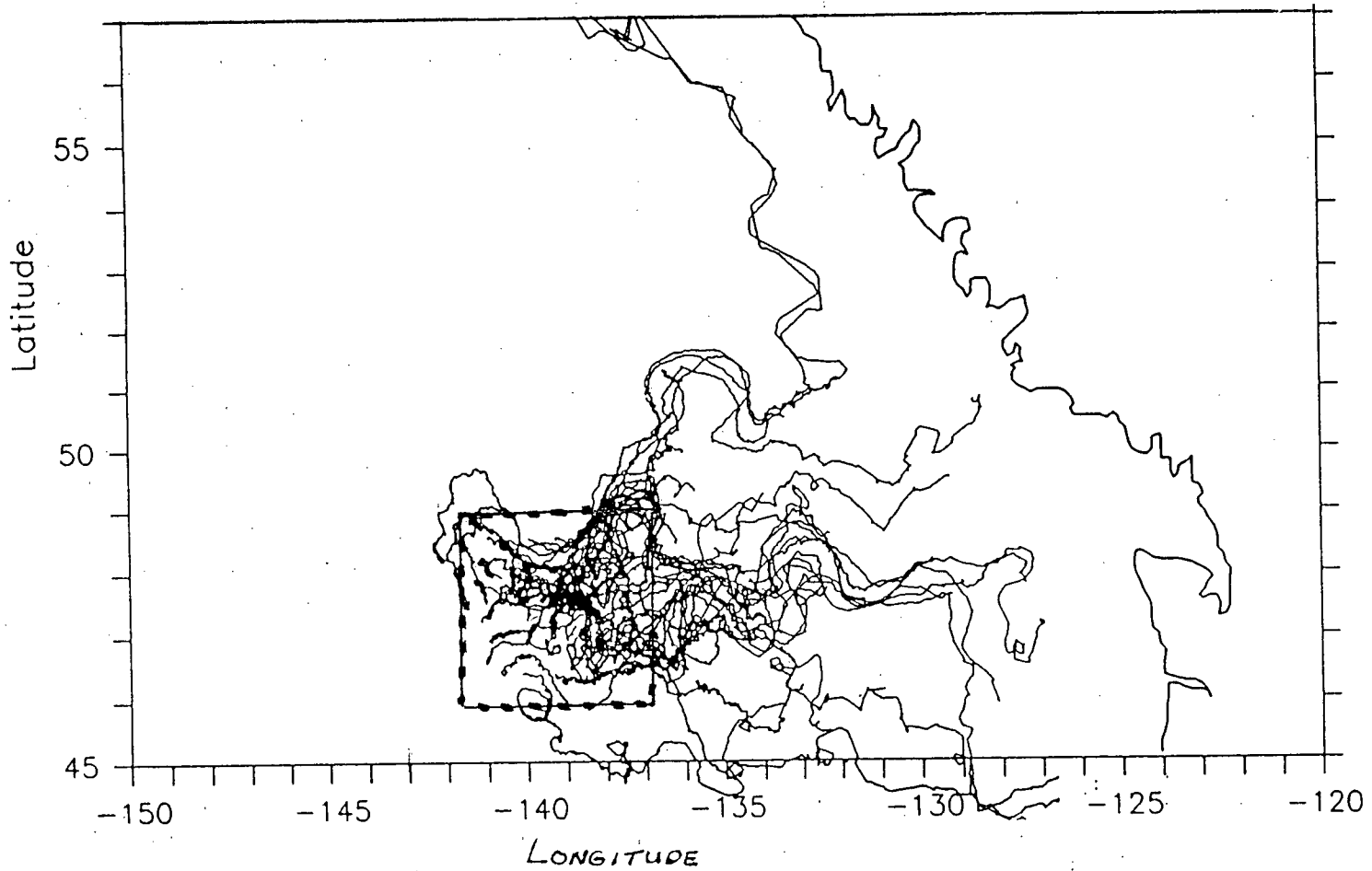


Figure 6.33: The tracks of the drifter data. The location of the Ocean Storms grid is defined by the dashed line on this map. The oscillation of the drifter tracks is due to inertial oscillations.

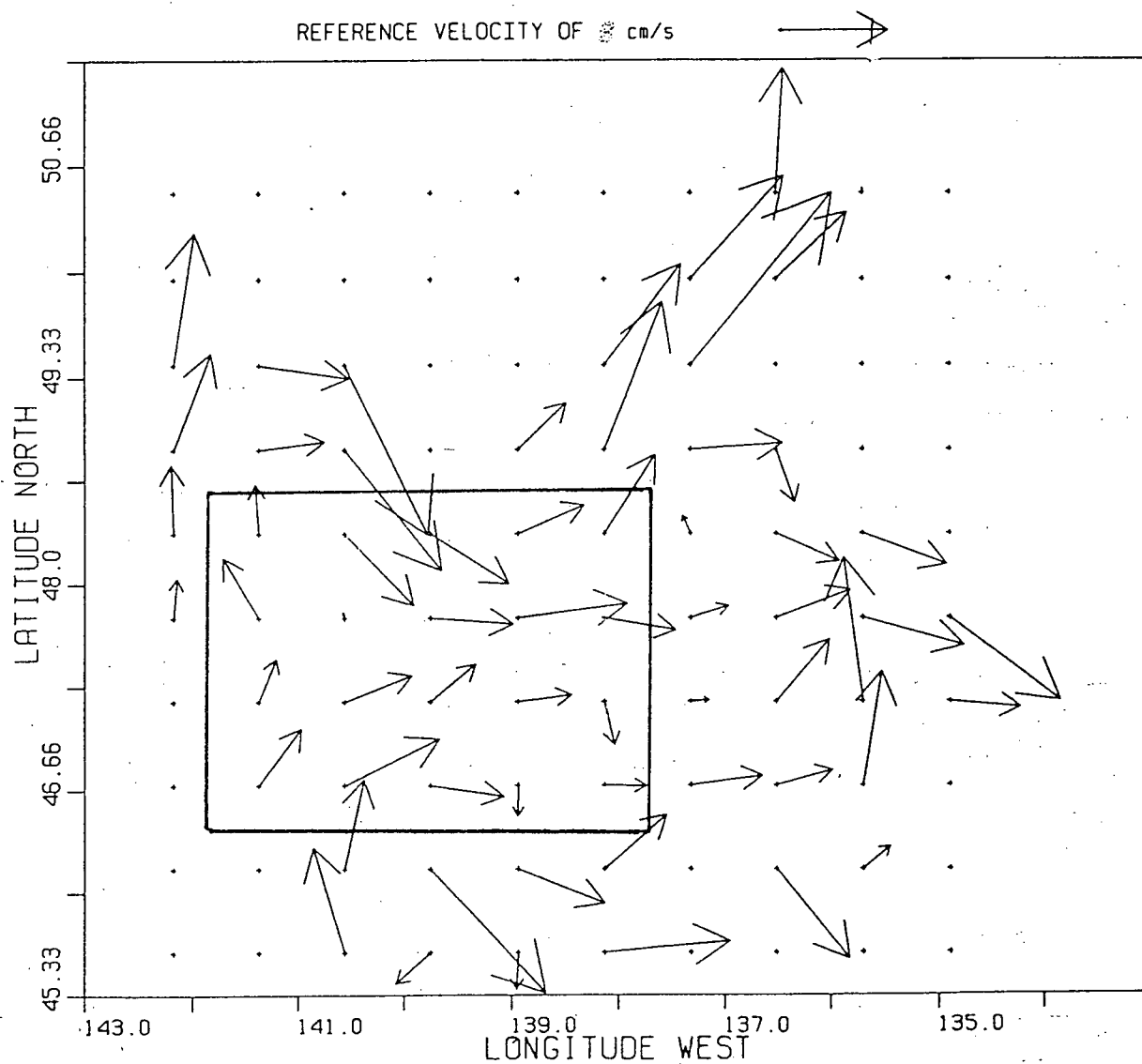


Figure 6.34: The total flow field determined from the drifter data. The location of the Ocean Storms grid is shown by the enclosed region on this map. This velocity map is obtained from the drifter data from day 275 to 295.

the flow field are controlled by geostrophy.

An estimate of the ageostrophic flow can be obtained by subtracting the geostrophic flow from the total flow determined by the drifter data. The inverse model results at a depth of 15 m are subtracted from the total flow field. This difference in flow fields is termed the ageostrophic flow. The ageostrophic flow in the mixed layer is shown in Figure 6.35. The ageostrophic flow shows the presence of a jet in the north with a strong easterly flow which moves in a south easterly direction through the east half of the Ocean Storms area. A smaller flow exists to the south of this jet moving in a southerly direction.

The magnitude of this flow field is significant but possesses smaller spatial features than the geostrophic flow at 15 m. Of the total flow through the Ocean Storms grid, 64% is due to the geostrophic flow and 36% is derived from the ageostrophic component. If the ageostrophic flow was produced by the windstress one would expect that the flow field would exhibit larger spatial features attributed to the larger spatial features present in the wind field. The small spatial features present in the ageostrophic flow field suggest that the windstress is not the dominant forcing term at this time. From this it is inferred that the acceleration and nonlinear terms in the momentum equations (6.42) and (6.43) must play an important role in the affecting the flow. This is consistent with the depth profile of the ageostrophic flow in the centre of the grid.

This analysis of separating the total flow field into ageostrophic and geostrophic flow is essentially independent of the inverse model results because the flow at the reference level does not significantly change the geostrophic flow at the surface.

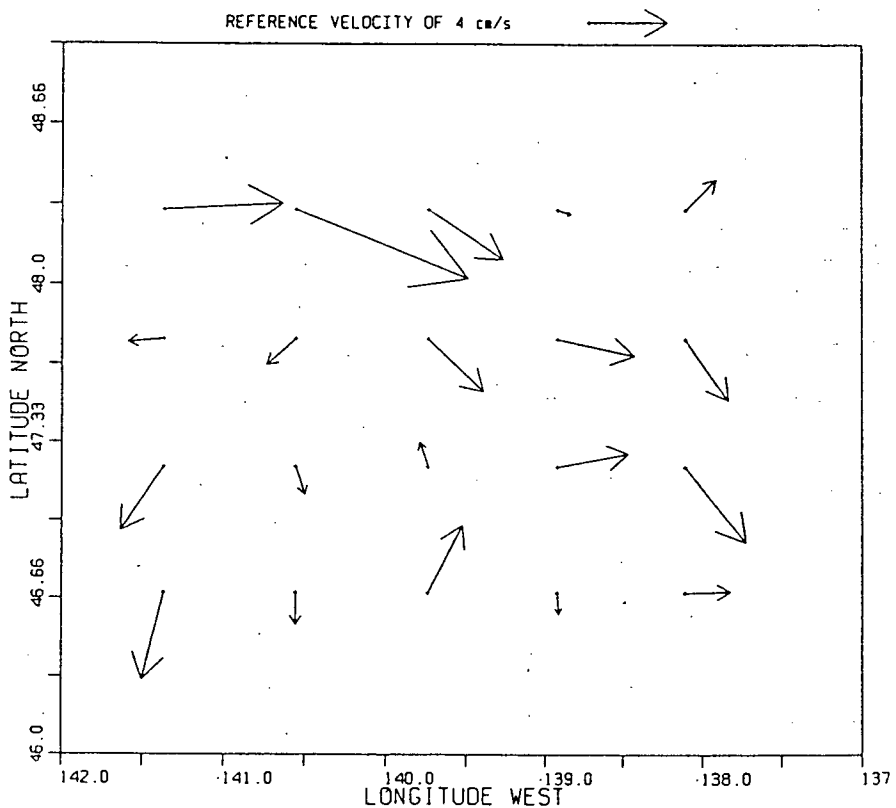


Figure 6.35: The ageostrophic flow field determined from subtracting the geostrophic velocity determined from the inverse model at 15 m from the total flow estimated from the drifter data.

## Chapter 7

### Factors Influencing Heat and Salt Content in the Ocean Storms Area

The factors that influence the salt and heat content in the ocean can be described by the following two equations

$$\frac{\partial S}{\partial t} = -\vec{u} \cdot \vec{\nabla} S + \frac{\partial}{\partial z} \left( k_z \frac{\partial S}{\partial z} \right) + Q^s \quad (7.44)$$

$$\frac{\partial(\rho CT)}{\partial t} = -\vec{u} \cdot \vec{\nabla}(\rho CT) + \frac{\partial}{\partial z} \left( k_z \frac{\partial(\rho CT)}{\partial z} \right) + Q^t \quad (7.45)$$

The change in salt and heat content of the ocean is affected by three factors 1) the horizontal and vertical transport of salt and heat by the flow field,  $\vec{u}$ ; 2) the mixing of salt and heat by the mixing coefficient  $k_z$ ; 3) the exchange of freshwater and heat across the air-sea boundary,  $Q^s$  and  $Q^t$ , respectively.

In this chapter I first determine the change in salt and heat content of the ocean in the Ocean Storms area during the time between the two cruises. Second, I calculate the transport of salt and heat by the flow field and mixing coefficients. Third, by balancing the salt and heat budgets, I estimate the exchange of heat and freshwater across the air-sea boundary.

#### 7.1 The Observed Change in Salt and Heat Content

An estimate of the change in salt and heat content in the Ocean Storms area is determined from the differences in salinity and temperature between the seventeen stations occupied during both cruises. These values of the change in salt and heat content between the two cruises exhibit a great deal of variability over the Ocean Storms grid. To reduce

the variability and increase the accuracy of these values, the mean value for the entire Ocean Storms area will only be considered. The variability of the change in heat and salt content estimated from the different stations is evident from the standard deviations about the mean values. An estimate of the error in the change in salt and heat content is determined from the high frequency temperature fluctuations observed at an OSU mooring. The estimated two standard deviation errors in the salinity and the temperature measurements for the upper 1500 m of the ocean is  $\pm 0.02$  ppt and  $\pm 0.1^\circ\text{C}$  respectively. For each station these error estimates are considered independent of the other stations.

The change in salt content,  $\partial S/\partial t$ , of a layer of the ocean bounded at the top and bottom by the depths  $z_t$  and  $z_b$  respectively is

$$\frac{\partial S}{\partial t} = \frac{1}{\Delta t} \int_{z_t}^{z_b} \Delta S dz \quad (7.46)$$

$\Delta S$  is the change in salinity of this layer during the time interval  $\Delta t$ .

The change in the salt content between these two cruises is shown in Table 7.13. For the upper 1500 m of the ocean the observed change in salt content is equivalent to a  $0.014 \pm 0.005$  ppt increase in salinity during the time between the two cruises (60 days). Such a change is within the accuracy of the measurements of salinity [17]. Considering only the upper 150 m of the ocean, the observed change in salt content is equivalent to an increase in salinity of  $0.004 \pm 0.005$  ppt. Previous estimates of the change in salt content of the upper ocean at Ocean Station P indicate that the upper ocean should experience a significant decrease in salinity during the fall season [17]. This discrepancy between these two measurements of the change in salt content of the upper ocean confirms that the salt content can exhibit significant year to year variability. This variability is influenced greatly by the atmospheric conditions but at the present time the affect the atmosphere has on the ocean is not well determined. This is attributed to the difficulty of trying to

Layer (m)		Change in Salt Content ( $10^{-9}$ ppt/s)		
Top	Bottom	Mean	Error	Standard Deviation
0	100	3.5	0.9	2.1
0	150	0.7	0.9	13.7
0	1000	2.8	0.9	2.8
0	1500	2.7	0.9	2.4

Table 7.13: Change in salt content between cruise one and cruise two. The value given for the change in salt content is the change in salinity observed in that layer. The mean and standard deviation are obtained using the stations occupied during both cruises.

directly measure the rate of evaporation and precipitation in the open ocean.

The change in heat content,  $\partial(\rho C T)/\partial t$ , of a layer of the ocean bounded at the top and bottom by the depths  $z_t$  and  $z_b$  respectively is

$$\frac{\partial(\rho C T)}{\partial t} = \frac{1}{\Delta t} \int_{z_t}^{z_b} \rho C \Delta T dz \approx \frac{\rho C}{\Delta t} \int_{z_t}^{z_b} \Delta T dz \quad (7.47)$$

$\Delta T$  is the change in temperature of this layer during the time interval  $\Delta t$ . The heat capacity ( $\rho C$ ) is assumed independent of depth and equal to  $4 \times 10^6$  kJ/m.

The observed changes in heat content of the ocean during the time between the two cruise are shown in Table 7.14. The observed change in heat content for the upper 1500 m of the ocean is equivalent to a decrease in temperature of this layer of  $0.047 \pm 0.018^\circ\text{C}$  during the time between the two cruises. Such a temperature difference in temperature is definitely within the accuracy of the temperature sensors [14]. In the upper 150 m, the average loss of heat of this layer during the fall 1987 is equal to  $92 \pm 2$  W/m<sup>2</sup>. Large *et al* [16] calculated that the average loss of heat in this area during the fall for the upper 120 m of the ocean was approximately 90 W/m<sup>2</sup>.

Layer (m)		Change in Heat Content ( $W/m^2$ )		
Top	Bottom	Mean	Error	Standard Deviation
0	60	-124	1.0	28
0	100	-96	1.4	32
0	150	-92	2.0	41
0	1000	-65	14.0	128
0	1500	-54	21.0	120

Table 7.14: Change in heat content between cruise one and cruise two. The value given for the change in heat content is the change in heat observed in that layer. The mean and standard deviation are obtained using the stations occupied during both cruises.

## 7.2 Transport of Salt and Heat

An estimate of the transport of salt and heat can be calculated from the ocean circulation parameters, determined by the inverse model and the gradients of the salinity and temperature fields observed during the first cruise. The results of the inverse model allows one to determined the transport of salt and heat by the vertical and horizontal velocities and the vertical mixing coefficients. By using the circulation parameters several assumptions are implied: 1) the horizontal flow determined from this model is geostrophic; 2) the vertical velocity satisfies the linear  $\beta$ -plane vorticity equation, and above the base of the mixed layer (50 m) the vertical velocity linearly decreases to zero; 3) the vertical mixing coefficient is determined only for depths greater than 150 dbar; 4) for depths greater than 150 dbar, one is uses the residual errors of the inverse problem to determine the transport of salt and heat.

The transport of the salt and heat from the flow field and vertical mixing terms are determined for the entire Ocean Storms grid. An estimate of the error in these transports are calculated using the errors in the circulation parameters and the estimated

SALT							
Layer (m)		Horizontal Transport ( $10^{-9}$ ppt/s)		Vertical Transport ( $10^{-9}$ ppt/s)		Total Transport ( $10^{-9}$ ppt/s)	
Top	Bottom	Mean	Error	Mean	Error	Mean	Error
0	60	20	3	2	2	22	4
0	150	27	3	-30	3	-3	4
0	1000	13	3	-17	4	-3	5
0	1500	12	3	-3	4	9	5
150	1500	10	3	-0.4	4	10	5

Table 7.15: The calculated transport of salt using circulation parameters determined by the inverse model. The vertical mixing term is only important at depths of 250 m to 800 m. The errors in these transports are determined from the uncertainty in the circulation parameters and the uncertainty in the measurement of salinity. A positive transport means that the Ocean Storms area experiences a gain in salinity.

uncertainties in the temperature and salinity measurements.

### 7.2.1 Salt Transport

The change in the salt content of the ocean due to vertical transport, horizontal transport and total transport are shown in Table 7.13. In the upper ocean (0 - 150 m), the increase in salinity due to horizontal transport is offset by the larger decrease in salinity caused by the vertical transport. The vertical transport of salt is negative even though the vertical velocity is upward because more salt leaves through the top of the layer than enters through the bottom. The calculated transport of salt in the upper 150 m of the ocean is equivalent to reducing the salinity in this layer by  $0.016 \pm 0.02$  ppt during the time between the two cruises (60 days).

In the deeper layers of the ocean ( $\geq 150$  m) the horizontal transport of salt continues to increase the salinity. The vertical transport of salt works to reduce the salt content in these layers. The vertical mixing of salt by the mixing coefficients is significant only

for depths between 248.4 m and 892.0 m, where it causes the salt content in ocean to increase. In the 150 m to 1500 m layer of the ocean, the calculated transport of salt would result in an increase in salinity of this layer by  $0.05 \pm 0.03$  ppt for the time interval between the two cruises. This exceeds the observed change in salinity of  $0.018 \pm 0.004$  ppt determined from the differences in salinity between the two cruises. This shows that the model does not conserve salt more effectively than the actual interior of the ocean. If the model was more effective in conserving salt this would suggest that the salinity information is being given too much importance in determining the inverse solution. The fact that these two values are comparable implies that the conservation of salt condition in the inverse model was adequately weighted.

### 7.2.2 Heat Transport

The change in the heat content of the ocean due to vertical transport, horizontal transport and total transport of heat are shown in Table 7.16. In the upper ocean (0 - 150 m), the vertical and horizontal transports of heat are nearly equivalent. The vertical transport of heat results in a loss of heat in this layer of  $20 \pm 6$   $W/m^2$ . This value is 21.5% of the observed heat lost by this layer for the time during the two cruises (Table 7.14). This is consistent with previous estimates of the vertical transport of heat which attribute approximately 20% of the heat lost in the upper ocean to this effect [17,16]. The horizontal transport of heat is also significant, it reduces the heat content of the upper ocean by  $20 \pm 10$   $W/m^2$ .

For the layers in the interior of the ocean between the depths of 150 m to 1500 m, the calculated net transport of heat from the model is  $-1 \pm 100$   $W/m^2$ . The observed heat loss of this layer determined from the differences in temperature between the two cruises is  $38 \pm 21$   $W/m^2$ . This shows that the model results does conserve heat more effectively than the real ocean. This suggests that the conservation of heat constraint

HEAT							
Layer (m)		Horizontal Transport ( $W/m^2$ )		Vertical Transport ( $W/m^2$ )		Total Transport ( $W/m^2$ )	
Top	Bottom	Mean	Error	Mean	Error	Mean	Error
0	60	-18	4	-9	1	-32	4
0	150	-20	10	-20	6	-40	12
0	1000	-9	60	-34	7	-43	60
0	1500	-9	100	-32	8	-41	100
150	1500	11	100	-12	8	-1	100

Table 7.16: The calculated fluxes of heat from using the velocities obtained from the inverse model. The vertical mixing term is only important at depths of 500 m to 1200 m. The errors in these transports are determined from the uncertainty in the circulation parameters and the uncertainty in the measurement of temperature.

used in the model could have been downweighted to produce a better agreement with observed heat loss. However, the large error attached to the model value does imply some consistency between this two values thus supporting the weighting of the conservation of heat condition used in the model.

### 7.3 Exchange Across the Air-Sea Boundary

An estimate of the exchanges of heat and fresh water across the air-sea boundary are determined by calculating the sources and sink terms that are required to balance the salt and heat budget in the upper ocean (equations 7.44 and 7.45). In balancing the salt and heat budgets, I will restrict the analysis to the upper 150 m of the ocean where the air-sea boundary process are most pronounced. Below 150 m, there is little evidence of the annual cyclic variations of salinity and temperature that would be attributed to the air-sea boundary process [17]. In this section, I will first balance the salt budget and then I will proceed to balance the heat budget.

### 7.3.1 Salt Budget

The air-sea boundary processes that affect the salt content of the upper ocean are precipitation and evaporation. The reduction of salinity in the open ocean is accomplished by precipitation in the form of rain, snow, and hail. On the other hand the increase in salinity is accomplished by the evaporation of fresh water from the sea surface. The fresh water exchange across the air-sea boundary due to precipitation and evaporation is the most important factor influencing the salinity of the upper surface water [17]. In the northeast Pacific Ocean, this influence is confined primarily to the water above the halocline [17].

In the time interval between the two cruises, the upper 150 m of the ocean experience an increase in salinity of  $0.004 \pm 0.005$  ppt. The estimated vertical and horizontal transport of salt for the upper ocean during the same time interval is  $-0.016 \pm 0.02$  ppt. Therefore, to balance the salt budget would require that fresh water exchange across the air-sea boundary increase the salinity of the upper ocean by  $0.020 \pm 0.020$  ppt. This can only be accomplished by having evaporation (E) exceed precipitation (P) during the fall of 1987.

The change of salinity,  $\Delta S$ , due to E - P, during the time interval  $\Delta t$  can be evaluated from the following formula [17]

$$\Delta S = S_f - S_i \approx S_i \frac{(E - P)}{z} \quad (7.48)$$

$S_f$  is the final salinity (ppt)

$S_i$  is the initial salinity (ppt)

$z$  is the depth (cm) of the column considered (0 - 150 m )

$E - P$  is the difference of evaporation and precipitation in centimetres during the time interval  $\Delta t$

In the Ocean Storms area the initial salinity of the upper zone,  $S_i$  is approximately 33 ppt. Thus, to balance the salt budget would require that  $E - P$  equals  $9 \pm 9$  cm.

### 7.3.2 Heat Budget

The air-sea boundary processes that influence the heat content of the upper ocean are the combined effects of incident solar radiation, reflected solar radiation, effective back radiation, evaporation (and condensation) and conduction of sensible heat. The heat transfer equation across the air-sea boundary during a time interval  $\Delta t$  can be written as

$$Q^t = Q_i - Q_r - Q_b - Q_e - Q_h \quad (7.49)$$

$Q^t$  is the net heat transfer across the air-sea boundary

$Q_i$  is the short-wave radiation from the sun and sky, both direct and diffuse.

$Q_r$  is the reflected short-wave radiation from the sea

$Q_b$  is the effective back radiation (long wave radiation from the sea surface minus that from the atmosphere)

$Q_e$  is the heat transferred by evaporation (and condensation)

$Q_h$  is the conduction of sensible heat between the atmosphere and the sea.

The observed loss of heat in the upper 150 m of the ocean during the fall of 1987 is  $92 \pm 2$   $W/m^2$ . The calculated vertical and horizontal transport of heat in the upper 150 m of the ocean is  $-40 \pm 12$   $W/m^2$ . In order to balance the heat budget in the upper 150 m of the ocean this upper layer would lose  $52 \pm 12$   $W/m^2$  of heat. This implies that the flux of heat at the air-sea boundary accounts for about 57% of the observed heat lost by the upper ocean. From the calculated  $E - P$  value of 9 cm the minimum amount of heat lost by evaporation would be 43  $W/m^2$ . This is comparable to calculated heat lost by the upper ocean. However, in this comparison one must keep in mind that there are other

terms which affect the transfer of heat across the air-sea boundary (equation 7.49).

## Chapter 8

### Discussion and Conclusion

The work presented in this thesis was based on the analysis of hydrographic data collected in the northeast Pacific Ocean as part of the Ocean Storms experiment during the fall of 1987. This work will be summarized in four parts:

- 1) the qualitative description of the hydrography of the ocean during the fall of 1987.
- 2) the development and application of an inverse model to the hydrographic data.
- 3) the ocean circulation of the study area determined from the inverse model.
- 4) the factors that influenced the salt and heat content of the ocean.

In the first part of this thesis, chapter 3, the hydrographic data collected revealed that vertical structure of the ocean represented the Eastern Sub-Arctic Pacific Water Mass and could be divided into three zones: 1) the upper "seasonal zone (0 - 100 m); 2) the principal halocline (100 - 200 m); and 3) the lower zone ( $\geq 200$  m). Maps of dynamic height of the study area showed that the horizontal flow field was quite smooth but did possess prominent mesoscale eddies in the flow. Isentropic analysis of the temperature and salinity fields generally supported the flow field inferred from the maps of dynamic height. However, this analysis revealed additional details in the flow field not evident in the maps of dynamic height. To extract this information from the data an inverse model was developed.

In the second part of thesis, chapters 4 and 5, an inverse model was first developed to calculate the absolute geostrophic velocities, the vertical flow field, and the vertical and horizontal mixing coefficients. These parameters were determined by calculating a model

that best tried to conserve salt, heat, and mass. Unlike finite differencing schemes [6,19], this inverse model calculated the unknown parameters by conserving heat, salinity, and mass in finite volumes. In developing this inverse model, four assumptions were made to simplify the physics of the problem.

- 1) The flow in the ocean is geostrophic.
- 2) The vertical velocities satisfy a linear  $\beta$ -plane vorticity equation.
- 3) A steady state advection-diffusion equation with no sources or sinks can be used in to conserve salt and heat in the interior of the ocean.
- 4) The mixing terms in the advection-diffusion equation are only considered functions of depth and can be parametrized according to vertical and horizontal mixing coefficients. The effects of these assumptions on calculating ocean circulation were considered by comparing the results of the model to other available information.

Second, the inverse model was then applied to the hydrographic data collected. In applying the inverse model to the observed data several problems and limitations arose which affected the results of the inverse model. These limitations are summarized below with a brief explanation of how they affect the inverse problem  $\mathbf{A}\vec{x} = \vec{b}$ .

- 1) The choice of the cutoff level used in determining the singular values that should be included in inverting the matrix  $\mathbf{A}$ . The cutoff level chosen in part determined how sensitive the solution was to errors in the data.
- 2) The weighting of the conservation of temperature, salinity, and mass equations used in solving the inverse problem. In evaluating the model, it was apparent that the solution was very sensitive to the adopted weighting of these three conditions.
- 3) The choice of reference level at which the unknown reference velocities were determined. The uncertainty introduced by the choice reference level is intimately related to the ability of the model to resolve the different unknown parameters.

4) The existence of errors in the temperature and salinity caused by unresolved temporal and spatial features and limitations in measuring equipment. These errors in the data affect both the forcing terms  $\vec{b}$  and the matrix  $\mathbf{A}$ .

An estimate of the uncertainty in the solution was made from the sensitivity of the solution to the choice of reference level and from the sensitivity of the solutions to errors in the data. In this estimate of the uncertainty in the solution, the choice of cutoff level was implicitly used because it affects how sensitive the solution is to errors in the data. The weighting of the equations was not used because this would require better understanding of how well the three conservation conditions were satisfied by the approximate equations used in the model. At present, this kind of information is not well understood in the literature. The errors due to the model assumptions were also neglected; these limitations were assessed in analyzing the results of the model. The estimated one standard deviation errors in the solution are as follows:

- 1)  $u_o = \pm 0.32$  cm/s.
- 2)  $v_o = \pm 0.25$  cm/s.
- 3)  $w_o = \pm 0.5$   $\mu$ m/s.
- 4)  $k_z = \pm 1.0$  cm<sup>2</sup>/s.
- 5)  $k_h$  is neglected.

The horizontal mixing coefficients  $k_h$  were omitted from the final solution because these unknowns were poorly determined by the model and did not play a significant role in conserving salt or heat.

In third part of this thesis, chapter 6, the results of the inverse model for the vertical mixing coefficients and horizontal and vertical flow fields were presented and discussed. These results were compared to other measurements made in the area allowing additional conclusion about the ocean circulation to be made.

The vertical mixing coefficients determined by the model were non-zero between the

depths of 200 m and 1200 m, with a maximum at 600 m. The values of these coefficients were large ( $10 \text{ cm}^2/\text{s}$ ) but this appears to be consistent with other box model estimates of the vertical mixing coefficients [6].

The vertical velocity field determined from the model gave velocities in the upper ocean consistent with previous estimates. The average vertical velocity for the upper ocean in the Ocean Storms area was  $1.0 \mu\text{m}/\text{s}$ . These velocities did exhibit prominent spatial features which appeared to be correlated with divergences and convergences in the horizontal flow at the surface.

The geostrophic flow field determined from the model revealed the presence of mesoscale eddies in the flow. However, the pattern of the flow determined was still generally smooth with well-defined flow features. At the surface the geostrophic flow produced the major features of the flow field evident from the drifter data. The geostrophic velocities calculated from the model were comparable to a seven day average of the current meter observations.

The results of the model for the horizontal flow field also appeared to improve on the assumption that a depth of no motion existed at 1000 dbar. In the halocline (100 - 200 m) the flow field from the model showed the existence of the oceanic front that was clearly present in the temperature and salinity fields but absent from the maps of dynamic height. For depths greater than 1000 m, the horizontal flow field obtained from the model, gave a better defined flow pattern than those obtained with the depth of no motion assumption. Furthermore, the model results were not consistent with the assumption that a level of no motion exists in the flow field.

A depth profile of the ageostrophic flow was determined from the difference between the current meter observations and the geostrophic flow. This profile lacked features that would associate this flow with windstress. The spatial pattern of the ageostrophic flow field in the mixed layer determined from the drifter data and the geostrophic velocities

also implied that this ageostrophic flow was not forced only by the wind. From these results it was inferred that the acceleration and nonlinear terms had an important effect on the flow field during the time of the first cruise. This lack of a connection between the windstress and current meter observations was observed in the JASIN experiment [25]. These investigators concluded that at most times the current in the upper ocean was not wind forced especially when the windstress was small.

In the fourth part of this thesis, chapter 7, the factors influencing the heat and salt content of the upper ocean were calculated. During the 60 days between the two cruises the upper ocean, (0 - 150 m), in the study area experienced a slight increase in salinity of  $0.004 \pm 0.005$  ppt. From the model results the calculated net transport of salt into the upper ocean during this same time period was  $-0.016 \pm 0.2$  ppt. Therefore, to balance the salt budget evaporation had to exceed precipitation by  $9 \pm 9$  cm for the 60 days between the two cruises. During this same period the upper ocean lost  $92 \pm 2$  W/m<sup>2</sup> of heat. The horizontal and vertical net transport of heat each account for a 21.5% reduction in heat content of the upper ocean. The remaining 57% of the heat lost by the upper ocean was due to the net loss of heat at the air-sea boundary.

In conclusion I would like to emphasize that more work still needs to be done on applying inverse models to oceanographic data. A detail study of the problem is required to assess how much information about the flow field can be extracted from tracer data by inverse models. A natural approach to this problem would be to apply the inverse model to data generated from numerical ocean circulation models.

## Bibliography

- [1] C. Wunsch, "The North Atlantic General Circulation west of the 50 W determined by inverse methods," *Reviews of Geophysics*, vol. 16, pp. 583-620, November 1978.
- [2] M. E. Fiadeiro and G. Veronis, "On the determination of absolute velocities in the ocean," *Journal of Marine Research*, vol. 40, pp. 159-182, Supplement 1982.
- [3] R. B. Montgomery, "Circulation in the upper layers of southern North Atlantic deduced with use of isentropic analysis," *Pap. Phys. Oceanogr. Meteorol., Mass. Inst. Tech. and Woods Hole Oceanogr. Inst.*, vol. 6, no. 2, p. , 1938.
- [4] F. Schott and H. Stommel, "Beta Spiral and absolute velocities in different oceans," *Deep-Sea Research*, vol. 25, pp. 961-1010, April 1978.
- [5] G. Dietrich, *General Oceanography*. New York, N.Y.: J. Wiley and Sons, 1963. 588pp.
- [6] D. J. Olbers, M. Wenzel, and J. Willebrand, "The inference of North Atlantic circulation patterns from climatological hydrographic data," *Reviews of Geophysics*, vol. 23, pp. 313-356, November 1985.
- [7] C. Wunsch and J. Minster, "Method for box models and ocean circulation tracers: mathematical programming and nonlinear inverse theory," *Journal of Geophysical Research*, vol. 87, pp. 5647-5662, July 1982.
- [8] C. Wunsch, "An eclectic Atlantic Ocean circulation model. part 1: the meridional flux of heat," *Journal of Physical Oceanography*, vol. 14, pp. 1712-1733, Nov. 1984.
- [9] S. Tabata, "The general circulation of the Pacific Ocean and a brief account of the oceanographic structure of the North Pacific Ocean. part i - circulation and volume transports," *Atmosphere*, vol. 13, no. 4, p. , 1975.
- [10] S. Tabata, L. A. F. Spearing, R. H. Biggam, B. G. Minkley, J. love, D. Yelland, J. Linguanti, and P. M. Kimber, "STP/hydrographic observations along line P, Station P, line R and associated lines in the "Ocean Storms" area: cruise I 22

Sept. - 16 Oct. 1987, cruise III 24 Nov. - 9 Dec. 1987.,” *Canadian Data Report of Hydrography and Ocean Science*, vol. 70, p. , 1988.

- [11] S. Tabata, “An evaluation of the quality of sea surface temperatures and salinities measured at station P and line P in the northeast Pacific Ocean,” *Journal of Physical Oceanography*, vol. 8, pp. 970–986, 1978.
- [12] N. P. Fofonoff and R. C. M. Jr., “Algorithms for computation of fundamental properties of seawater,” *Unesco Technical Papers in Marine Science*, vol. , no. 44, p. , 1983.
- [13] S. Tabata and R. Thomson, “Baroclinic oscillations of the tidal frequency at Ocean Weather Station P,” *Atmosphere-Ocean*, vol. 20, no. 2, pp. 242–257, 1982.
- [14] S. Tabata, “Variability of oceanographic conditions at Ocean Station ‘P’ in the northeast Pacific Ocean,” *Transactions of the Royal Society of Canada*, vol. 3, pp. 367–418, June 1965.
- [15] S. Tabata and N. P. Fofonoff, “Variability of oceanographic conditions between Ocean Station P and Swiftsure Bank off the pacific coast of Canada.,” *Journal of Fish Research Board of Canada*, vol. 23, no. 6, pp. 825–868, 1966.
- [16] W. G. Large, J. C. McWilliams, and P. P. Niiler, “Upper ocean thermal response to strong autumnal forcing of the northeast Pacific,” *Journal of Physical Oceanography*, vol. 16, p. , Sept. 1986.
- [17] S. Tabata, “Temporal changes of salinity, temperature and dissolved oxygen content of the water at Station ‘P’ in the northeast Pacific, and some of their determining factors,” *Journal of Fish Research Board of Canada*, vol. 18, no. 6, pp. 1073–1124, 1961.
- [18] C. Wunsch, D. Hu, and B. Grant, “Mass, heat, salt, and nutrient fluxes in the South Pacific Ocean,” *Journal of Physical Oceanography*, vol. 13, pp. 725–753, 1983.
- [19] E. Tziperman and A. Hecht, “Circulation in the eastern Levantine Basin determined by inverse method,” *Journal of Physical Oceanography*, vol. 18, pp. 506–518, March 1988.
- [20] R. A. Wiggins, “The general linear problem: implication of surface waves and free oscillations for earth structure,” *Reviews of Geophysics and Space Physics*, vol. 10,

pp. 251-285, February 1972.

- [21] C. L. Lawson and R. J. Hanson, *Solving Least Squares Problem*. Englewood Cliff. N.J.: Prentice-Hall, 1974. 1054pp.
- [22] W. Menke, *Geophysical Data Analysis, Discrete Inverse Theory*. Orlando Florida: Academic Press Inc., 1984. 260pp.
- [23] B. Bolin, A. Bjorkstrom, K. Holmen, and B. Moore, "On inverse methods for the chemical and physical oceanographic data: a steady-state analysis of the atlantic ocean.," Tech. Rep. CM 71, Department of Meterology, University of Stockholm, August 1987.
- [24] E. D'Assaro, "Ocean Storms update," Dec. 1988. Applied Physics Laboratory, University of Washington, Seattle Washington.
- [25] R. A. Weller and D. Halpern, "The velocity structure of the upper ocean in the presence of surface forcing and mesoscale oceanic eddies," *Philosophical Transactions of the Royal Society of London*, vol. 308, no. A, pp. 327-340, 1983.